Henning Hünteler

Development and Evaluation of a Multiwire Proportional Chamber for a High Resolution Small Animal PET Scanner

— 2007 —

Kernphysik

Development and Evaluation of a Multiwire Proportional Chamber for a High Resolution Small Animal PET Scanner

Diplomarbeit

von

Henning Hünteler

Westfälische Wilhelms-Universität Münster
Institut für Kernphysik

— Februar 2007 —

Contents

1 Introduction 7

2 Positron Emission Tomography 9

2.1 The β-Decay 10

2.1.1 Different Types of Radioactive Decay 10

2.1.2 Different Types of β-Decays 11

2.1.3 The β-Spectrum 13

2.2 Tracer 16

2.3 Mean Range and Annihilation of Positrons in Matter 18

2.3.1 Positron Range in Matter 18

2.3.2 Positron Annihilation 22

2.4 Interactions of Gamma Radiation in Matter 23

2.4.1 Photoelectric Effect 23

2.4.2 Compton Effect 25

3 Multiwire Proportional Chambers 33

3.1 Basics on Proportional Counters 35

3.1.1 Proportional Counters Tubes 35

3.1.2 Gas Amplification 36

3.1.3 Fill Gases 39

3.2 Multiwire Proportional Chambers 43

3.2.1 Geometry of Multiwire Proportional Chambers 43

3.2.2 Readout Methods 46

4 Motivation for an MWPC Small Animal PET 51
4.1 Reasons for the Construction of a Small Animal PET Detector 51
4.2 Motivation for the Development of an MWPC-based PET Detector . 54
4.2.1 Advantages of Scintillation Crystals 54
4.2.2 Advantages of Multiwire Proportional Chambers 55
4.2.3 Conclusions 56

5 Determination of the Optimal Converter Thickness 57
5.1 Theoretical Determination of the Optimal Converter Thickness 58
5.2 Experimental Determination of the Optimal Converter Thickness . . 62
5.2.1 Experimental Setup 62
5.2.2 Energy Calibration 64
5.2.3 The Measured Spectra 64
5.3 Evaluation of Theory and Measurement 69

6 The MWPC Prototype 71
6.1 Construction of a Multiwire Proportional Chamber 71
6.1.1 G-10 Frame 72
6.1.2 Wire Winding 72
6.1.3 Cathode Pads 73
6.1.4 Fill Gas 75
6.2 Conditioning of the Multiwire Proportional Chamber 76
6.3 Converter Pads 78
6.3.1 Lead Pads 79
6.3.2 Gold Pads 79
6.4 Readout of the Chamber Signals 80

7 Evaluation of the Detector Performance 83
7.1 Calculation of the Achievable Sensitivity 83
7.2 Calculation of the Achievable Spatial Resolution 86
7.2.1 Angular Distribution of the Liberated Electrons 87
7.3 Evaluation of the Performance Parameters 95
7.3.1 Evaluation of the Sensitivity 95
7.3.2 Evaluation of the Spatial Resolution 95

8 Future Prospects 97
8.1 1 mm-Prototype 97
8.2 Readout ASICs 98

9 Summary 101

A Experimental Setups 103

Bibliography 104

Danksagung 111

1. Introduction

In medicine, as well as in industrial productions the positron emission tomography (PET) is used as a procedure of non-invasive imaging. With this technology it is possible to reconstruct a three dimensional image of the spatial distribution of a radioactive tracer molecule within a solvent or biological tissue. Especially in medical research which mainly works with mice as models for the human body functional images of a high spatial resolution are required due to the small size of the organs of a mouse. With new tracer molecules that enrich in regions with special characteristics, e.g. high metabolism, low oxygen supply or even deposits within blood vessels, medical diagnosis could be improved in several fields of research. The search for these new substances demands high quality images which can only be provided by modern PET devices.

Conventional PET cameras usually work with scintillator crystals as gamma ray detectors; the advantages of these crystals are a very good energy resolution, a good timing resolution, a high efficiency and simple handling. But there are some disadvantages, too for example the enormous costs and the very complex architectures necessary to reach good spatial resolutions. Especially for the examination of laboratory animals like mice or rats, a very good spatial resolution is required. Therefore one has to search for other, more economic detector types which might provide a similar or even better performance than scintillator crystals.

One detector technique that has successfully been tested to construct positron emission tomography cameras is the multiwire proportional chamber (MWPC). In these gas filled detectors that were introduced in 1968 by George Charpak [Cha68], ionizing particles can be detected with high spatial resolution. Since this development allowed a totally new and efficient way of particle detection that is still in use in modern particle physics experiments, George Charpak was awarded the Noble Price in Physics in 1992 [Nob07]. Although MWPCs have some disadvantages compared to commonly used scintillation crystals like the missing energy resolution and the very low efficiency, it is believed that the low costs and the very good spatial resolution that can be achieved with multiwire proportional chambers could compensate these disadvantages.

The small animal PET project at the Institut für Kernphysik in Münster is supported by the Collaborative Research Center SFB 656 Mobil of the University of Münster since July 2006. This Collaborative Research Center has been installed in July 2005 to develop new technologies and methods for cardiovascular molecular imaging. To research on this interdisciplinary science, scientists and clinicians from the faculties of chemistry, mathematics, computer science, physics and medicine work together on several projects [Mob07].
Subject of this diploma thesis is the development and performance evaluation of a multiwire proportional chamber, assigned to be used in a positron emission tomography device for small animals.
After the discussion on the theoretical background in Chapters 2 and 3, the motivation to construct a small animal PET using MWPCs is discussed in Chapter 4. Chapter 5 describes the theoretical and experimental determination of the optimal layer thickness for the converters that are needed to detect incident γ-radiation with an MWPC. The development of the first MWPC prototype is presented in Chapter 6, while its theoretical and experimental evaluation is discussed in Chapter 7. Chapter 8 finally gives a prospect on the future tasks.

2. Positron Emission Tomography

Positron Emission Tomography (PET) is a non-invasive diagnostic method to produce functional in vivo images of the examined tissue. It is used in medical research as well as in clinical everyday life for diagnosing the metabolism of brain, heart and tumor cells.

Based on the detection of the radiation of annihilating positrons one can assign the original distribution of the administered tracer. By linking a positron emitting isotope e.g. to a glucose molecule that concentrates in regions of increased metabolism, the tracer can be deposited in these areas.

When the isotope decays, the emitted positron has a short mean free path (see Section 2.3.1). It is decelerated until it annihilates with an electron from the surrounding tissue. The two photons, which are produced in most annihilation events, leave the place of annihilation back-to-back with an energy of 511 keV each. If these two photons are detected in two different detectors, a so-called "Line of Response" (LOR) can be calculated on which the decay took place. However, the actual position on the LOR is unknown. By detecting a huge number of photons, the original distribution of the tracer can be determined to reconstruct a three dimensional image that displays the original tracer distribution within the patient's body. Therefore the LORs are superposed so that the points where multiple LORs coincide have an increased likelihood for the tracer distribution.

Although a substantial exposure dose for the patient is involved with this type of imaging, the positron emission tomography is one of the most important techniques in the clinical nuclear medicine as well as in medical research. In spite of the recent progress in several imaging technologies like fMRT[1] or ultrasonic imaging, PET and the related technology of SPECT[2] are the only technologies that allow metabolistic imaging.

[1] fMRT: functional Magnetic Resonance Tomography. An imaging technology, where two magnetic resonance images of the same tissue are taken with a certain time lag. The two images are compared and the variations are illustrated to display changes e.g. in perfusion.

[2] SPECT: Single Photon Emission Computed Tomography. The technology of taking functional images by reconstructing the concentration of a γ-emitting isotope. The principle of radiation detection and image reconstruction is similar to PET. However, as there is only one $\gamma-$particle to be detected, the image quality is lower than the quality of PET images.

2.1 The β-Decay

2.1.1 Different Types of Radioactive Decay

Since the beginning of the twentieth century, physicists have been distinguishing between three different types of radioactive radiation:

- α-radiation - This form of radioactive radiation, which is described in Equation 2.1, consists of helium nuclei which consist of two protons and two neutrons. Due to the high scattering cross section, the stopping power for α-particles is very high for all elements. According to [Car06], the continuous-slowing-down approximation range R_{CSDA} in solids is on the order of a few μm for energies of typical α-radiation. Even the CSDA range for α-particles in air is only 3.6 cm [Ber05a], so that α-radiation usually does not cause harm to the human body when not being incorporated. However, since the whole α-energy is deposited in a very little amount of tissue when an α-emitting isotope is incorporated into the human body, it has a very high damage potential and therefore is very dangerous. Since this type of nuclear decay is a two-body decay, the kinetic energy Q of α-particles has a discrete value, usually $4-6$ MeV.

$$ {}^{A}_{Z}X \rightarrow {}^{A-4}_{Z-2}Y + {}^{4}_{2}He + Q \tag{2.1} $$

- β-radiation - Electron respectively positron radiation that originates from nuclear disintegrations is called β-radiation. In the β-decay, which is caused by the weak force, β-particles are emitted with a very wide energy distribution. This is due to the emission of a second particle in addition to the charged electron or positron respectively (see Equation 2.2 and Equation 2.3). This particle, which is called antineutrino or neutrino respectively, was postulated by Pauli in 1930 and satisfactorily detected in 1956 by Cowan and Reines [Gru00]. The neutrino and the antineutrino respectively, receives the energy difference between the reaction energy Q and the actual β-energy. β-radiation with a typical energy of e.g. 1.5 MeV can be shielded with a layer of 5 mm of polyethylene [Ber05a]. The problem of shielding β-radiation with high-Z materials is the occurrence of electro-magnetic bremsstrahlung, which is emitted during the stopping process of charged particles in these materials

[Bet01]. Therefore β-radiation usually is shielded with low-Z materials for example like synthetics. The principle of positron emission tomography is based on the decay of β-emitting isotopes within the examined tissue.

$$^{\mathrm{A}}_{\mathrm{Z}}\mathrm{X} \rightarrow {}^{\mathrm{A}}_{\mathrm{Z+1}}\mathrm{Y} + \mathrm{e}^{-} + \overline{\nu_{\mathrm{e}}} + \mathrm{Q} \tag{2.2}$$

$$^{\mathrm{A}}_{\mathrm{Z}}\mathrm{X} \rightarrow {}^{\mathrm{A}}_{\mathrm{Z-1}}\mathrm{Y} + \mathrm{e}^{+} + \nu_{\mathrm{e}} + \mathrm{Q} \tag{2.3}$$

- γ-radiation - γ-radiation is a type of electromagnetic radiation with energies of several keV up to a few MeV. Due to its electromagnetic character, this type of radiation is very hard to shield and therefore can be very dangerous to handle. For instance the total attenuation coefficient for γ-rays of an exemplary energy of 500 keV in a lead absorber is $\mu = 0.161$ cm^2/g [Ber05b]. For this attenuation coefficient, the length of a lead absorber that is needed to attenuate the radiation to 1% of its original number of γ-particles is $x_{Pb} = 25.312$ mm. γ-radiation is emitted by excited nuclei, decaying to a lower state or by annihilation of matter-antimatter pairs. Equation 2.4 describes the emission of γ-radiation of a deexiting nucleus.

$$^{A}_{Z}X^{*} \rightarrow {}^{A}_{Z}X + \gamma + Q \tag{2.4}$$

2.1.2 Different Types of β-Decays

Due to its considerable importance for the understanding of positron emission tomography, the β-decay shall be discussed in more detail in the following:
After its discovery in the year 1900 by H. Becquerel, this kind of radioactive decay was subject of many controversial discussions. The original reaction formula, proposed by Becquerel, did not include a neutrino:

$$n \rightarrow p^{+} + e^{-} + Q \tag{2.5}$$

Because several fundamental conservation laws are broken by this formula there are sundry problems with the interpretation of the observations:

- The observed energy spectra of the emitted electrons (or positrons respectively) are continuous. Since the parent nucleus, as well as the daughter nucleus, has a definite energy, the energy conservation law seems to be broken.

- Due to a two-particle decay, the β-particle and the daughter nucleus ought to leave the point of decay with an angle of exactly 180 degrees; this can almost never be observed. As the angle between the trajectories of the two particles slightly differs from 180 degrees, the momentum conservation law seems to be broken as well.

- Electrons have a spin of $1/2$ in units of $\hbar$. When a spin- $1/2$ -particle is emitted, the parent nucleus should merge from an integer spin state into a half-integer spin state and vice versa. But as the spin number of a nucleus is determined by the number of nucleons and the atomic number of the parent nucleus does not change during the β-decay, the angular momentum conservation law seems to be broken, too.

With the definite proof of the existence of neutrinos by Cowan and Reines in 1956, these problems with the explanation of the observed effects have been solved. The neutrino carries the difference between the reaction energy and the actual electron energy in form of kinetic energy. Concerning the angular distribution of the emitted neutrino, the momentum conservations law is satisfied and the neutrino spin of $1/2$ maintains the angular momentum conservation law.
Nowadays there are three known forms of the β-decay that shall be explained briefly:

- β^--decay
  The β^--decay is the classical β-decay, described by H. Becquerel. In this type of decay, a neutron decays into a proton and emits an electron and an anti-electron-neutrino (Equation 2.6).

$$n \rightarrow p^+ + e^- + \overline{\nu_e} + Q \tag{2.6}$$

- β^+-decay
  Here, a proton decays into a neutron with the simultaneous emission of an electron neutrino and a positron (Equation 2.7). β^+-radiating isotopes are used for PET imaging. Since the mass of the neutron is higher than the proton mass, the β^+-decay can only occur when the energy of the parent nucleus is higher than the energy of the daughter nucleus. If this is not the case, the conversion can only take place via a so-called electron capture reaction.

$$p^+ \rightarrow n + e^+ + \nu_e + Q \tag{2.7}$$

- Electron Capture
  The electron capture reaction is a kind of reverse β^--decay. Here, an electron of one of the inner electron shells is captured by a proton from the nucleus which emits an electron neutrino and transforms to a neutron. The reaction formula reads as follows:

$$p^+ + e^- \rightarrow n + \nu_e + Q \tag{2.8}$$

  As there is only one particle emitted during this nuclear reaction, the excess energy is not shared between the liberated particles, so that the neutrino has a fixed energy. The generated electron hole in the K-shell or rarely the L-shell is replenished by an electron from an outer shell. Hence, an x-ray photon or an Auger electron is emitted.

2.1.3 The β-Spectrum

Due to the emission of a neutrino, the spectrum of the β-particles that are emitted during the β-decay has a continuous shape since the reaction energy is shared between the two emitted particles. The shape of the spectrum can be calculated with Equation 2.9 [Kri04]:

$$N(\varepsilon)d\varepsilon \propto \varepsilon \cdot \sqrt{\varepsilon^2 - 1} \cdot (\varepsilon_0 - \varepsilon)^2 d\varepsilon. \tag{2.9}$$

Here ε_0 is the reaction energy and ε the energy that is carried by the electron or the positron respectively. The energies ε_0 and ε are given in units of the rest energy

of the β-particles ($\varepsilon_0 = \frac{E}{m_e c^2}$ and $\varepsilon = \frac{E_e}{m_e c^2}$). Equation 2.9 describes the energy distribution of the β-particle at the point of emission. It takes not into account the Coulomb field of the daughter nucleus: electrons are decelerated while positrons are accelerated in the repulsive Coulomb potential. To take the so-called Coulomb shift into account, Equation 2.9 is corrected with the factor F_c.

$$N(\varepsilon)d\varepsilon \propto \varepsilon \cdot \sqrt{(\varepsilon^2 - 1)}(\varepsilon_0 - \varepsilon)^2 \cdot F_C \cdot d\varepsilon \tag{2.10}$$

A typical β-spectrum is shown in Figure 2.1, where the Coulomb shift is illustrated.

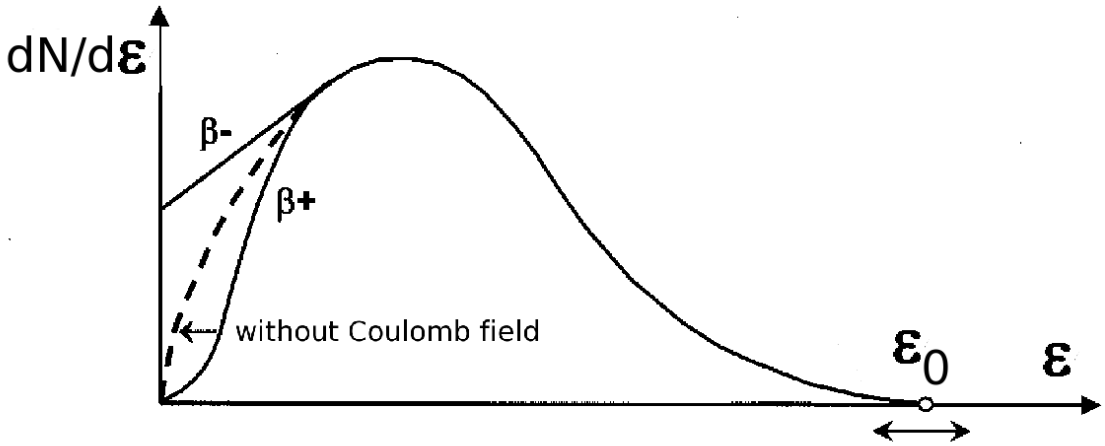

Figure 2.1: Schematic illustration of the spectra of the β^+ and the β^--decay. The spectra are shifted by the Coulomb field of the daughter nucleus. Electrons are decelerated while positrons are accelerated by the positively charged nucleus[Kri04].

To calculate the maximum electron energy, Equation 2.10 can be written as:

$$\sqrt{\frac{N(\varepsilon)}{\varepsilon \cdot (\varepsilon^2 - 1)^{1/2} \cdot F_C}} \propto (\varepsilon_0 - \varepsilon) \tag{2.11}$$

From the related graph, the so-called Fermi plot, the maximum energy can be obtained from the intersection point of the graph and the axis of abscissa [Kri04].

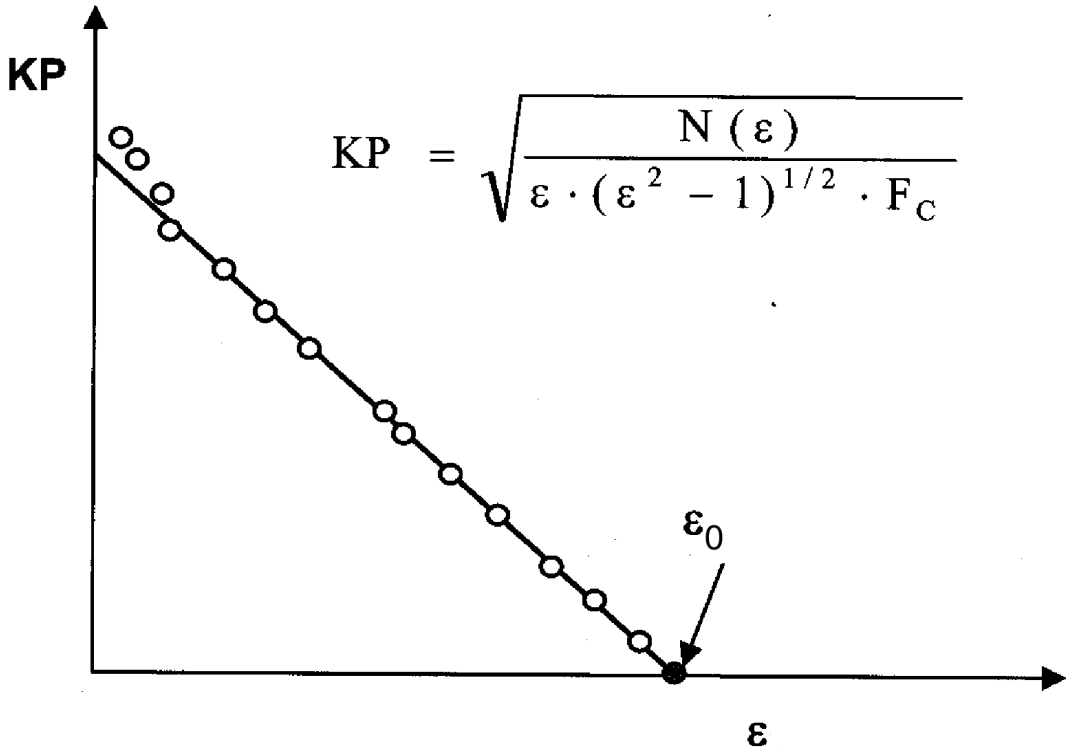

Figure 2.2: Fermi plot as calculated in Equation 2.11. F_C is the correction factor corresponding to the Coulomb potential. The reaction energy of the β-decay can be obtained from the intersection point of the plot and the axis of abscissa [Kri04].

2.2 Tracer

The idea of radio indicated diagnoses has been developed by the Hungarian chemist Georg von Hevesy who was awarded the Nobel Price in Chemistry in 1934 [Sch03b]. Radioactive tracers allow the in vivo measurement of metabolistic processes as well as perfusion and nutriment distribution.
Radioactive tracer molecules are molecules that can be found in the human, or animal body respectively, additionally marked with a radioactive isotope. They behave in the biological system exactly as their non-radioactive counter parts do; the marking with a radiating isotope allows to monitor the biochemical distribution with image reconstruction systems.
The principle of the positron emission tomography is the reconstruction of a three dimensional distribution of a radioactive isotope within the biological tissue of a mouse or a human patient. Since the reconstruction is based on the data from the β^+-decay, the image quality is improved with a growing amount of data, which corresponds to more decays being detected by the scanner. To provide a high number of β^+-decays combined with a low radiation exposure of the patient and his relatives, it is reasonable to use a radionuclide with a very short half-life. A high disintegration rate assures that a high fraction of decays happens while the patient is examined with the PET camera so that the emitted γ-particles can be used for the image reconstruction.
The demand for transient isotopes leads to another complication: the radioactive isotopes cannot be produced centrally at a production site and delivered on demand, but have to be synthesized locally at the day of deployment. Therefore the nuclear medical hospitals and research sites have to maintain a cyclotron besides the actual imaging devices to warrant a steady supply with the necessary isotopes.
Since only the light nuclei favor the β^+-decay over the electron caption reaction, the choice of optimal isotopes for PET imaging is limited [Web96]. The main isotopes that can be used are shown in Table 2.1. In this table, half-life, maximum positron energy, specific activity and the nuclear reaction that can be used to produce the isotope in a cyclotron are displayed for several isotopes.
Table 2.2 shows the different molecules that are used for the functional imaging with PET and their main purposes in the human or animal body. When the behavior of new tracer molecules can be investigated with high resolution imaging technologies, new types of diagnosis are conceivable to make better diagnoses of high accuracy.

The development of new disease-specific tracer molecules is a very important field of research in modern nuclear medicine.

Isotope	**Half-life [min]**	**Max. energy [MeV]**	**Spec. Activity [GBq/mol]**	**Reaction**
^{11}C	20.40	0.97	3.4×10^{11}	^{10}B(d,n)^{11}C ^{11}B(p,n)^{11}C ^{14}N(p,α)^{11}C
^{13}N	9.96	1.19	7.0×10^{11}	^{12}C(d,n)^{13}N ^{13}C(p,n)^{13}N ^{16}O(p,α)^{13}N
^{15}O	1.05	1.72	3.4×10^{12}	^{14}N(d,n)^{15}O ^{15}N(p,n)^{15}O
^{18}F	109.77	0.64	6.3×10^{10}	^{18}O(p,n)^{18}F ^{20}Ne(d,α)^{18}O

Table 2.1: Different sorts of positron emitting isotopes, used in PET [Wie98].

Molecule	**Purpose**
$H_2{}^{15}O,\ C^{15}O_2,\ CH_3{}^{18}F,\ C_4H_{10}{}^{15}O$	blood circulation
$^{11}CO,\ C^{15}O_2$	blood volume
$^{15}O_2$	oxygen consumption
$2-[^{18}F]-\text{Fluoro}-2-\text{deoxy}-\text{D}-$ glucose [FDG]	glucose metabolism
^{11}C−, ^{18}F-amino acid	protein synthesis
$^{18}\text{F}-\text{L}-\text{Dopa},\ ^{11}$C−, ^{18}F-spiroperidol	dopamine receptor
^{11}C-flunitrazepam	benzodiazepin receptor
^{11}C-endorphin	opiate receptor

Table 2.2: Molecules that can be used in medical PET imaging and their purpose [Web96].

2.3 Mean Range and Annihilation of Positrons in Matter

2.3.1 Positron Range in Matter

The technology of positron emission tomography does not allow a determination of the exact position of positron emission, but a determination of the exact position of the positron annihilation. Therefore the reconstruction of tracer concentration within the patients body is smeared by the mean range of the positrons in tissue, which can be regarded as water to a first approximation. The distance which the positron propagates before its annihilation is the main factor that limits the spatial resolution which can be reached with the technology of positron emission tomography. Therefore the knowledge of the positron range in biological tissue is important to evaluate the theoretical limit of the spatial resolution of a PET scanner.

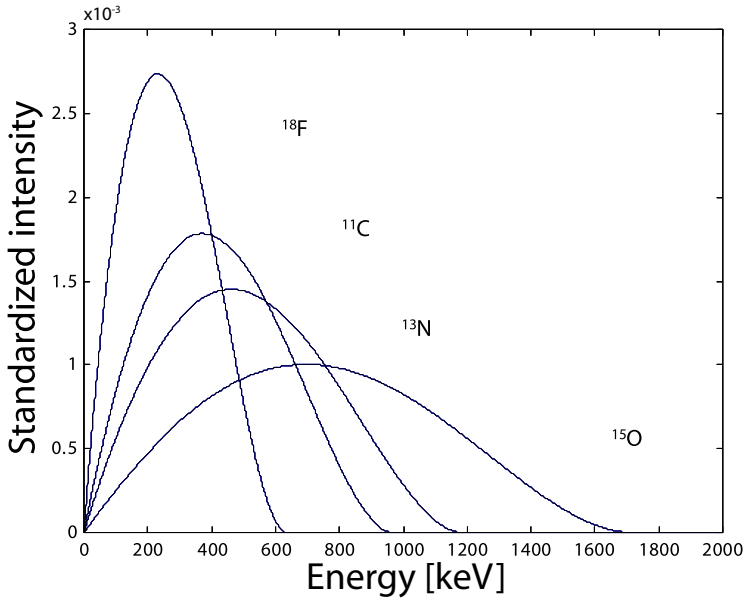

Figure 2.3: Standardized energy spectra of the most common radio nuclides in PET [Smi].

After its emission, the positron is slowed down in the surrounding tissue. While the velocity decreases, the probability for the positron to form a hydrogen-like molecular state called positronium with one of the surrounding electrons, grows. Due to this

deceleration process, the range of positrons in tissue depends on their original energy. The energy spectra of the most common radio nuclides are shown in Figure 2.3. According to [Hei53], the cross section for positrons to form a positronium with an electron from the surrounding tissue is represented by:

$$\phi = \pi r_0^2 \frac{1}{\gamma+1}\left[\frac{\gamma^2+4\gamma+1}{\gamma^2-1} + \log\left(\gamma+\sqrt{\gamma^2-1}\right) - \frac{\gamma+3}{\sqrt{\gamma^2-1}}\right], \tag{2.12}$$

where γ describes the relativistic γ-factor

$$\gamma = \left(\frac{1}{\sqrt{1-(v^2/c^2)}}\right), \tag{2.13}$$

and $r_0 = 2.82 \cdot 10^{-15}$ m is the classical electron radius. This means that the probability of annihilation increases with decreasing velocity of the positron. While the positron propagates through matter, it loses energy by scatter processes and the γ-factor mentioned above, approaches 1. Thus the cross section grows and the interaction with an electron becomes more likely. The loss of energy of the positron is described by the Bethe-Bloch formula [Leo87]:

$$-\frac{dE}{dx} = 2\pi N_a r_e^2 m_e c^2 \rho \frac{Z}{A}\frac{z^2}{\beta^2}\left[\ln\left(\frac{2m_e c^2\gamma^2\beta^2 W_{\max}}{I^2}\right) - 2\beta^2 - \delta - 2\frac{C}{Z}\right] \tag{2.14}$$

With:

r_e :	electron radius = 2.817×10^{-15} m	m_e :	electron mass = $9.10938188 \times 10^{31}$ kg
N_a :	Avogadro's number = 6.022×1023 mol^{-1}	I :	mean excitation potential
Z :	atomic number of absorbing matter	A :	atomic weight of absorbing matter
ρ :	density of absorbing matter	β :	v/c of incident particle
γ :	$1/\sqrt{1-\beta^2}$ of incident particle	z :	charge of incident particle
W_{max} :	maximum energy transfer in a single collision	C :	shell correction (accounts for the momentum of the extra nuclear electrons)
δ :	density correction (accounts for the polarizability of the medium)		

Since the mean excitation potential is not easy to calculate, one can assume a semi-empirical formula that has been fitted to the measured data of dE/dx [Leo87]:

$$\begin{aligned} \frac{I}{Z} &= 12 + \frac{7}{Z}\ \text{eV} && Z < 13 \\ \frac{I}{Z} &= 9.76 + 58.8 Z^{-1.19}\ \text{eV} && Z \geq 13 \end{aligned} \tag{2.15}$$

While the maximum range of positrons in water can easily be calculated using the Bethe-Bloch-formula described above, it is rather difficult to calculate or measure the mean range of positrons in water for different energies. Different authors give values that differ from each other by up to one order of magnitude. Table 2.3 presents the reaction energy, the most probable positron energy and the path length for electrons of the maximum energy for different isotopes that are relevant for the positron emission tomography. The path length, which is not to be mistaken with the penetration depth, is derived from the integral of the reciprocal of the stopping power which is the continuous slowing down approximation range (R_{CSDA}).

Isotope	**Max. energy [MeV]**	**Most probable energy [MeV]**	**R_{CSDA} in water [mm]**
^{11}C	0.959	0.326	5.0
^{13}N	1.197	0.432	5.4
^{15}O	1.738	0.696	8.2
^{18}F	0.633	0.203	2.4

Table 2.3: Reaction energy, most probable positron energy and continuous slowing down approximation range for electrons of the same reaction energy for the most common positron emitting isotopes used for PET as measured in [Cho75].

Furthermore, Table 2.4 gives the FWHM[3] and FWTM[4] values for the mean positron range in water, measured by Cho et al. [Cho75], the same ranges obtained from a Monte Carlo[5] calculation that has been validated experimentally by Levin and Hoffman [Lev99] and the mean positron range, given by Bailey et al. [Bai03] and Humm et al. [Hum03].

	[Cho75]		[Lev99]		[Bai03]	[Hum03]
Isotope	**Range FWHM [mm]**	**Range FWTM [mm]**	**Range FWHM [mm]**	**Range FWTM [mm]**	**Mean Range [mm]**	**Mean Range [mm]**
^{11}C	1.11	2.19	0.188	1.86	1.1	1.7
^{13}N	1.42	2.78	0.282	2.53	1.5	2.0
^{15}O	1.49	3.57	0.501	4.14	2.5	2.7
^{18}F	1.02	1.8	0.102	1.03	0.6	1.4

Table 2.4: Range FWHM, FWTM and mean range for the most common positron emitting isotopes used for PET from different authors.

Although a precise answer to the mean positron range in biological tissue cannot be given from these contradictory data, it can be said that the mean positron range is on the order of 1 mm. According to this, the maximum spatial resolution that can be reached by PET scanners is about 1 mm and devices with a spatial resolution which is much better than 1 mm would not be reasonable.

[3]FWHM: Full Width at Half Maximum. The FWHM is a measure of the distribution width of Gaussian distributions. It describes the width of the Gaussian distribution at the half of its maximum. The FWHM is larger than the commonly used σ and it can be shown to be $FWHM = 2\sigma\sqrt{2\ln 2} = 2.35\,\sigma$ [Leo87].

[4]Full Width at one-Tenth Maximum. The definition is equivalent to the definition of the FWHM.

[5]Monte Carlo: Monte Carlo methods are a widely used class of mathematical methods that intend to simulate the behavior of physical systems that cannot be described by numerical methods. Especially systems with several coupled degrees of freedom can be determined with these mathematical procedures. By calculating a large number of processes, the behavior of the simulated systems are determined stochastically.

2.3.2 Positron Annihilation

Positrons are particles of antimatter which means that they are highly reactive when exposed to the related particle of matter, the electron. As described above, the cross section goes up as the relative speed of the two particles goes down. Therefore the positron has to be decelerated to a kinetic energy of a few eV before the annihilation can occur. When the positron has lost most of its kinetic energy, a hydrogen like bound state called positronium (Ps) is formed for 98% of the positrons; two percent of the positrons hit an electron and annihilate in flight [Sem72].
If the spins of electron and positron are oppositely directed, the positronium is in a ${}^1S$ singlet state; the ${}^3S$ triplet state that is formed when the spins are parallel, has a larger energy and lifetime. The lifetime of the ${}^1S$ state, which is also called para-positronium, is $\tau({}^1S) \simeq 1.25 \times 10^{-10}$ s and the lifetime of the ${}^3S$ state, called ortho-positronium, is $\tau({}^3S) \simeq 1.4 \times 10^{-7}$ s [Ber79]. Shortly after the formation of the positronium, the two β-particles annihilate and the total energy of the electron-positron system is transferred into two photons (para positronium) that leave the vertex with an angle of 180° in the center of mass system. The ortho positronium decays into 3 photons that leave the vertex with an angle of 120°. The ratio of 2γ-decays to 3γ-decays is $\frac{1}{372}$ [Sch92]. As only 0.3% of the decays happen with an angle of 120°, the 3γ-decays are neglected and all the events are reconstructed as if all the photons left the vertices with an angle of 180°. In theory even decays with more than three photons are possible. However, these decays are so unlikely that they can be disregarded [Sch92].
Since the positron still has a kinetic energy of a few eV at the time of its annihilation, the angle with which the photons leave the vertex should differ from the exact value of 180°. This can be tested experimentally by measuring the angle between the trajectories of the two photons in the laboratory coordinate system. According to [Col65], the discrepancy between the actual angle in the lab system and the angle of 180°, respectively 120°, in the center of mass system, constitutes less than 0.28° as a general rule. Since this deviation from the theoretical angle between the two trajectories cannot be measured by a PET scanner, it is neglected and the reconstruction algorithms of common PET cameras assume an angle of exactly 180°.

2.4 Interactions of Gamma Radiation in Matter

2.4.1 Photoelectric Effect

Principle of the Photoelectric Effect

The photoelectric effect, for whose theoretical interpretation Einstein was awarded the Nobel Price in Physics in 1921, is the dominating way of photon-matter interaction for low photon energies. Here, an extra nuclear electron is hit by an incident photon. The total photon energy is transferred to the electron and the photon is absorbed. Following this, the electron energy exceeds its binding energy and is liberated from the electron shell. The recoil energy of the atom is negligible due to the high mass ratio. The energy of the liberated electron can be determined to be:

$$E_{kin} = E_\gamma - E_B \tag{2.16}$$

Here E_B represents the binding energy of the electron and E_γ represents the energy of the incident photon. This Equation clarifies that the photon has to have a minimum energy for the photoelectric effect to happen. This minimum energy that is necessary to liberate an electron is exactly the binding energy. Figure 2.4 shows a schematic illustration of the photoelectric effect that is not drawn to scale.

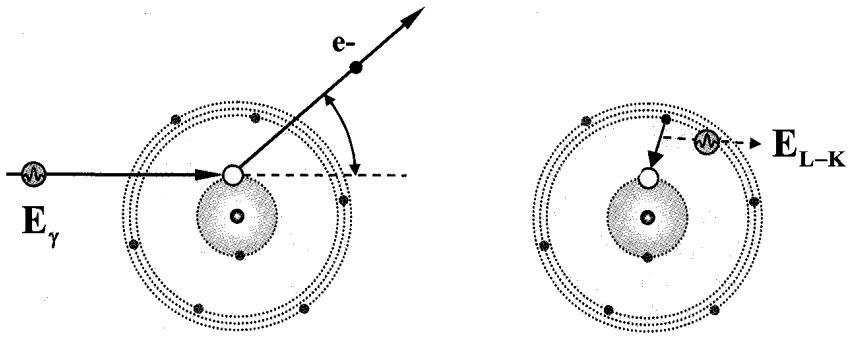

Figure 2.4: Schematic illustration of the photoelectric effect [Kri04].

As illustrated in Figure 2.5, the total cross section for the photoelectric effect mainly matches with the cross section of the photoelectric effect occurring with K-shell electrons for energies above the highest binding energies [Leo87]. This means that

the electron which is liberated by the photoelectric effect is almost always an electron from the K-shell for photon energies above the binding energy of the K-shell electrons. For these electrons the cross section for a photoelectric reaction can be described as follows [Bet01]:

$$\sigma^{K}_{\text{Photo}} = \left(\frac{32}{\varepsilon^7}\right)^{1/2} \alpha^4 Z^5 \sigma^{e}_{Th} \ (\text{cm}^2/\text{Atom}) \tag{2.17}$$

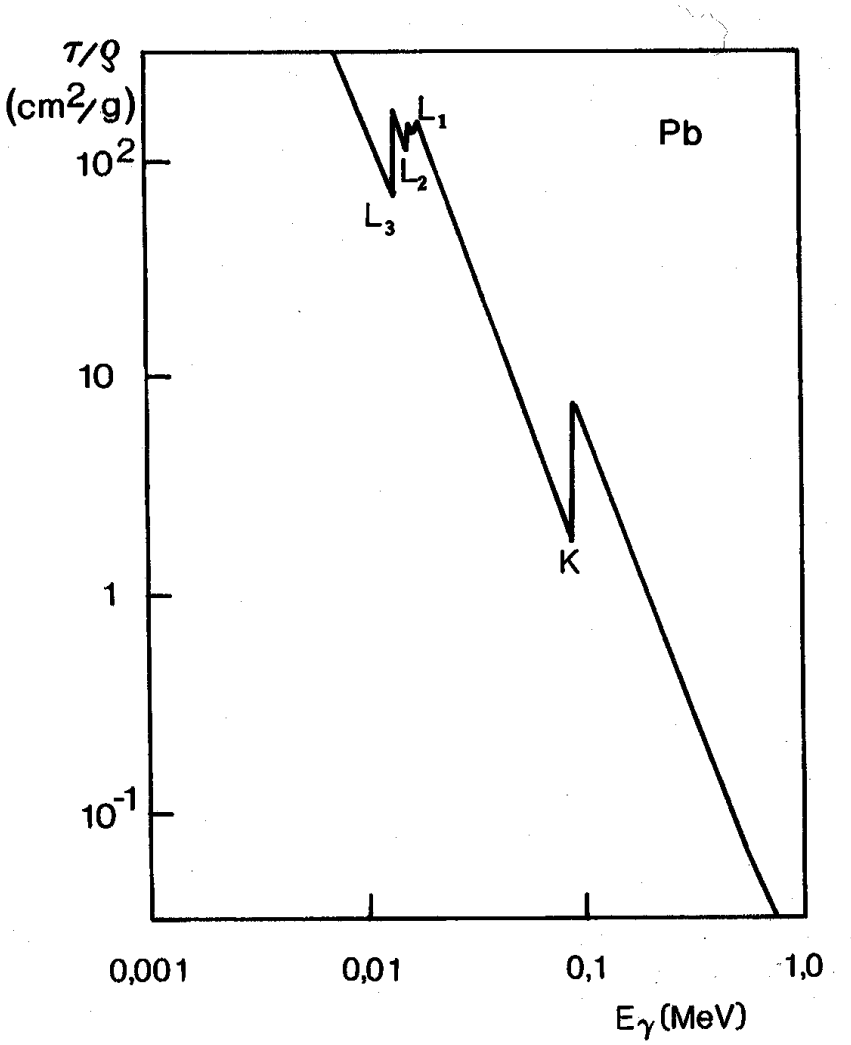

Figure 2.5: Photo absorption coefficient for lead. The absorption edges of the K and L electron shells are easily identified [Kri04].

With the reduced photon energy

$$\varepsilon = E_\gamma / m_e c^2, \tag{2.18}$$

the Sommerfeld fine-structure constant

$$\alpha = \frac{e^2}{4\pi\varepsilon_0 \hbar c}, \tag{2.19}$$

the atomic number Z and the Thomson cross section

$$\sigma_{Th}^e = \frac{8}{3}\pi r_e^2 = 6.65 \cdot 10^{-25}\ \mathrm{cm}^2. \tag{2.20}$$

Angular Distribution of the Electron Emission

The liberated photoelectrons are neither all emitted in the same direction, nor is the angular distribution isotropic. The distribution of emitted electrons, which varies with the energy of the incident photon, can be calculated. According to [Kri06] and [Sau31], using relativistic considerations by assuming that $\beta = \frac{v}{c} \sim 1$ and that $\frac{Z}{137} \ll 1$, the angular distribution of the photoelectrons can be written as:

$$\begin{aligned} dI = Jd\Omega &\sim \beta^2 \sin^2\theta \cdot \\ \cdot &\left\{ \frac{(1-\beta^2)^{\frac{1}{2}} \cos^2\varphi}{(1-\beta\cos\theta)^4} - \frac{[1-(1-\beta^2)^{\frac{1}{2}}]\cos^2\varphi}{2(1-\beta^2)^{\frac{1}{2}}(1-\beta\cos\theta)^3} + \frac{[1-(1-\beta^2)^{\frac{1}{2}}]}{4(1-\beta^2)(1-\beta\cos\theta)^3} \right\} d\Omega \end{aligned} \tag{2.21}$$

In this equation Ω represents the solid angle, φ is the zenith and θ is the azimuth. The plotted angular distribution can be seen in Figure 2.6 for γ-energies of 100 keV, 250 keV, 511 keV, 1 MeV and 1.5 MeV. Since the fraction $\beta = \frac{v}{c}$ has a value of $\frac{\sqrt{3}}{2}$ for 511 keV electrons, these assumptions fit rather well and Davisson and Evans [Dav52] showed that Equation 2.21 describes the data measured by Lutze [Lut31] very good, even for electron energies of as low as 90 keV.

2.4.2 Compton Effect

Besides the photoelectric effect, a second way of interaction of photons with extra nuclear electrons of the surrounding matter becomes more important for higher photon energies (Figure 2.7): The Compton effect (Figure 2.8).

Contrary to the photoelectric effect, the photon is not absorbed in the Compton effect. Instead it transfers a fraction of its energy to the participating electron. Since

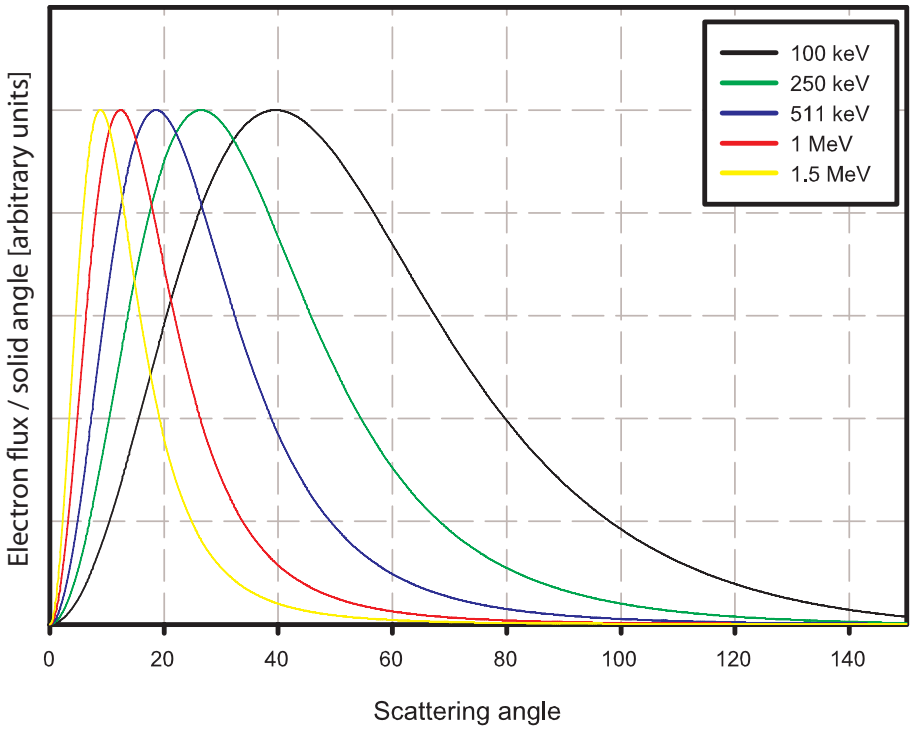

Figure 2.6: Angular distribution of electrons emitted by the photoelectric effect in arbitrary units. The data corresponds to Equation 2.21

the binding energy of the electron is small compared to the photon energy it can be neglected and the process can be considered as an elastic scattering [Bet01]. Following this consideration, the electron is liberated and the photon is scattered by the angle of φ with respect to its original trajectory. A schematic illustration of this process is given in Figure 2.8.

For the theoretical interpretation, relativistic collision kinematics are assumed: The photon energy is $E_\gamma = h\nu$, while its momentum can be written as $p_\gamma = \frac{E_\gamma}{c} = \frac{h}{\lambda}$. The energy of the electron is E, its rest mass is $m_e c^2$ and its momentum is given by $\vec{p_e}$. With that, the energy and momentum conservation laws predict:

$$E_\gamma + m_e c^2 = E'_\gamma + E_e \tag{2.22}$$

$$\vec{n} \cdot \frac{E_\gamma}{c} = \vec{n}' \cdot \frac{E'_\gamma}{c} + \vec{p_e} \tag{2.23}$$

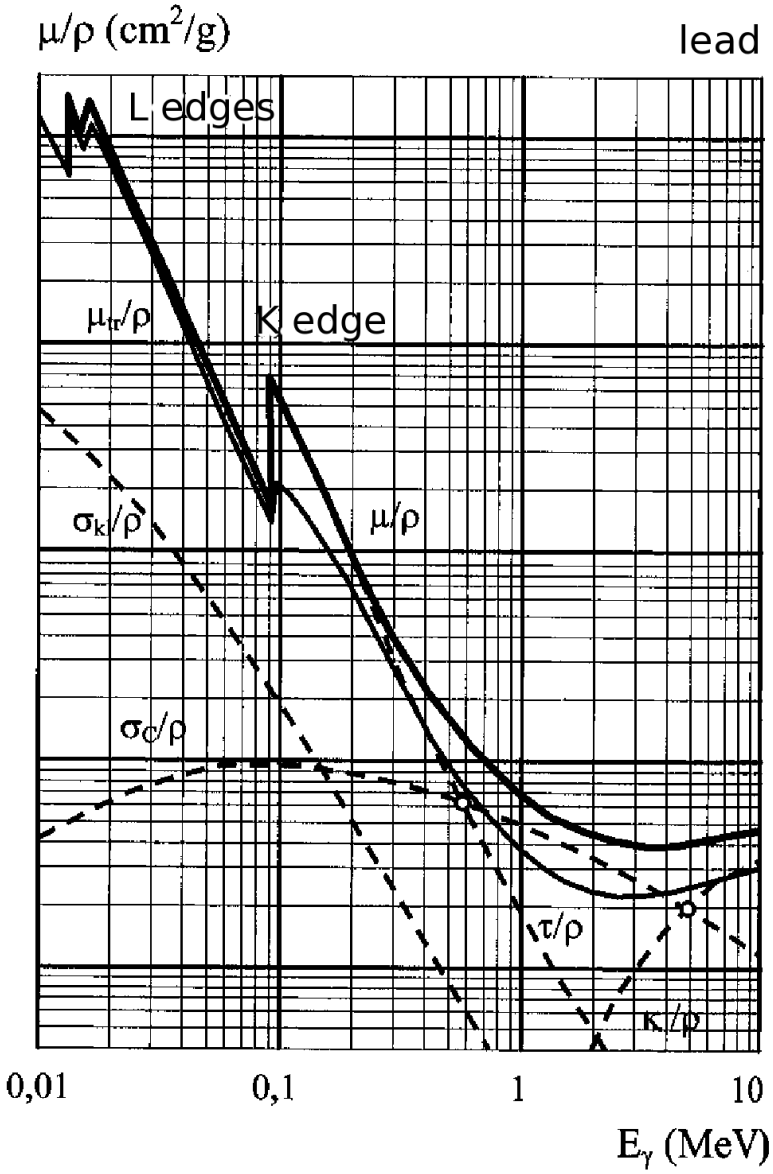

Figure 2.7: Mass attenuation coefficient of lead. The upper line represents the total mass attenuation coefficient; the dashed lines represent its components. The fractions of photoelectric effect (μ_τ/ρ), Compton effect (σ_C/ρ), pair production (κ/ρ) and coherent scattering (σ_{kl}/ρ)) are clearly distinguishable [Kri04]. With increasing photon energies the Compton effect becomes more important besides the photoelectric effect.

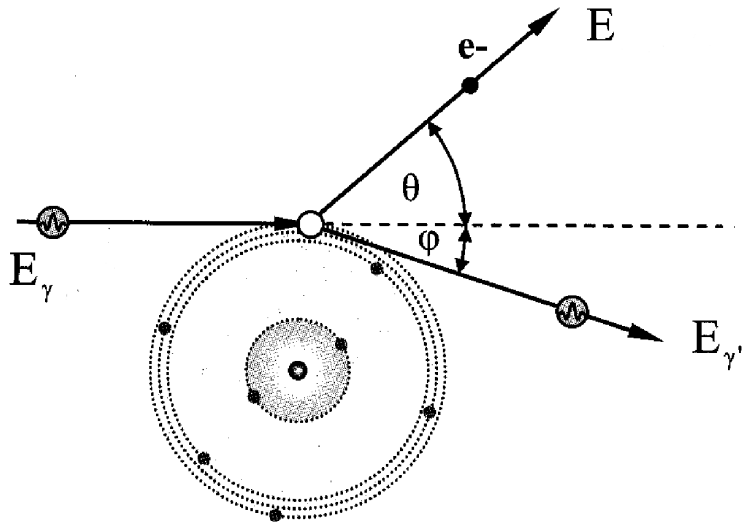

Figure 2.8: Phenomenological illustration of the Compton effect [Kri04].

$\vec{n}$ and $\vec{n}'$ are the normalized vectors in the direction of the photon trajectory before and after the scattering respectively. The angle between these vectors is φ. Both equations are squared and the momentum formula is subtracted from the energy formula. This leads to the following relations:

$$(E_\gamma - E_\gamma^{'})^2 + 2m_e c^2(E_\gamma - E_\gamma^{'}) + m_e^2 c^4 = E^2 \tag{2.24}$$

$$E_\gamma^2 - 2E_\gamma E_\gamma^{'}\cos\varphi + E_\gamma^{'2} = {p_e}^2 c^2 \tag{2.25}$$

$$\Rightarrow \qquad E_\gamma E_\gamma^{'}(1-\cos\varphi) - m_e c^2(E_\gamma - E_\gamma^{'}) = 0 \tag{2.26}$$

With these equations the change of the photon wavelength during the Compton effect can be determined:

$$\Delta\lambda = \lambda^{'} - \lambda = \frac{h}{m_e c}(1-\cos\varphi) = \lambda_C \cdot (1-\cos\varphi) \tag{2.27}$$

The constant $\lambda_C = \frac{h}{m_e c}$ is called the Compton wavelength. By rewriting this equation, an equation for the kinetic energy of the electron and thereby for the energy loss of the photon can be calculated:

$$E_{kin} = E - m_e c^2 = h\nu \frac{\frac{h\nu}{m_e c^2}(1 - \cos\varphi)}{1 + \frac{h\nu}{m_e c^2}(1 - \cos\varphi)} \tag{2.28}$$

So, the remaining energy reads:

$$E_\gamma^{'} = \frac{h\nu}{1 + \frac{h\nu}{m_e c^2}(1 - \cos\varphi)} \tag{2.29}$$

According to O. Klein and Y. Nishina, the total cross section per electron for this reaction is [Nis29]:

$$\begin{aligned} \sigma_C^e &= 2\pi r_e \left\{ \left(\frac{1+\varepsilon}{\varepsilon^2} \right) \left[\frac{2(1+\varepsilon)}{1+2\varepsilon} - \frac{1}{\varepsilon} \ln(1+2\varepsilon) \right] + \right. \\ &\quad \left. + \frac{1}{2\varepsilon} \ln(1+2\varepsilon) - \frac{1+3\varepsilon}{(1+2\varepsilon)^2} \right\} (\mathrm{cm}^2/\mathrm{electron}) \end{aligned} \tag{2.30}$$

To simplify matters, the abbreviation $\varepsilon = {E_\gamma}/{m_e c^2}$ is established. This equation gives the total cross section per electron. By multiplying Equation 2.30 with the atomic mass number Z, one obtains the total cross section per atom:

$$\sigma_C^{\mathrm{atomic}} = Z\sigma_C^e \tag{2.31}$$

To calculate an energy distribution of the Compton electrons, the cross section for electrons being scattered in the energy range $\mathrm{d}T_e$ will be determined:

$$\begin{aligned} \frac{\mathrm{d}\sigma_\mathrm{C}}{\mathrm{dT_e}} &= \frac{\pi r_e^2}{\frac{(h\nu)^2}{m_e c^2}} \left\{ 2 + \left(\frac{T}{h\nu - T} \right)^2 \cdot \right. \\ &\quad \left. \cdot \left[\left(\frac{m_e c^2}{h\nu} \right)^2 + \frac{h\nu - T}{h\nu} - \frac{2 m_e c^2}{h\nu} \left(\frac{h\nu - T}{T} \right) \right] \right\} \end{aligned} \tag{2.32}$$

At the upper end of the energy spectrum, this cross section shows a clearly to identify maximum, called Compton edge. The Compton edge lies below the photon energy

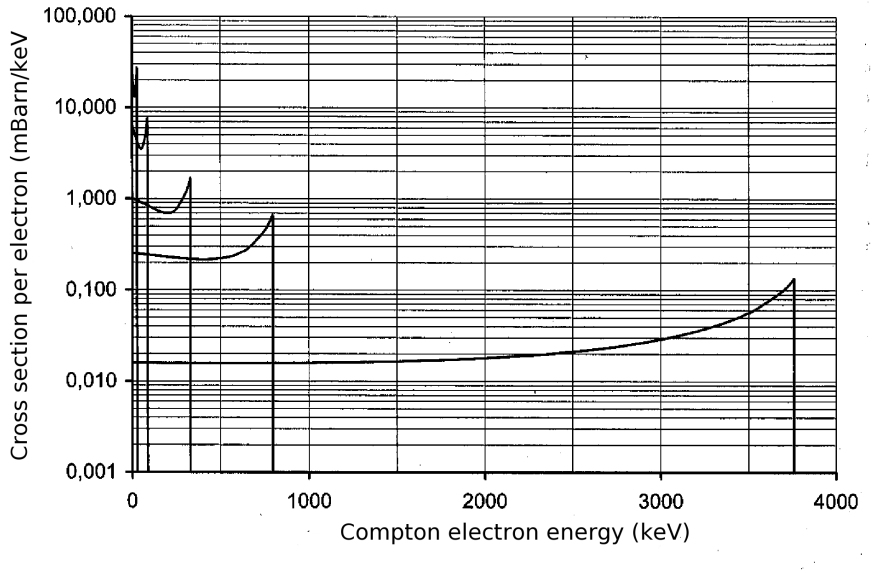

Figure 2.9: The energy distributions of the Compton electrons show sharp edges that refer to the photon energies of 100, 200, 500, 1000 and 4000 keV [Kri04].

because only a fraction of the photon energy is transferred to the electron. Figure 2.9 shows the cross section with the Compton edge for different photon energies. Referring to Equation 2.28 and the relativistic collision kinematics, this maximal electron energy occurs when the electron is hit head-on by the photon. Referring to [Bet01], the maximal electron energy lies at 340 keV for 511 keV photons.

Angular Distribution of the Electron Emission

As it has been done for the photoelectrons, the angular distribution of the Compton electrons can be determined. Due to the momentum conservation law, the Compton electrons can only be accelerated parallel or perpendicular to the photon trajectory but never anti-parallel. Therefore the angular distribution of the electrons becomes zero for angles in backward directions. The Klein-Nishina cross section provides the following expression:

$$\frac{d\sigma_e}{d\theta} = \frac{d\sigma_e}{d\Omega} \cdot \frac{2\pi(1+\cos\varphi)\cdot\sin\varphi}{\left(1+\frac{E'_\gamma}{m_0c^2}\right)\cdot\sin^2\theta} \tag{2.33}$$

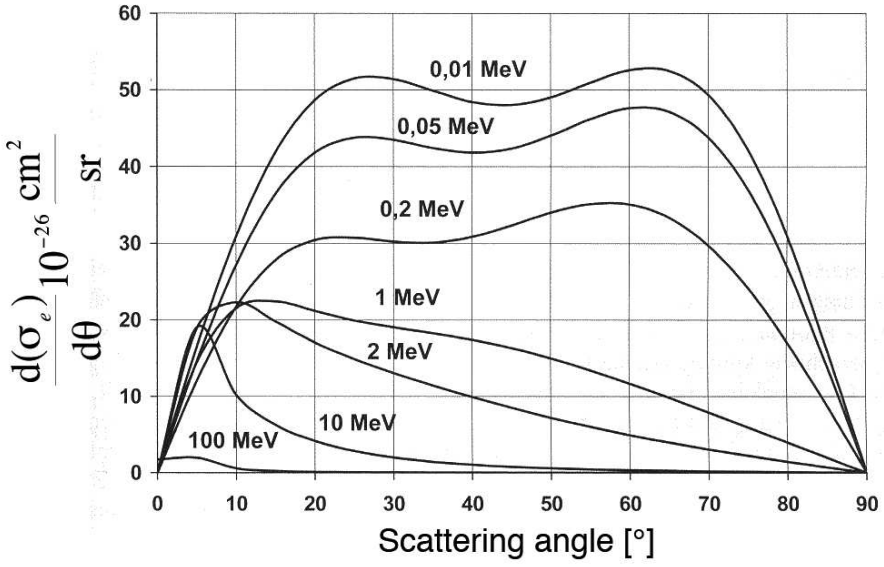

Figure 2.10: Angular distribution of the Compton electrons for different photon energies [Kri04].

The corresponding graph is shown in Figure 2.10. Two maxima can be identified for photon energies below 1000 keV. For energies above 1 MeV, the distribution deforms to a peak in forward direction.

3. Multiwire Proportional Chambers

Proportional counters were introduced in the late 1940s. These gas filled detectors are based on the charge amplification of the original ion pairs that are created by incoming radiation which ionizes the counting gas.
Since these detectors multiply the number of primary ion pairs, they are common in situations in which the number of primary ion pairs is too small to assure a sufficient detection probability for the direct radiation detection. Proportional chambers are therefore often used for the detection of low energy X-rays or charged particles.
Proportional counters usually consist of a thin anode wire and a cylindrical or planar shaped cathode. Incoming radiation ionizes the counting gas the detector is filled with. Due to the applied high voltage, usually on the order of several kV, the electrons that are liberated drift towards the anode wire. When they reach a region, in which the electric field strength is high enough to accelerate the electrons to an energy above the ionizing threshold of the counting gas, secondary ionization will occur as the electrons collide with gas atoms. With every collision more electrons are liberated and cause a gas multiplication process, which forms a cascade known as the Townsend avalanche [Kno79].
The avalanche stops when all ejected electrons have been collected at the anode. By choosing a voltage in the proportional region (see Figure 3.1), the number of collected electrons can be kept proportional to the number of primary ion pairs formed. Depending on the applied voltage, different modes of operation can be distinguished. These regions can be seen in Figure 3.1.
For very low voltages, the electric field is insufficient to prevent the ion pairs from recombination. The charge that is collected at the anode wires is less than the charge of the original ion pairs. As the applied voltage is increased, a region of constant amplification is formed. On this plateau, the collected charge corresponds to the charge of original ion pairs. When the voltage is increased further, the region of proportionality is reached. Here, the collected charge is proportional to the amount of original ion pairs. The observed pulse amplitude allows to reconstruct the number of created ion pairs although the charge has been greatly amplified.

Due to this amplification even low energetic particles can be detected with high accuracies. For even higher voltages, nonlinear effects are of growing importance. The most important of these effects is the formation of charge clouds of positive ions that slowly drift towards the cathode. When the charge amplification increases, these ion clouds significantly deform the shape of the electric field around the anode wires. The newly produced ion pairs are shielded from the electric field by this effect. The pulse amplitude, although still increasing with an increasing number of created ion pairs, does not show a proportional behavior. The Geiger-Mueller region does not allow a reconstruction of the number of original ion pairs at all. Multiple avalanches occur along the entire wire until a critical number of positive charges has been created and the avalanches are disrupted, regardless of the number of initial ions. Therefore all pulses obtained from a Geiger-Mueller tube have the same amplitude and only the intensity of the incident radiation can be determined.

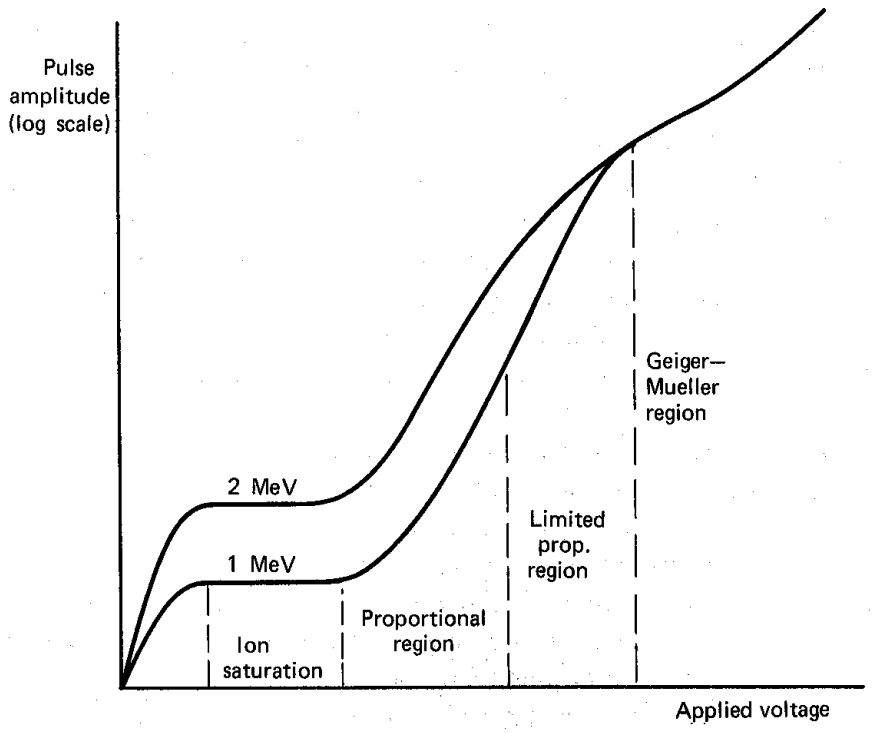

Figure 3.1: The different regions of operation of gas filled ionizing detectors [Kno79].

3.1 Basics on Proportional Counters

3.1.1 Proportional Counters Tubes

The simplest sort of proportional counters is the proportional counter tube. To generate the sufficiently high electric field that is required for the gas amplification, the proportional counter tube is constructed with a cylindrical geometry. In the center, along the axis of the cylinder, a thin anode wire is mounted. The tube shaped cylinder itself serves as the cathode (see Figure 3.2.) By applying a high voltage of several kV, typically 1 - 10 kV depending on the geometry, the electric field that induces the gas amplification is created.

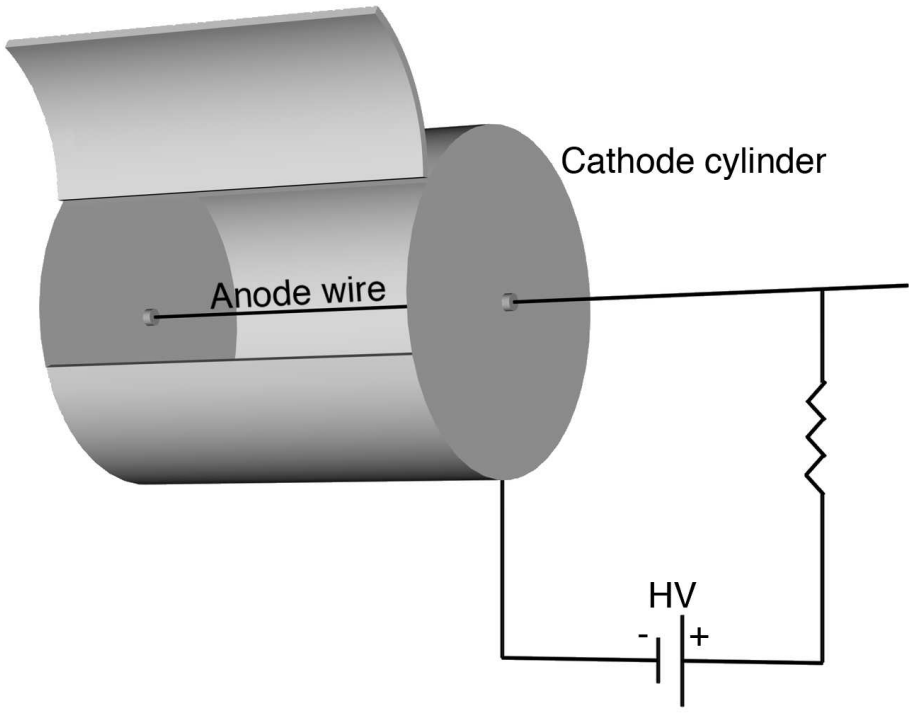

Figure 3.2: Simple geometry of a proportional counter tube. In this image, the cylindrical proportional counter was opened to see the inner architecture.

In this simple geometry the electric field at a given distance r of the anode wire is represented by the following formula:

$$E(r) = \frac{V}{r \ln(b/a)} \tag{3.1}$$

where V is the applied voltage, a the wire radius and b the inner cathode radius. The formula implies that the electric field increases with decreasing distance from the anode wire. Thereby the electrons are accelerated towards the regions of high electric strength where the multiplication takes place. In typical gas mixtures the threshold for the electric field to allow gas multiplication is about 10^6 V/m [Kno79].

3.1.2 Gas Amplification

When an incoming ionizing particle interacts with one of the gas molecules and an ion pair is produced, the electron is accelerated towards the anode wire. Between two interactions, the electron gains the energy of:

$$\begin{aligned} \Delta T_{kin} &= e \int_{r_1}^{r_2} E(r) dr \\ \Delta T_{kin} &= e U_0 \frac{\ln\left(\frac{r_2}{r_1}\right)}{\ln\left(\frac{b}{a}\right)} \end{aligned} \tag{3.2}$$

If the kinetic energy exceeds the ionization energy of the counting gas, the electron is able to ionize other atoms; secondary ionization begins and a Townsend avalanche occurs. By colliding with other atoms before their kinetic energy reaches the threshold value, the secondary electrons are scattered before they can ionize other atoms and so the avalanche spreads all around the wire. Figure 3.3 demonstrates the evolution of a Townsend avalanche. A Monte Carlo simulation of such an avalanche is represented in Figure 3.4 [Net91].
The pulse that originally consisted of just a couple of ion pairs is amplified by the gas multiplication factor M.

$$\Delta U = \frac{-MNe}{C} \tag{3.3}$$

N is the number of ion pairs created and C is the capacity of the cylindrical tube. The proportional region is defined as the region of electric field strength and gas pressure, in which M is constant and the pulse height is proportional to the number of primary ion pairs. By optimizing the voltage setting, it is possible to achieve an amplification factor of $10^4 - 10^6$.

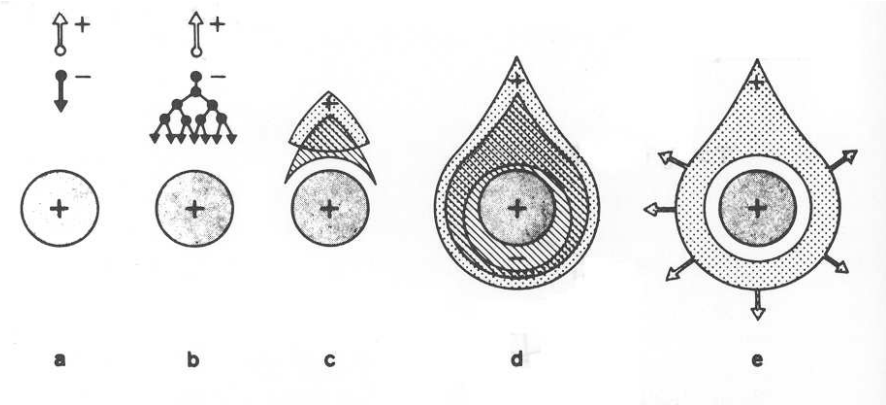

Figure 3.3: a) The primary ion pair is separated by the electric field and the recombination is avoided. b) The primary electron gains energy and exceeds the ionization energy of the counting gas. c) The secondary ions are prevented from recombination. The electrons drift towards the anode, the positive ions accelerate towards the cathode. d) and e) The electrons reach the anode, the heavier and slower ions slowly drift away [Kle92].

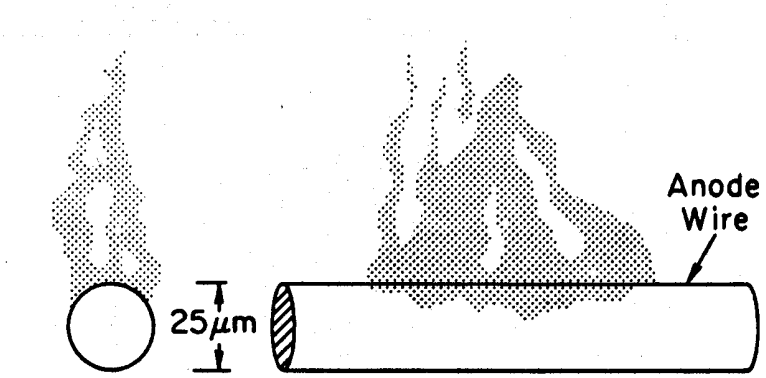

Figure 3.4: Monte Carlo simulation of a Townsend avalanche. The charge of the primary ion pairs is amplified by secondary ionizations and collected at the anode wire [Net91].

The number of ionizations which are produced in relation to the propagated distance is called the first Townsend coefficient α.

$$\alpha = \sigma_i \cdot N \tag{3.4}$$

The cross section σ_i is exemplarily shown in Figure 3.5.

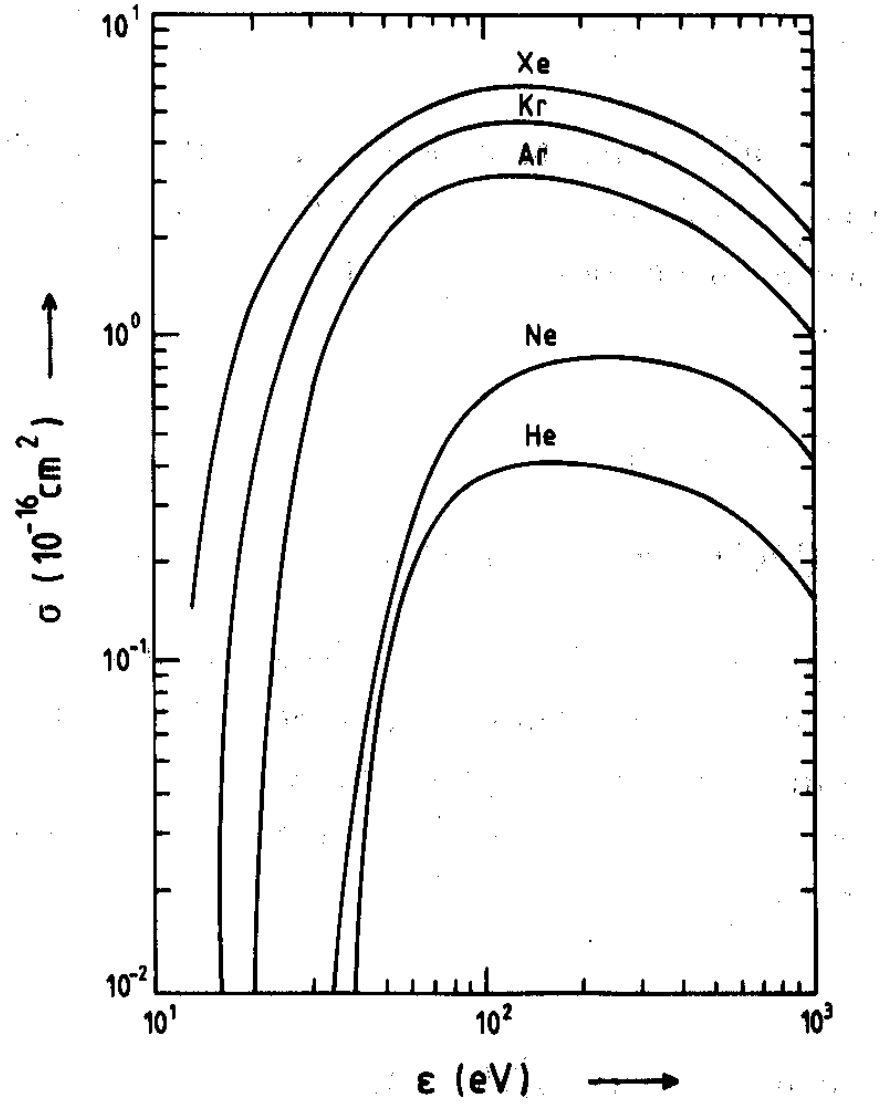

Figure 3.5: Cross section of the first Townsend coefficient as a function of the electron energy for different noble gases, used in MWPCs [Sau77].

With that first Townsend coefficient the gas multiplication factor M can be written as:

$$\ln M = \int_a^{r_c} \alpha(r) dr \qquad \text{[Kle92] and [Kno79]} \tag{3.5}$$

The integration is carried out from the anode radius a to the critical radius r_c. This radius defines the threshold of the electric field strength to support gas multiplication. Using Equation 3.1, one can derive an expression for M:

$$\ln M = \frac{V}{\ln(b/a)} \int_{E(a)}^{E(r_c)} \frac{\alpha(E)}{E} \frac{dE}{E} \tag{3.6}$$

With the assumption of a linear coherence between α and E, Diethorn has derived:

$$\ln M = \frac{V}{\ln(b/a)} \frac{\ln 2}{\Delta V} \left[\ln \frac{V}{pa \ln(b/a)} - \ln K \right] \qquad \text{[Kno79]} \tag{3.7}$$

Where p is the gas pressure, ΔV is the voltage the electrons propagate through between two ionizing events and K represents the threshold value for E/p.
Wolff has proven the applicability of this equation to several conventional fill gases, shown in Table 3.1 [Wol74].

3.1.3 Fill Gases

According to [Sau77], avalanche multiplication occurs in every gas. The reasons for the choice of one specific gas are experimental ones. Some gases or gas mixtures provide e.g. a long lifetime, short recovery time, low working voltage and good proportionality, compared to others.
It has been shown that due to lots of non-ionizing energy modes, molecular gases cannot provide avalanche multiplication at such a low voltage threshold as noble gases can. Therefore noble gases are usually chosen for the main component to fill the detector. Aiming for a high specific ionization and including economical considerations, one usually chooses argon. The problem with argon, however, is the high excitation energy. Within an avalanche, ionized and excited atoms are produced. The excited atoms can only return to the ground state by emitting a photon, which has a minimum energy at 11.6 eV. This energy is well above the ionization energy of

Gas mixture	$K[10^{-4}(\mathrm{V/cm \cdot atm})]$	ΔV[eV]
90% Ar, 10% CH_4 [P - 10]	4.8	23.6
95% Ar, 5% CH_4 [P - 5]	4.5	21.8
100% CH_4 [methane]	6.9	36.5
100% C_3H_8 [propane]	10.0	29.5
90% He, 4% [isobutane]	1.48	27.6
75% Ar, 15% Xe, 10% CO_2	5.1	20.2
69.4% Ar, 19.9% Xe, 10.7% CH_4	5.45	20.3
64.6% Ar, 24.7% Xe, 10.7% CO_2	6.0	18.3
90% Xe, 10% CH_4	3.62	33.9
95% Xe, 5% CO_2	3.66	31.4

Table 3.1: Parameters for several common fill gases [Wol74].

the metallic cathode (e.g. 7.7 eV for Cu). Thereby photoelectrons are liberated from the cathode and initiate a new avalanche. Depending on the applied voltage, the consequence is either a permanent discharge, which makes the detector inoperative, or a gain factor of about $10^3 - 10^4$, which makes the detector inefficient for the detection of low-energy particles.
Another problem using noble gases like argon is the secondary emission of photons from the cathode. When an argon atom is ionized, the electron drifts towards the anode and the heavy ion moves slowly towards the cathode. When reaching the cathode, the ion is neutralized by accepting an electron. The balance energy is liberated by emission of a photon or by secondary emission of a second electron from the cathode. Both effects cause a permanent discharge in the proportional chamber, even when it is operated with a moderate gain.
The advantage of complex molecules is that the excited energy states mentioned above allow these molecules to absorb photons in a wide energy range. Methane for example is a very efficient absorber of photons with an energy of 7.9 eV to 14.5 eV. This means that methane is able to absorb most of the photons which are emitted by electrons of the argon atoms when returning to their ground state. The efficiency of this quenching effect increases with the complexity of the molecule. By allowing even more excited energy states, the energy range of absorbed photons widens and more photons are captured.

When being neutralized, the radicals usually form simple molecules or polymerize to larger organic complexes. Somehow or other, no secondary electrons are liberated and a secondary avalanche is inhibited.
Adding even little concentrations of these molecular quenching gases to the noble gases allows to avoid permanent discharges and therefore to reach higher gains of about $10^5 - 10^6$. A major problem when using a molecular gas to quench secondary

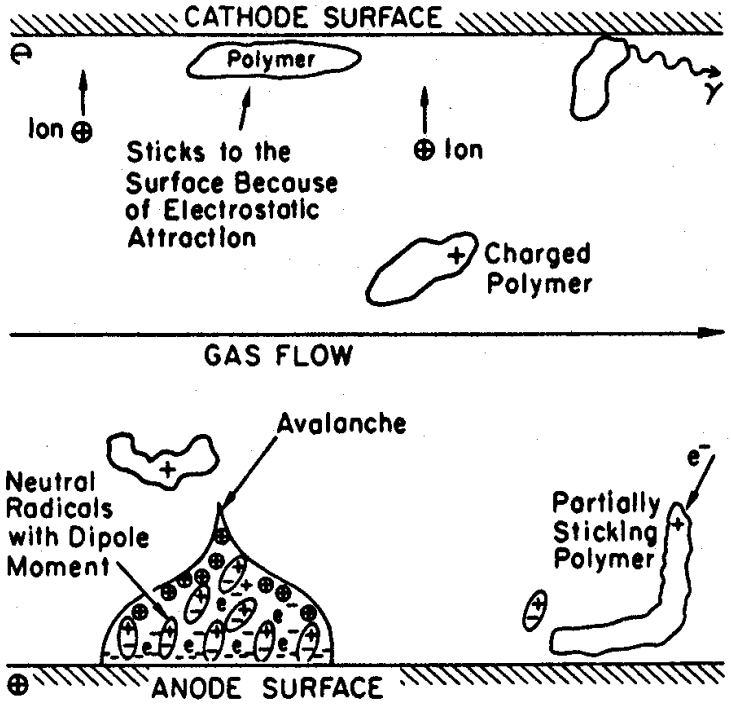

Figure 3.6: Deposition of a crust of polymers. The result of a thick crust of polymers on the cathode is a constant discharge. To grant a stable charge multiplication again, the detector has to be cleaned to remove the crust [Deu92].

avalanches is the disposal of polymers on the cathode as well as the consumption of the quencher. As mentioned before, the molecules tend to form polymers when neutralizing on the cathode. These polymers may be fluid or solid, and therefore build a thin insulating crust on the cathode. When this crust grows, the ions have to leak through and the drift speed is lowered. When the ion production rate exceeds

the leaking rate, a high density layer of charge is created around the cathode. When the density of ions gets high enough, electrons can be extracted through the crust. The resulting discharge can be stopped by lowering the applied voltage, but will resume when applying a high voltage again. The damaged detector has to be cleaned to remove the crust and grant a stable multiplication again.
Small organic molecules or CO_2 can suppress the polymerization induced aging effects, but the obtained quenching is not as efficient as the one achieved with more complex gases. Especially in modern accelerator systems, the event rate is too high to use these inefficient quenchers. For these applications organic gases with a very low ionization energy like propylic alcohol [C_3H_7OH] or methylal [$(OCH_3)_2CH_2$] are used.
To provide optimal signals for particle detection without constant discharges, usually a mixture of two gases is chosen to fill the chamber. A noble gas for the particle detection by building electron-ion pairs and an organic gas or CO_2 for the quenching of discharges. Some of the most common gas mixtures are listed in Table 3.1.

3.2 Multiwire Proportional Chambers

3.2.1 Geometry of Multiwire Proportional Chambers

To construct a position sensitive proportional counter with a large surface, one can combine a large number of anode wires to create a grid of wires between two flat plates, which serve as cathodes. This kind of radiation detector was presented by Charpak (et al.) in 1968 [Cha68], who has been rewarded the Nobel Price in Physics in 1992 [Nob07]. It has been shown that multiple parallel wires, arranged close to each other, surrounded by two cathode plates, behave like independent proportional counter tubes. Such a construction is shown in Figure 3.7. The related electric field can be seen in Figure 3.8.

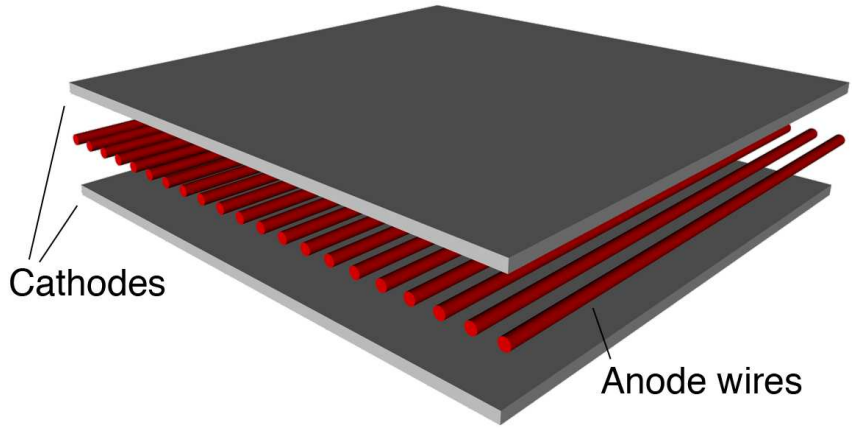

Figure 3.7: Geometry of a simple multiwire proportional chamber.

When a primary ion pair is produced, the electron drifts in the direction of the highest field gradient. Thereby it moves towards the nearest wire and undergoes the multiplication process discussed in Section 3.1.2. However, the region where the amplification process takes place is rather small compared to the MWPC size. Figure 3.9 shows the electric field depending on the distance from the wire center for a wire with a diameter of 20 μm [Cha70b]. To calculate the avalanche region, Equation 3.1, which describes the electric field inside a proportional counter tube, is used for a multiwire proportional chamber in a first approximation. With the parameters $b = 3$ mm, $a = 20$ μm and an electric field of $E = 10^6 \frac{\mathrm{V}}{\mathrm{m}}$, where the gas amplification begins [Kno79], the region of amplification can be calculated for different operating voltages:

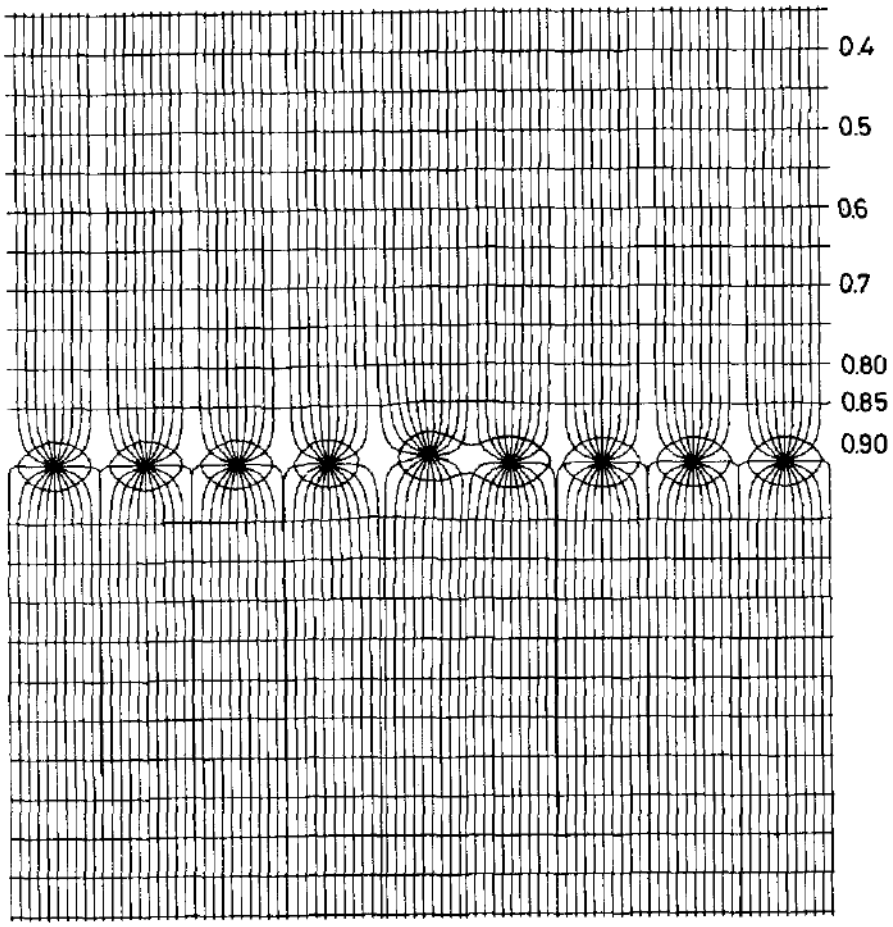

Figure 3.8: Electric field of a multiwire proportional chamber. The effect of a displaced wire can be seen on wire 5 and 6 (from left to right). The scale indicates the electric field strength, where 1 is the electric potential at the surface of the wires, and 0 is the potential at the surface of the cathode [Cha70b].

$$
\begin{aligned}
r &= \frac{V}{E \cdot \ln\left(\frac{b}{a}\right)} \qquad (3.8)\\
&= \begin{cases} 200\mu\text{m} & V = 1.0 \text{ kV} \\ 300\mu\text{m} \quad \text{for} & V = 1.5 \text{ kV} \\ 400\mu\text{m} & V = 2.4 \text{ kV} \end{cases}
\end{aligned}
$$

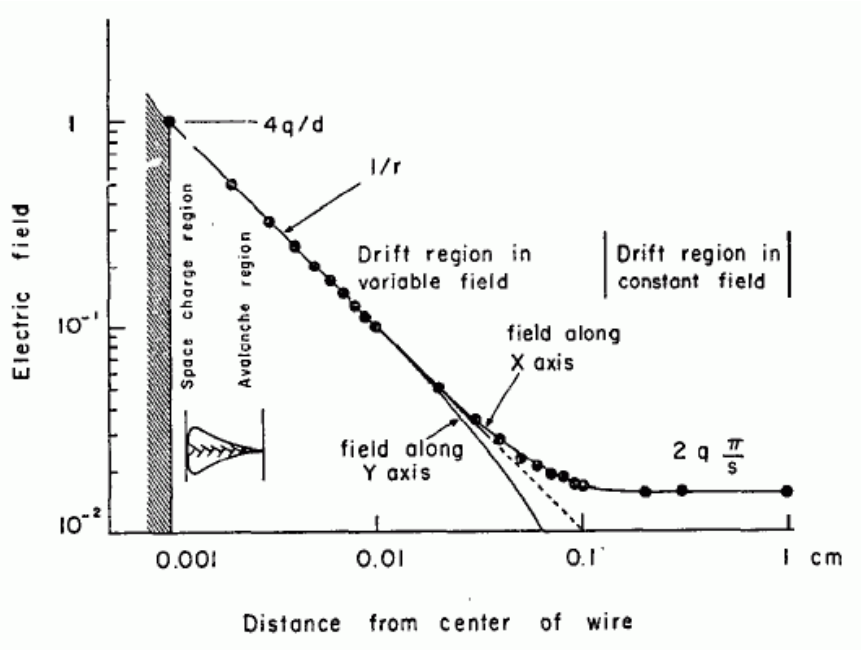

Figure 3.9: Different regions of the charge propagation [Cha70a].

Using the construction shown in Figure 3.7, the signal is obtained from the anode. Each single wire has to be read out with two channels to get the correct location of interaction: The x-coordinate is represented by the wire on which the signal occurred. To reconstruct the y-coordinate, the charge division technique can be used (see Section 3.2.2).

To improve the spatial resolution, modern multiwire proportional chambers usually do not have a single plane cathode on each side of the anode wires. Instead several cathode strips with one plane of strips orientated perpendicular to the wires and the other orientated parallel to the wires are used. This construction can be reviewed in Figure 3.10.

By using this type of chamber, one can use the center of gravity technique to calculate the exact location of interaction. (see Section 3.2.2). The advantage of this method compared to the charge division method is that the spatial resolution is better than the size of the gap between the readout points. Therefore fewer cathode strips and fewer readout channels are required, still providing a submilimeter spatial resolution.

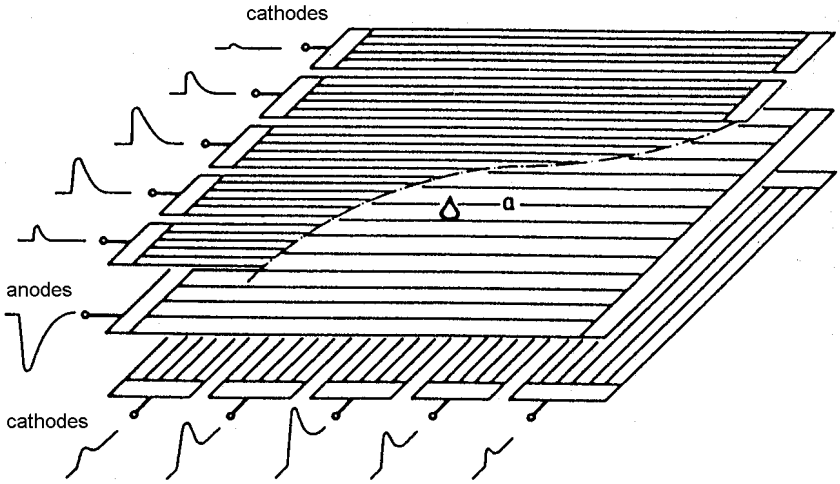

Figure 3.10: Divided cathodes allow a better readout process [Bre76].

3.2.2 Readout Methods

Charge Division Method

For the charge division readout method, two readout channels are necessary for each anode wire. Every single wire is read out on each side, so that the charge that is collected on each side can be compared.
The fraction of the charge Q_A and the total charge $Q_A + Q_B$ is proportional to the distance between the point of readout A and the place of interaction y. The proportionality coefficient is the length L of the wire:

$$y = L\frac{Q_A}{Q_A + Q_B} \tag{3.9}$$

Where Q_A and Q_B are the charges that are collected on the readout points A and B. According to [Cha79a], accuracies of up to 0.4% of the wire length can be achieved. The principle of the charge division method is shown in Figure 3.11. The main drawback of this readout method is the inexpedient large amount of readout channels that are needed to readout every wire on two sides.

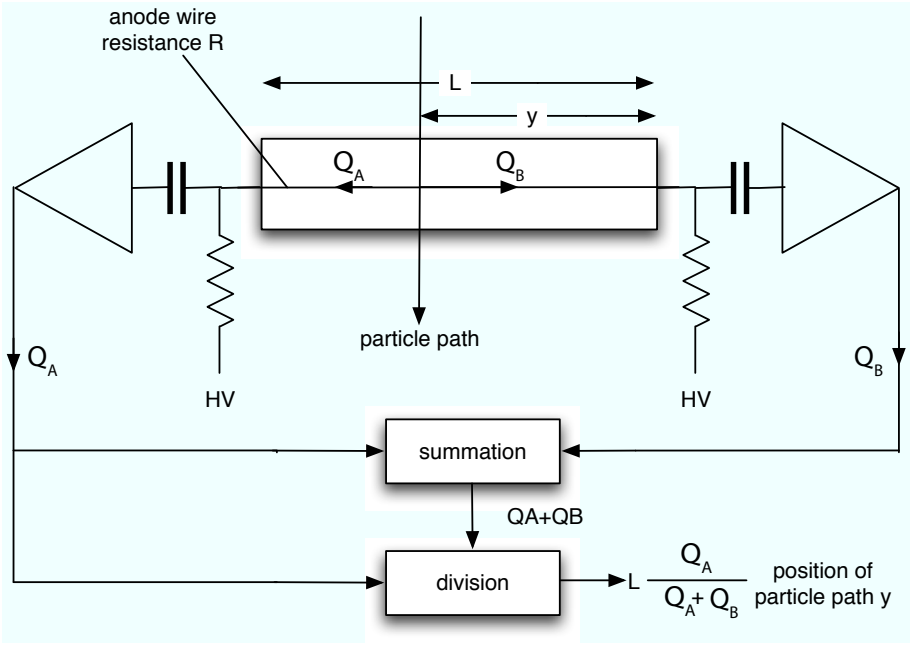

Figure 3.11: Principle of the charge division readout method as shown in [Fis77].

Delay Line Method

The delay line procedure is one of the earliest readout techniques and can be realized even with very elementary analog electronics. For this method both, the anode and the cathodes have to be read out. The two cathode planes consist of wires, one plane lies parallel to the anode wires the other lies perpendicular. The wires of each one cathode plane are coupled to a so-called delay line. The delay line delays the signals of the cathode wire by a time that is proportional to the length of the delay line between the wire position and the readout point of the delay line. The signal of the coupled anode wires serves as a start signal for a TDC[1] and the cathode signals serve as the stop signal. Since the time between the start signal and the stop signal is proportional to the length of the delay line, the position of the wire on which the avalanche occurred can be calculated to obtain the two coordinates of interaction with an accuracy of 0.15 mm [Gro70].

[1]TDC: Time to digital converter. This device converts the time between a start signal and a stop signal into a digital number that is proportional to the time between the two signals. The timing resolution of modern TDC devices is on the order of 1 ns down to a few ps.

Center of Gravity Method

For the center of gravity readout method the induced signals on the cathode strips shown in Figure 3.10 are read out instead of the anode wires. As shown in this figure, these induced signals are largest on the strip nearest to the anode wire on which the avalanche occurred and diminishes with the distance. By calculating the center of gravity for the signals, the point of interaction can be estimated, as

$$y = \frac{\sum(Q_i - b)y_i}{\sum(Q_i - b)}. \tag{3.10}$$

In this formula, Q_i is the charge measured on the i*th* strip, y_i is the coordinate of the i*th* strip and b is a small bias which, according to [Cha79b], has to be subtracted to correct the dispersive effects of noise. According to [Cha84], position resolutions of up to 35 μm have been reached for soft x-rays with this method. However, due to the higher kinetic energies, the position resolution decreases with higher particle energies, so that resolutions of about 100 μm are more typical for common applications [Cha84].

Pad Response Function

The use of the pad response function (PRF) for the position reconstruction is an improvement of the center of gravity method. It is assumed that the charge which is induced on the pads during a Townsend avalanche approximately corresponds to a Gaussian distribution within a few per cent of its maximum value [Blu94] :

$$PRF(x) = A \cdot e^{-\frac{x^2}{2\sigma^2}} = \frac{Q_i}{Q_{\text{total}}} \tag{3.11}$$

Here, x is the distance between the Townsend avalanche and the center of the pad with the most induced charge carriers in pad units, Q_i is the charge that is induced on the center pad i and Q_{total} is the total charge induced on all pads. As a good approximation, Q_{total} is replaced by the sum of charges induced on the three center pads $Q_{i-1} + Q_i + Q_{i+1}$. Solving this equation for the distance x one gets:

$$x = \frac{1}{w_1 + w_2}\left[w_1\left(-\frac{W}{2} + \frac{\sigma^2}{W} \cdot \ln\frac{Q_i}{Q_{i-1}}\right) + w_2\left(\frac{W}{2} + \frac{\sigma^2}{W} \cdot \ln\frac{Q_{i+1}}{Q_i}\right)\right] \tag{3.12}$$

With $w_1 = Q_{i-1}^2$, $w_2 = Q_{i+1}^2$, W = pad width and σ = sigma of Gaussian fit to PRF. To determine the displacement independently of the a priori knowledge of the Gaussian σ, it can be calculated by the approximation([KB06] and [Bus02]):

$$x = \frac{W}{2} \frac{ln(Q_{i+1}/Q_{i-1})}{ln(Q_i^2/Q_{i+1}Q_{i-1})} \tag{3.13}$$

With Equation 3.11 and Equation 3.13 the pad response can be determined for several test events. After a Gaussian fit to these data, sigma can be determined to calculate the exact displacement of every event with Equation 3.12. This readout method is favored for the multiwire proportional chambers in modern particle physics experiments.

4. Motivation for an MWPC Small Animal PET

4.1 Reasons for the Construction of a Small Animal PET Detector

The techniques of modern medical research demand non invasive in vivo images of increasing quality. Therefore the imaging technologies have to be improved constantly. Especially the research on new disease-specific radiotracer molecules requires a very good spatial resolution to detect even the smallest tracer concentrations within the organisms of small animals. The positron emission tomography is the only technology that provides functional images of an organisms metabolism by using molecular biomarkers in a satisfying image quality. Therefore the market for high resolution small animal PET devices will even increase in the future.
The performance of PET scanners can be characterized by two values: The volumetric spatial resolution and the sensitivity. The volumetric spatial resolution, measured in mm^3, describes the capacity to separate two radiotracer distributions within a certain volume in the three dimensional image reconstruction. The effects of a very high volumetric spatial resolution are images with a small pixel respectively voxel size and therefore a very good image quality that allows a more precise diagnosis. Especially for small animal PET devices, good volumetric spatial resolution is very important for a satisfying performance. Since neurology, cardiology and oncology are the three main research disciplines that PET is used for, the imaging of small structures, like the brain or the heart of a mouse, plays an important role for the positron emission tomography. According to [Sty06] and [Eng06], the total length of a mouse's heart is 6-8 mm, while its diameter is 3-5 mm, depending on age, gender, weight, genotype and strain. The length of the brain is approximately 7 mm [Mye02]. Since the spatial resolution achieved by common PET scanners used for human patients lies between 5 and 7 mm [Lod05], these scanners do not provide a sufficient image quality that is required for modern medical research. The consequence is the

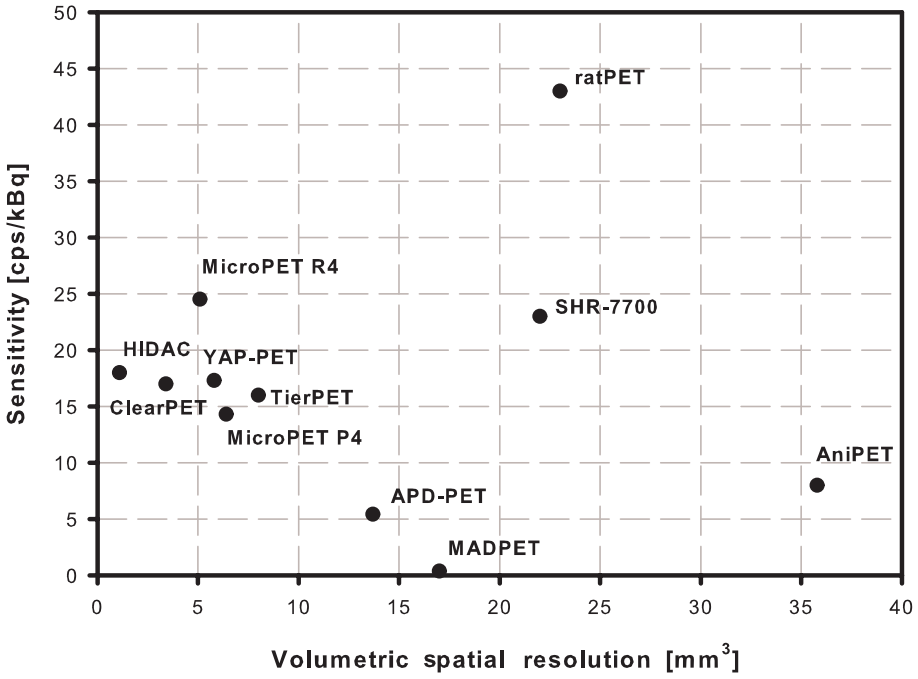

Figure 4.1: Sensitivity and volumetric spatial resolution for several small animal PET scanners. Data from [Sch03a].

demand for PET scanners with a small field of view[1], but a high spatial resolution, constructed especially for the examination of small animals.
The sensitivity of a PET scanner, measured in $\frac{\text{counts}}{\text{second}\cdot\text{kBq}}$, describes the fraction of the radioactive decays that occur in the examined tissue that is detected by the scanner. A good sensitivity allows the reduction of the amount of applied radiotracer and therefore the reduction of the radiation exposure for the patient. Since the reduction of the radiation exposure in small animal PET imaging is not as important as it is in human imaging processing, a higher sensitivity allows a shorter acquisition time with a given amount of applied radiotracer and thus a higher scan rate with more mice examined in a certain period of time. In Figure 4.1, the sensitivity is plotted against the volumetric spatial resolution for several obtainable small animal PET scanners. In this diagram, an optimal PET scanner would be found in the upper left corner with a very high sensitivity and a good spatial resolution.

[1]field of view: The field of view (FOV) is the region that is *seen* by a scanner. In radiology, the FOV is an important parameter for the quality assurance of a diagnostic device and the evaluation and its images.

Here, the HIDAC PET scanner is the only device working with multiwire proportional chambers. It can be seen that this detector has a sensitivity that is comparable to other devices and a very good spatial resolution which nowadays cannot yet be reached by the other competitors. The detectors which are used in all other scanners are scintillator crystals, read out by photo multiplier tubes or avalanche photo diodes (APD) respectively. This plot elucidates that PET systems working with MWPCs are able to achieve the same or even better performance parameters than crystal based PET scanners. To understand the motivation for the construction of an MWPC based PET device the advantages of wire chambers and crystals shall be explained more precisely.

4.2 Motivation for the Development of an MWPC-based PET Detector

4.2.1 Advantages of Scintillation Crystals

- **Energy resolution**
  The energy resolution of a particle detector characterizes its ability to distinguish between particles of different energies. The good energy resolution of scintillation crystals allows to reduce background counts in the image and thus to achieve a good image contrast.
  A PET scanner acquires three different types of coincidences: true coincidences, scatter coincidences and random coincidences. True coincidences are emissions from single annihilation points, which reach the detector without undergoing any kind of significant interaction with matter in the field of view. Scatter coincidences are emissions from the same annihilation that reach the detectors with at least one photon being Compton scattered. Random events are two photons from two different positron annihilation events detected simultaneously. Since the detection of scattered and random events leads to the calculation of wrong lines of response (LOR), the image contrast is reduced while the noise is increased with a growing number of scatter and random events.
  A good energy resolution allows the application of an energy gate to reject the detection of unwanted events. For example NaI scintillation crystals allow energy gates of up to 450 keV due to its good energy resolution of 6.6% [Bai03]. By this, all photons that reach the detector with an energy of less than 450 keV are ignored and thereby the image contrast can be improved compared to the reconstruction of one LOR for every coincidence detected. To measure the total energy of an incident particle, it has to be stopped and all its energy has to be deposited inside the detector. Due to the structure of multiwire proportional chambers and the very low cross section for 511 keV $\gamma-$particles to interact with a molecule of the filling gas, the stopping power of these detectors is too low to provide an adequate energy resolution with multiwire proportional chambers.

- **Timing resolution**
  By providing a good timing resolution too, scintillation crystals allow to improve the image quality even further. Due to the very fast detection system, the coincident gate can be set to a very short period of time. The random event count rate is proportional to τA^2, where τ is the coincidence window width and A is the activity present inside the scanner [Bai03]. Therefore the reduction of the window width leads to a linear reduction of the random count rate and thereby to a reduction of the noise and an improvement of the image contrast.
  According to [Mos06], the coincidence timing resolution of the CPS Accel, a commercial PET camera working with LSO crystals, is about 3 ns. With a single LSO crystal test system timing resolutions of 221 ps have been achieved, whereas the timing resolution of a multiwire proportional chamber is about $25 - 30$ ns [Kno79].

- **Absorption efficiency**
  Due to the high atomic numbers of the crystals the absorption efficiency of the crystal detectors is very high. Common crystal materials have an effective Z of 34.2 for yttrium oxyorthosilicate (YSO) and up to 72.2 for bismuth germanate (BGO). As can be seen in Equation 2.17 and Equation 2.31, the probabilities for the photoelectric effect or the Compton effect highly depend on the atomic number and therefore the high-Z crystals can provide a much better stopping efficiency than the gas filled multiwire proportional chamber.

4.2.2 Advantages of Multiwire Proportional Chambers

- **Costs**
  Compared to modern scintillation crystals, the construction of multiwire proportional chambers is a very cheap procedure. Especially the new and modern crystal materials are very expensive to produce. Up to one third of the costs of a modern PET machine is the cost of the crystal material and another third is the cost of the photo detectors which are required for the signal readout of the crystals [Zec06]. Both would not be necessary for a PET that works with multiwire proportional chambers. The detector itself and the readout electronics, which could get by with just an amplifying system, ADCs to digitize the data and a controlling computer, could be built much more economically.

- **Spatial resolution**
  Since every single wire of the multiwire proportional chamber can be regarded as a single detector, the spatial resolution of these detectors is very high. In comparison to scintillation crystals, the construction of high resolution MWPCs is a very simple procedure since the detectors only consist of a grid of thin wires and the signals can be obtained directly from the cathodes. Using the crystal technology, very small and filigree crystals have to be produced and read out via small photo multipliers to achieve good spatial resolution.

- **Geometric acceptance**
  As the experience gained with huge particle detectors built for accelerator experiments has shown, it is not difficult to produce wire chambers of huge size. While the crystals are very expensive and therefore usually only one flat ring of detectors is build around the field of view and the patient has to be scanned slice by slice, the wire chamber detectors could be built all around the field of view very easily. This high geometric acceptance leads to a good total efficiency so that the activity applied to the patient could be reduced.

4.2.3 Conclusions

Although the technology of scintillating crystals has some advantages compared to the technology of multiwire proportional chambers, the enormous costs of these detectors demand research for alternative ways of radiation detection and image reconstruction. Using MWPCs as detectors for the 511 keV photons gives the opportunity of a very good spatial resolution at the expense of difficulties that result from the missing energy resolution and rather poor timing resolution. The main reason for the use of wire chambers however, is the economical efficiency during the production process of even very large chambers. The successful employment of the QUAD HIDAC small animal PET device demonstrates the satisfying performance parameters and the usability of this technology. Since this PET system makes use of photon-electron converters of a very complex construction, the idea came up to simplify this converter and develop a low cost and easy to produce high-resolution small animal PET device.

5. Determination of the Optimal Converter Thickness

The problem with detecting 511 keV γ-rays in multiwire proportional chambers is the very low cross section for photon interactions in the low-Z atoms of the fill gas (e.g. argon or xenon) and the low density of these elements. Most of the photons pass the chamber without any kind of reaction and thereby the efficiency of such a detector is unsatisfactory. One option to handle this challenge is to convert the incoming γ-particles into electrons using the photoelectric effect or Compton effect. Parameters of this converter ought to be a high nuclear number and a high density. An economic material with these properties is lead. Therefore thin foils of lead could be used to convert the incoming photons into charged particles that could easily be detected in the MWPCs.

As seen in Equation 2.17 and Equation 2.31, the probability for the photoelectric effect approximately goes with Z^5 and the probability for the Compton effect goes with Z. Due to the higher atomic number Z and the higher density of lead, the total attenuation coefficient for 511 keV γ-radiation in lead is more than 10.000 times higher than the total mass attenuation coefficient in argon [Ber05b].

When a foil of lead is placed at the entrance window of a multiwire proportional chamber, two effects influence the number of electrons that leave the lead and enter the fill gas. On one hand more photoelectrons and Compton electrons are produced with an increasing foil thickness. Since there are more electrons to interact with, there are more electrons that are liberated by the photoelectric effect or Compton effect. On the other hand the mean range of electrons with an energy of 423 keV, which would be the maximum energy for electrons liberated by the photoelectric effect in the inner electron shells, is only 40 μm [Laz00]. Thus, the electrons that are produced in the lead are slowed down and stopped already in the converter and do not leave the foil, if the foil is too thick. Therefore the converter would only absorb the incoming radiation without providing a better conversion efficiency, since only the electrons liberated in the last few μm could leave the foil to enter the detector. Due to these two competing effects an optimal layer thickness can be calculated and measured for the converter.

5.1 Theoretical Determination of the Optimal Converter Thickness

To get an idea of the optimal converter thickness, a rough estimation can be made. Although the assumptions that are made contain inaccuracies, the calculation can give an idea of the scale of the optimal converter thickness.
For the photon-energies of 511 keV the absorption is described by an exponential decrease of intensity:

$$I(x) = I_0 \cdot e^{-\lambda x} \tag{5.1}$$

Because the pair production as a process of interaction of radiation and matter only takes place at energies above 1.022 MeV, which is twice the rest energy of the electron, the absorption coefficient λ is a composite of the absorption coefficients for the photoelectric effect λ_{photo} and for the Compton effect λ_{Compton}. According to Berger et al., the mass absorption coefficient of lead for photons of 511 keV consists of $\lambda_{\text{photo}} = 8.26 \times 10^{-2}\ \frac{\text{cm}^2}{\text{g}}$ and $\lambda_{\text{Compton}} = 6.73 \times 10^{-2}\ \frac{\text{cm}^2}{g}$ [Ber05b]. Thus the total mass absorption coefficient of lead for 511 keV photons is $\lambda_{\text{total}} = 0.1499\ \frac{\text{cm}^2}{\text{g}}$.
To calculate the number of electrons liberated from the converter foil, the exit probability of the electrons has to be determined. With the mass absorption coefficients specified above, one gets a photoelectron to Compton electron ratio of:

$$\frac{n_{\text{photo}}}{n_{\text{Compton}}} = \frac{0.551}{0.449} = 1.23 \tag{5.2}$$

A formula for the transmission probability T of electrons and positrons propagating through absorber foils is given in [Rao66]:

$$T = \frac{1 + e^{-\mu x_0}}{1 + e^{\mu(x - x_0)}}. \tag{5.3}$$

With the parameters $\mu = \frac{n}{R_p}$ and $x_0 = n_0 \cdot R_p$. The constants n and n_0 are given to be $n = 9.2Z^{-0.2} + 16Z^{-2.2}$ and $n_0 = \frac{0.63Z}{A} + 0.27$. R_p, which is called practical range of the electrons and was validated for an energy range of (0.01 MeV $<$ E $<$ 3 MeV), has different, energy dependent, values for electrons and positrons [Rao66]:

$$
\begin{aligned}
R_p^-(\mathrm{mg/cm^2}) &= \left(\frac{166\times10^{-5}}{Z^{0.33}}\right)\cdot E^{2.579-0.219\log_{10}E} \\
R_p^+(\mathrm{mg/cm^2}) &= \left(\frac{955\times10^{-5}}{Z^{0.25}}\right)\cdot E^{2.600-0.200\log_{10}E}.
\end{aligned} \tag{5.4}
$$

To simplify the calculation, the energies of the photoelectrons and Compton electrons are assumed to be the mean energies of these electrons. Due to the K-shell energy of 88 keV, the photoelectrons that are emitted from this shell have a discrete energy of 423 keV. Since nearly all photoelectrons originate for the K-shell for photon energies above the K-shell energy, the energy of the photoelectrons is assumed to be 423 keV.
The average Compton electron energy can be calculated with Equation 5.5 [Chi55]:

$$E_{av} = h\nu(\frac{{}_e\sigma_a}{{}_e\sigma}). \tag{5.5}$$

In this formula, Childers defines ${}_e\sigma$ as the total Klein-Nishina cross section shown in Equation 2.30, and ${}_e\sigma_a$ is the cross section for the energy absorbed by the electron. For the quantitative values ${}_e\sigma_a$ and ${}_e\sigma$, [Dav52] gives ${}_e\sigma_a = 0.987$ and ${}_e\sigma = 2.866$ for electron energies of 511 keV. With these numbers, one obtains an average Compton electron energy of $E_{\mathrm{av}} = 175.98$ keV.
Therefore the transmission probability for an electron liberated by the photoelectric or the Compton effect (Equation 5.6) can be written as:

$$T = 0.551\cdot\left(\frac{1+e^{(-\mu x_0)}}{1+e^{\mu(x-x_0)}}\right)_{E=423\ \mathrm{keV}} + 0.449\cdot\left(\frac{1+e^{(-\mu x_0)}}{1+e^{\mu(x-x_0)}}\right)_{E=175.98\ \mathrm{keV}}. \tag{5.6}$$

Here, the first term represents the photoelectrons; Compton electrons are represented by the second term. Since the emission of photoelectrons and Compton electrons is subject to an angular distribution, the thickness which the electrons have to propagate through before their liberation has to be scaled with a factor that depends on the mean cosine of the angle. With Equation 2.21 and Equation 2.33, the emission angles for the photoelectrons and Compton electrons liberated by 511 keV γ-radiation can be calculated. The mean angles are: $\theta_{\mathrm{p}} = 28.2°$ and $\theta_{\mathrm{c}} = 32.4°$. The mean cosine of the photoelectron emission is $\overline{\cos\vartheta_{\mathrm{p}}} = 0.85$, while the mean

cosine of the Compton electron emission is $\overline{\cos\vartheta_c} = 0.82$. For the case of inclined incidence at angles $\theta < \frac{\pi}{2}$, Equation 5.6 has to be extended by

$$x \rightarrow \left(x' = \frac{x}{\cos\theta} \right). \tag{5.7}$$

With this extension, Equation 5.6 looks like:

$$\begin{aligned} T &= 0.551 \cdot \left(\frac{1 + e^{(-\mu x_0)}}{1 + e^{\mu(x \cdot \overline{\cos^{-1}\theta_p} - x_{0)}}} \right)_{E=423 \text{ keV}} \\ &+ 0.449 \cdot \left(\frac{1 + e^{(-\mu x_0)}}{1 + e^{\mu(x \cdot \overline{\cos^{-1}\theta_c} - x_{0)}}} \right)_{E=175.98 \text{ keV}} . \end{aligned} \tag{5.8}$$

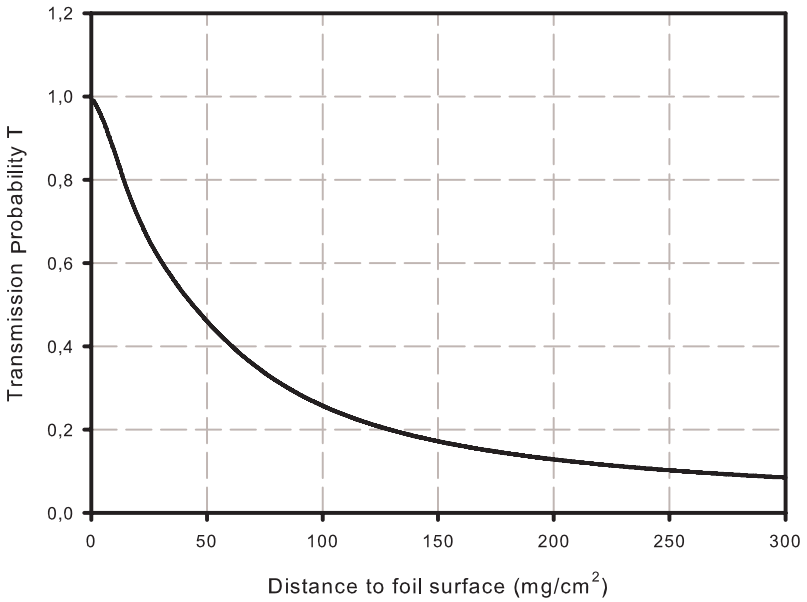

Figure 5.1: Escape probability of the photo and Compton electrons, as a function of the distance to the surface of the lead foil.

The transmission probability is illustrated in Figure 5.1. It can be seen that the probability for an electron to escape the converter foil diminishes for foil thicknesses above 100 $\frac{\text{mg}}{\text{cm}^2}$.

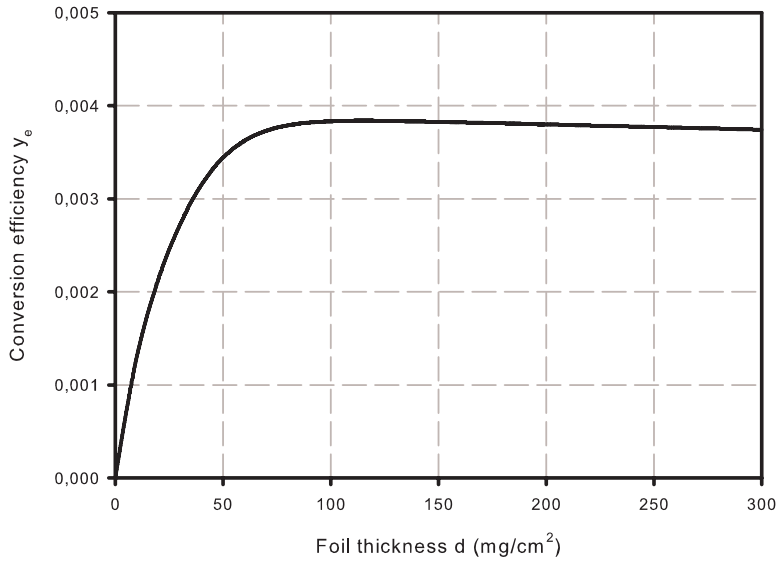

Figure 5.2: Efficiency of the converter depending on the lead thickness.

With the calculated intensity (Equation 5.1) and escape probability for the electrons (Equation 5.8), the standardized electron yield can be calculated as a product of intensity and escape probability. Therefore it can be assumed that the electron production rate commensurates with the intensity. When integrating over the point of electron production, one obtains:

$$y_e(d) = \frac{\lambda}{\dot{i}_0} \int_0^d I(d')T(d-d')dd' \tag{5.9}$$

This efficiency is shown in Figure 5.2. From a thickness of 80 $\frac{\text{mg}}{\text{cm}^2} \mathrel{\hat{=}} 70$ μm on, the calculated function forms a plateau. Although the efficiency has its theoretical maximum at a thickness of $d_{\text{opt}} = 114.915 \frac{\text{mg}}{\text{cm}^2} \mathrel{\hat{=}} 101$ μm, a converter of 70 μm has an efficiency of 98% of its maximum value.

5.2 Experimental Determination of the Optimal Converter Thickness

The theoretical calculations of the optimal layer thickness shall be validated experimentally. The principle of finding the optimal thickness must be to detect the electrons that are liberated by a thin foil of lead when it is irradiated with photons of 511 keV. When different foils are inserted in the setup, the electron emission as a function of the foil thickness can be obtained. The entire setup can be seen in Figure A.1, Appendix A.

5.2.1 Experimental Setup

The Experimental Setup

The experimental setup is rather simple. The ^{137}Cs source, which is fixed to an optical bench, provides the necessary γ-radiation. The photons emitted by ^{137}Cs do not have an energy of exact 511 keV, but 662 MeV. Due to the lack of a γ source with an energy of exactly 511 keV, a ^{137}Cs source is used for the measurement. Therefore the optimal converter thickness that can be determined with this measurement is expected to be higher than the optimal converter thickness for γ-particles of 511 keV. The β-particles, which are liberated by ^{137}Cs additionally to the γ-radiation, are absorbed by a 6 mm thick layer of perspex. The 662 MeV γ-radiation passes through the perspex with minor interaction. After propagating through the perspex, the γ-particles impinge on a foil of lead. As described in Section 2.4.1 and Section 2.4.2, the photons interact with the lead electrons via the photoelectric or the Compton effect. Therefore electrons are liberated from the lead and can be detected by a surface barrier detector that is arranged directly behind the lead foil. The count rate is expected to increase in an energy range below the 662 MeV of the incident photons.
Since foils with different layer thicknesses liberate a different number of electrons, the spectra are expected to differ for energies below the original γ-particle energy when different foils are inserted into the installation. From the differing spectra an optimal thickness, for which the number of liberated electrons is at its maximum, can be calculated by integrating the whole count rate and subtracting the count rate of the measurement without a foil.

Surface Barrier Detectors

A surface barrier detector, which is shown in Figure 5.3, consists of a thin n-type silicon wafer in combination with certain metals, e.g. a very thin coating of gold or a coated layer of p-typed silicon. Caused by the higher Fermi level in the n-type silicon layer, a weak electromagnetic field is formed. Since the Fermi level has to be equal in the barrier layer, the valence band and the conduction band are deformed to a common level. The outcome of this band deformation is a potential difference that causes a current of charge carriers, which ends in a depletion zone, where the density of free electrons is very low. By applying a negative voltage to the p-typed layer, the depletion zone which is also called junction, can even be enlarged.
When a charged particle passes the junction, it creates electron ion pairs by transferring energy to bound electrons. The electrons are collected by the applied voltage and a signal that is proportional to the primary deposited energy can be obtained.

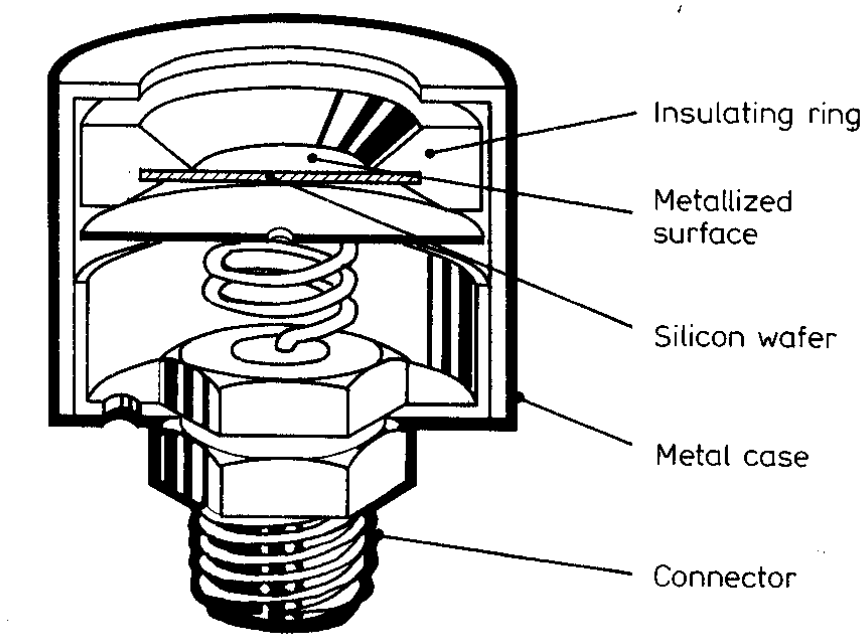

Figure 5.3: Cross section of a typical surface barrier detector [Leo87].

The Electronic Setup

An illustration of the electronic setup can be reviewed in Figure A.1, Appendix A. The signals of the surface barrier detector are amplified in the Canberra 970D Preamp and the Ortec 452 Spectroscopy Amplifier and divided into two independent signals by the PS 740 Fan in/Fan out NIM module. One of the two signals is discriminated by the PS 706 16 Channel Discriminator to get a well shaped trigger signal for the PS 704 Quad Gate Generator. The generated gate signal, as well as the second detector signal which is delayed by 280 ns to match the reaction time of the discriminator and the gate generator, are fed into the LeCroy Peak Sensing ADC 2259B. Here, the detector signal is converted into a digital number which is proportional to the pulse hight of the original signal. The ADC memory then is read out by a Camac PC interface. The obtained data is written into a histogram that visualizes the energy distribution of the events recorded by the surface barrier detector.

5.2.2 Energy Calibration

To assign the channel numbers of the ADC to the particle energies, a calibration has to be performed. Therefore the spectrum of a mixed nuclide source of known energies is taken. The mixed nuclide source contains the α-particle emitting isotopes ^{239}Pu, ^{241}Am and ^{244}Cm. The energies of the most intense α particles are 5.155 MeV, 5.486 MeV and 5.805 MeV. With the knowledge of the exact energies, the particle energy can be identified for every ADC channel. The obtained spectrum of the mixed nuclide source and the corresponding energy fit can be seen in Figure 5.4 and Figure 5.5. For the following diagrams the energy can be identified and therefore the energy is displayed instead of the ADC channel number.

5.2.3 The Measured Spectra

The measurement of the spectrum was performed without a lead foil and for several foil thicknesses between 30 μm and 110 μm. The spectra that were measured with the described setup are shown in Figure 5.6. A more detailed view of the energy range up to 500 keV, which is the interesting interval as the liberated electrons are of that kinetic energy, can be seen in Figure 5.7.

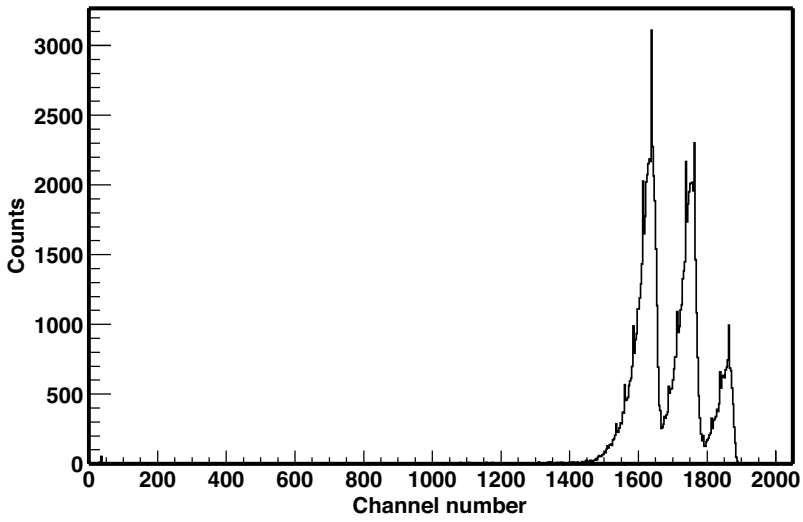

Figure 5.4: Spectrum of the mixed nuclide source, taken to calibrate the measuring station.

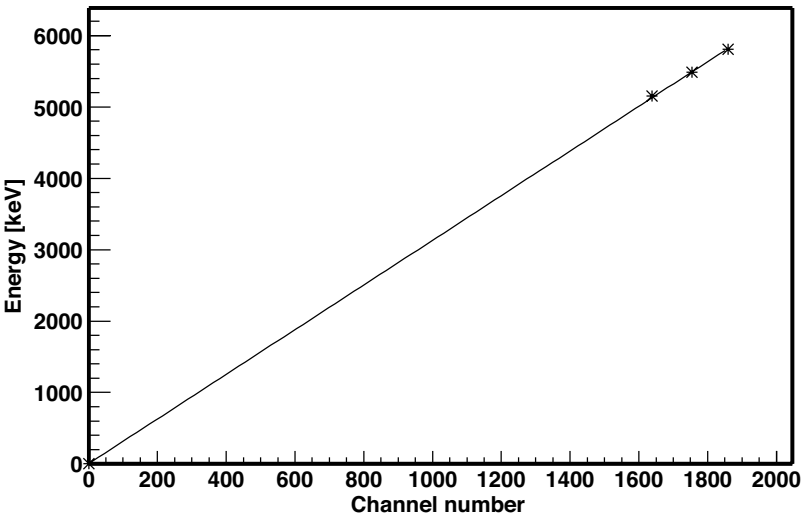

Figure 5.5: Calibration of the measuring station. The known energies of the mixed nuclide sources are assigned to the channel numbers of the ADC.

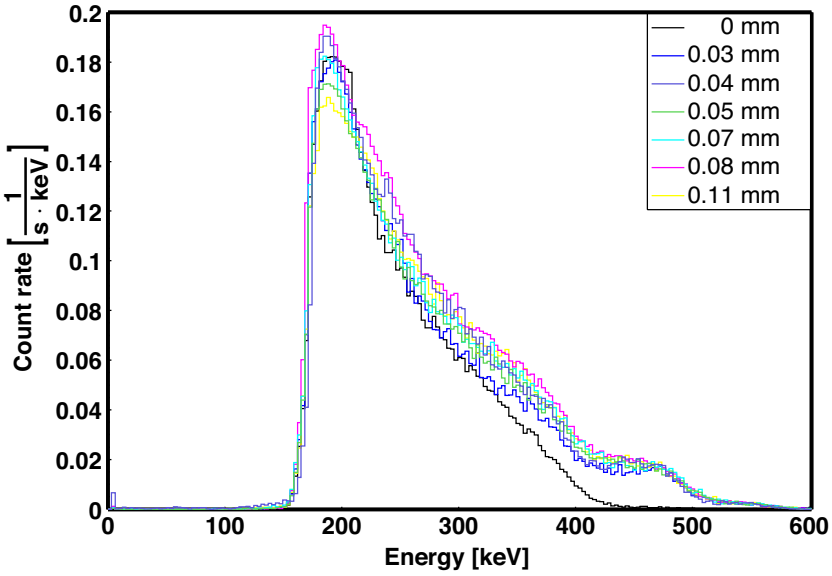

Figure 5.6: Spectra of the ^{137}Cs-Source radiating through different lead foils.

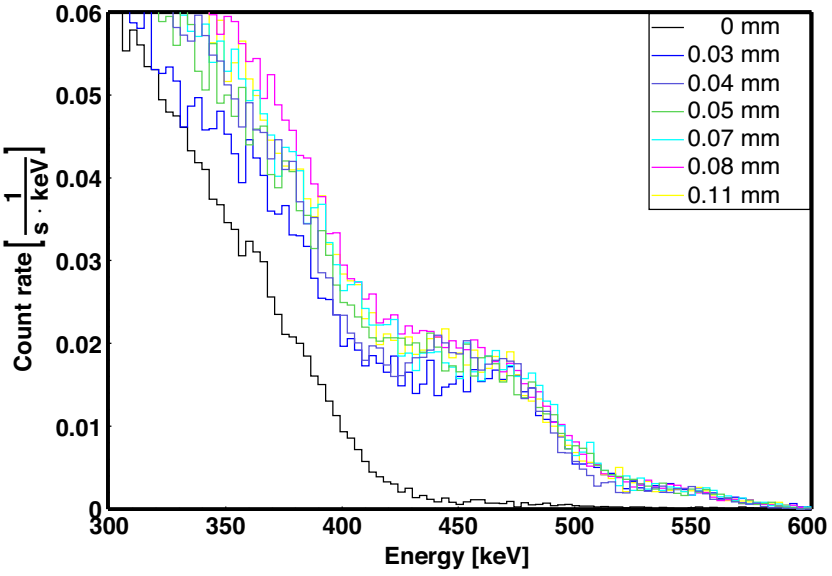

Figure 5.7: Energy band around 500 keV of the ^{137}Cs-Spectra.

Foil thickness	300-662 keV	350-662 keV	400-662 keV
0 μm	0	0	0
30 μm	0.752	0.678	0.529
40 μm	0.871	0.726	0.553
50 μm	1.011	0.835	0.571
70 μm	1.129	0.909	0.596
80 μm	1.167	0.899	0.577
110 μm	1.168	0.906	0.588

Table 5.1: Count rate growth $[s^{-1} \cdot keV^{-1}]$ for different foil thicknesses and energy bandwidths.

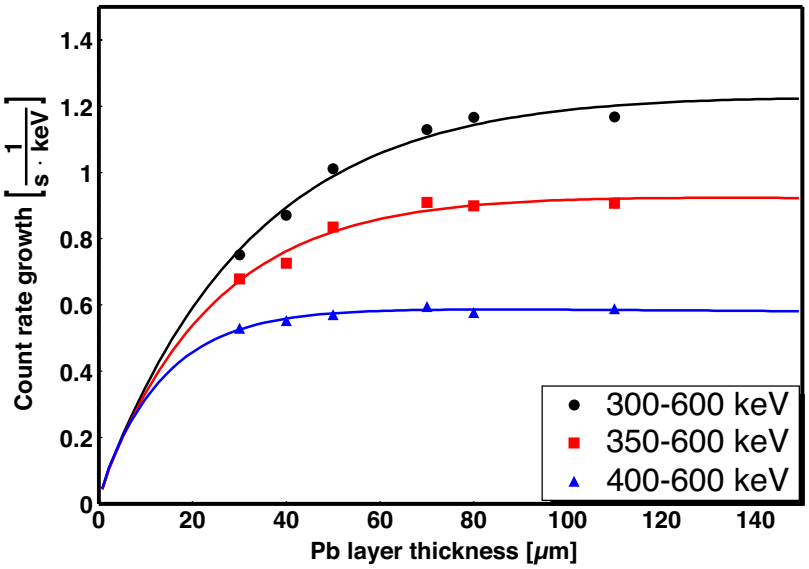

Figure 5.8: The electron liberation has its maximum at a foil thickness of around 70 μm to 80 μm.

For every spectrum the increase of count rate in a certain energy band compared to the 0 μm spectrum can be calculated by subtracting the histogram entries and integrating over the whole energy band. Table 5.1 presents the count rate growth for the energy bands of 300 to 662 keV, 350 to 662 keV and 400 to 662 keV.

When these data are plotted, one can see (Figure 5.8) that the electron liberation has its maximum at a foil thickness of around (70 - 80) μm. With higher foil thicknesses the beam intensity is weakened without more electrons being emitted from the foil.

5.3 Evaluation of Theory and Measurement

The two techniques to determine the optimal lead converter thickness give corresponding results: The theoretical estimation of the most efficient converter thickness led to an efficiency plateau from 70 μm on, while the measurement came to an optimal thickness of $(70 - 80)$ μm. Since the theoretical determination of the most efficient converter thickness is only an estimation that was intended to determine a rough idea, these results are satisfying. Although several assumptions have been made that may cause inaccuracies in the theoretical estimation as there are the energy of the Compton electrons that has been assumed to be the mean energy of the Compton electrons, the calculated and the measured data fit rather well.

Another technique to confirm the measured data is a Monte Carlo simulation that was performed [Got07] with the physical simulation environment GEANT4 [GEA07]. In this mathematical simulation, the behavior of electrons is simulated. A simulated lead foil is irradiated with 1.000.000 γ-particles for foil thicknesses

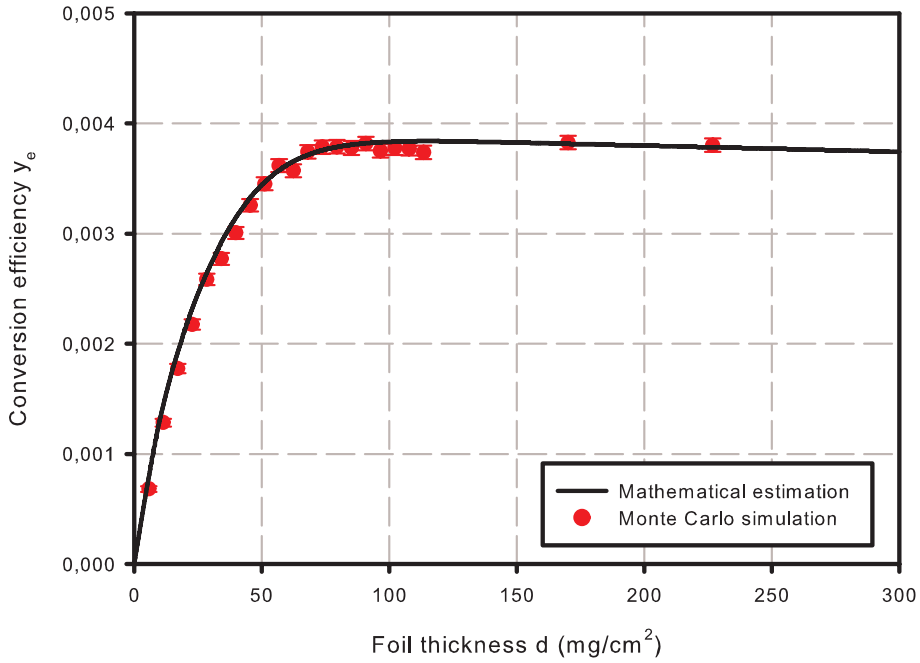

Figure 5.9: Efficiency of the photon-electron converter in dependence on the foil thickness. The line represents the mathematical estimation, the data points are derived [Got07] by the simulation environment GEANT4.

between 5 μm and 200 μm. The behavior of the incident photons and the liberated electrons is determined by the knowledge of the interaction probabilities. Since the interactions can only be described by the use of probabilities, the simulation only becomes statistically relevant for a large number of simulated electrons. Figure 5.9 shows the efficiency of a lead foil converter as estimated in Equation 5.9 and the results of the Monte Carlo simulation. The error bars of the simulated data contribute to the root-mean-square deviation $\frac{\sigma}{N} = \sqrt{\frac{\epsilon \cdot (1-\epsilon)}{N}}$ of the binominal distribution, where $\epsilon = \frac{N_e}{N}$. N_e is the calculated number of electrons that leave the foil and N is the number of simulated photons ($N = 1.000.000$). This simulation confirms the value of the mathematical estimation very well. As a consequence of these three results, a thickness of 70 μm is defined to be a promising converter thickness.

6. The MWPC Prototype

6.1 Construction of a Multiwire Proportional Chamber

To perform first test measurements and to prove that the principle of PET using multiwire proportional chambers works as expected, a first MWPC prototype was designed and constructed. Using the mechanical drawing (see Figure 6.1), the prototype was constructed in the mechanical workshop of the Institut fr Kernphysik in Mnster.

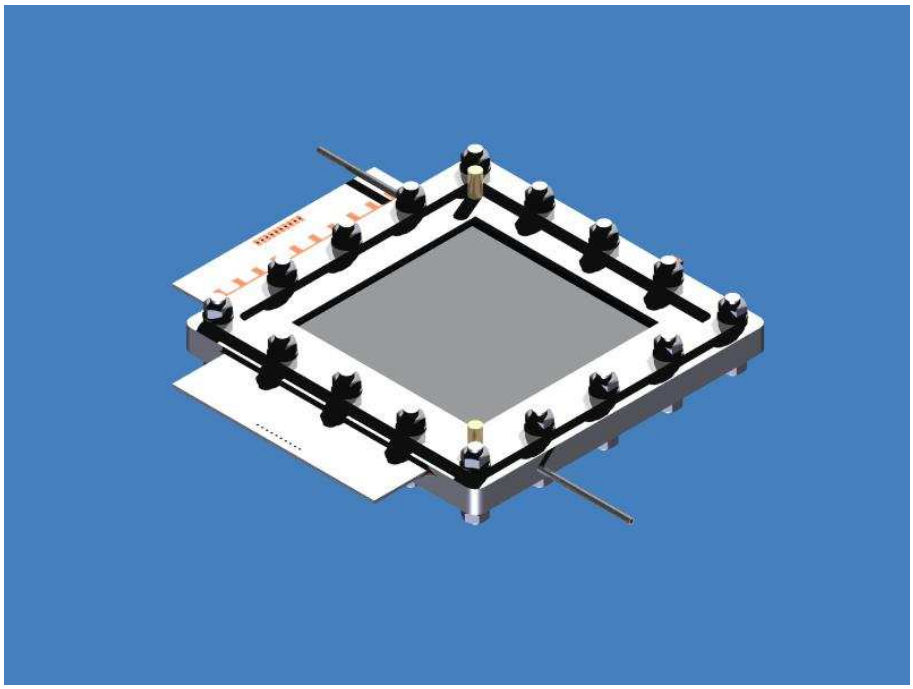

Figure 6.1: Rendered image of the mechanical drawing used to construct the MWPC prototype [Got06].

6.1.1 G-10 Frame

The prototype consists of two frames of G-10 synthetics, each with a thickness of 3 millimeters. The frames have a face of 16 cm × 16 cm and a cut-out of 10 cm × 10 cm in the middle of the layer. One of the frames has the wires applied to one surface, so that the two frames can be fixed together with the wires in between with 3 millimeters of G-10 synthetics on both sides. To avoid a gas exchange between the proportional chamber and the ambiance, thin strips of Teflon are placed between the two frames as a sealing.

6.1.2 Wire Winding

For an accurate operation of the detector, a sag-free mounting of the wires is of great importance. A sag of the wires would transform the electric field inside the chamber in an unpredictable way and the particle detection would not be isotropic. Therefore each wire has to be wound with a definite tension. The wires that are used for the MWPC are of the same type as the wires that are used for the ALICE TRD project. Therefore the wire tension that has been chosen for the TRD wires will be applied to these wires, too.
To provide an accurate and definite tension, the tungsten wires with a diameter of 20 μm have been applied to the frame at the Institut fr Kernphysik at the Johann-Wolfgang-Goethe University in Frankfurt, using the winding machine designed and constructed for the ALICE[1] Transition Radiation Detectors at CERN LHC[2]. This machine basically consists of an axis where a metal tension frame can be clamped and a device that provides the wire with a constant tension. The tension frame

[1]ALICE: A Large Ion Collider Experiment - The ALICE Collaboration is building a dedicated heavy-ion detector to exploit the unique physics potential of nucleus-nucleus interactions at LHC[2] energies. The aim is to study the physics of strongly interacting matter at extreme energy densities, where the formation of a new phase of matter, the quark-gluon plasma, is expected. The existence of such a phase and its properties are key issues in QCD for the understanding of confinement and of chiral-symmetry restoration. For this purpose, the intent is to carry out a comprehensive study of the hadrons, electrons, muons and photons produced in the collision of heavy nuclei. Alice will also study proton-proton collisions both as a comparison for lead-lead collisions in physics areas where Alice is competitive with other LHC experiments [Ali06].

[2]The Large Hadron Collider (LHC) is a particle accelerator which will probe deeper into matter than ever before. Due to switch on in 2007, it will ultimately collide beams of protons at an energy of 14 TeV . Beams of lead nuclei will be also accelerated, smashing together with a collision energy of 1150 TeV [LHC06].

circles around the axis, while the wire provider moves parallel to the axis of rotation so that the frame is covered with parallel strings. When the entire frame is covered, the wires are fixed to the surface of the frame. The frame is removed and the wires can be glued to the G-10 frame of the MWPC.

6.1.3 Cathode Pads

As cathodes 0.2 μm layers of copper have been vaporized to a 25 μm foil of polyamide. Unfortunately this construction has shown to be inadequate since the signals that have been obtained from the MWPC seemed to be unpredictable and did not resemble the pulses one would expect from a working multiwire proportional chamber. One possible explanation for this undesired behavior is that microscopic clusters of copper are liberated from the vaporized cathodes and produce random

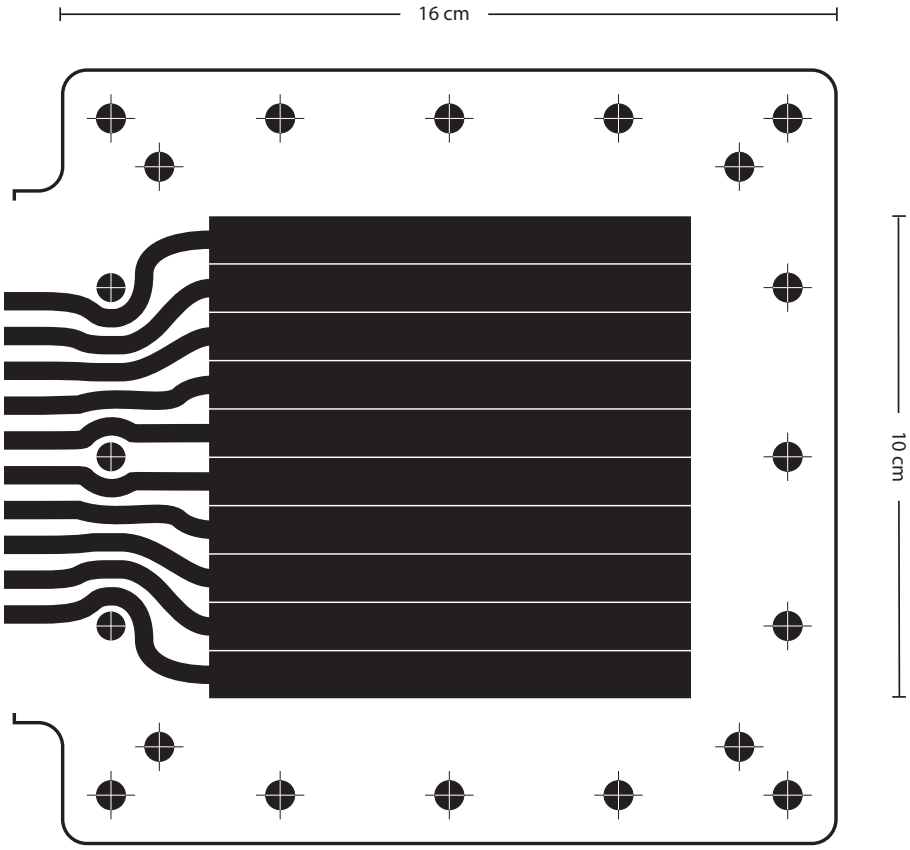

Figure 6.2: Pattern of the circuit board [Hei06].

errors by moving through the detector, performing a charge transport. Since the measurement with this chamber architecture was unsuccessful, a second pair of pad planes was constructed using circuit boards with copper printed onto. The pattern that was used to etch the pads on the circuit boards is shown in Figure 6.2. Since this type of cathode pads would not allow to use a converter since the conversion electrons would be stopped inside the cathode pads and would not enter the detector, a third generation of pad plane was produced. These planes use the pads itself as converters. The converter pads are discussed in Section 6.3. The planes are orientated perpendicular to each other, one pad plane on each side of the chamber. Using this construction, the pads can be used to read out both coordinates of an interaction.

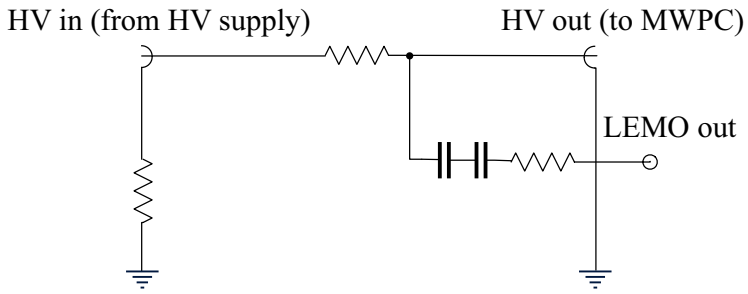

Figure 6.3: Circuit diagram of the readout electronics. The anode wires are read out via two capacitors to readout the pure signals without the applied high voltage.

To obtain the opportunity to read out both, the cathode strips and the anode wires, the high voltage can be read out via two capacitors, so that the voltage fluctuations caused by Townsend avalanches at the wires can be obtained without reading out the high voltage itself. With this construction, the readout electronics are protected from high voltage pulses that might damage or destroy them. The readout hardware was taken from the work of Klaus Reygers [Rey95]. A circuit diagram of the electronics is illustrated in Figure 6.3.

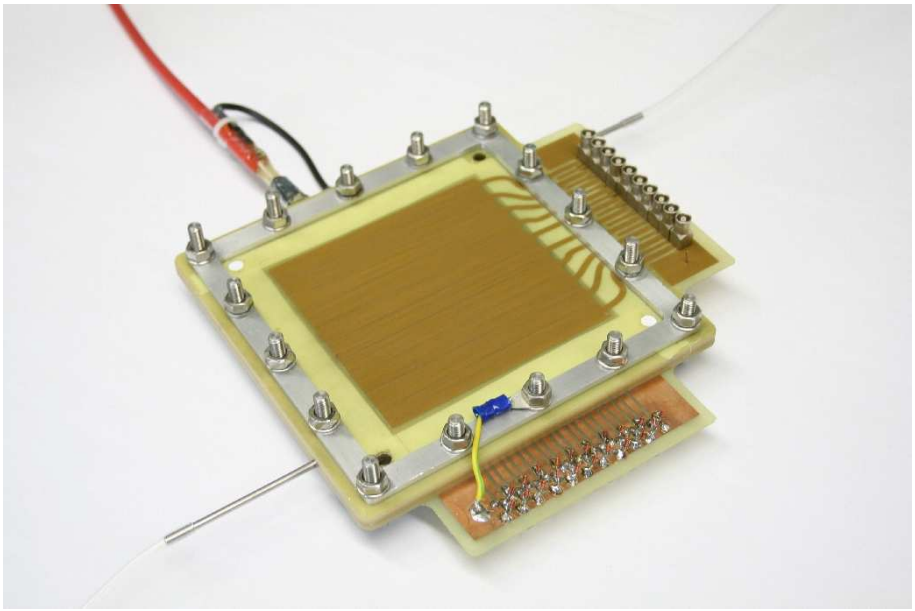

Figure 6.4: The assembled MWPC prototype.

6.1.4 Fill Gas

The chamber was filled with P-10, a gas mixture consisting of 90% of argon and 10 % of methane at atmospheric pressure via a thin metallic pipe with an inner diameter of 1 mm. A second pipe allows the gas to leave the chamber again. Using these two pipes, a constant gas flow can be realized which can be regulated by a flow meter. As described in Section 3.1.3, the main function of the argon is to liberate its outer electrons via secondary ionizations by the electrons from the converter foil. Although xenon would provide even better characteristics for the detection of ionizing particles, argon is chosen as the fill gas due to the high price of xenon. To avoid permanent discharges between the cathode and the anode induced by photon emitting excited argon atoms, methane is mixed with the argon to quench these photons as explained in Section 3.1.3.
The assembled prototype can be seen in Figure 6.4.

6.2 Conditioning of the Multiwire Proportional Chamber

When constructing a multiwire proportional chamber, one has to avoid any particles of dust or impurities in the chamber when closing the body. Therefore the assembling of the individual parts has to be done in a clean room. This room is constantly kept under positive pressure so that no impureness can contaminate the room when the door is opened. In addition, an air conditioning permanently filters the air to grant a highly purged ambiance. When closing the body each part of the chamber has to be cleaned with compressed air from a pressurized dispenser.
The problem with any kind of pollution in the gas filled multiwire proportional chamber is the occurrence of the so called *sparking*. When small particles of dust stick to one of the wires while the high voltage is applied, it is possible that the dirt particles influence the electric field and cause a spontaneous discharge from the wires towards the cathode pads. At best, this may cause a dysfunction of the chamber by showing signals without ionizing particles propagating through the chamber. In the worst case the chamber or even the readout electronics may take serious damage.
Despite the taken precautions, it cannot be avoided that some impurities remain in the closed chamber body. To remove these small particles of dust that usually stick to one of the wires, an elaborate procedure is required every time the body has been opened. At first, the chamber is filled with the counting gas using a flow of around 1000 $\frac{\mathrm{mm}^3}{\mathrm{h}}$. Usually this gas flow removes some of the impurities just by the mechanical pressure. After the venting with the fill gas, the so-called *conditioning* can be performed.
Here, the voltage that is applied to the anode wires is increased very slowly. With an external ammeter the current that goes through the wire chamber is measured very precisely. The voltage is increased slowly until the current rises as well. When the current exceeds a value of around 50 nA, the current is held until the current decreases again to a value of 0 nA. Usually this takes a few minutes up to a few hours. When the current has vanished again, the applied voltage is increased again to *accustom* the multiwire proportional chamber to higher voltages. Using this procedure, the small particles of dust which stick to the wires can be loosened. With increasing voltage, growing avalanches occur in the ambiance of the wires and remove the impurities. A radioactive source, for example a ^{55}Fe-source can be used to

induce primary ionizations that are amplified by the strong electric field to produce more avalanches.
A second problem for the consistent function of the wire chamber is the imprecise manufacturing of the wires. When the wires do not have a round and even surface, little pinnacles may transform the electric field in the direct proximity and therefore may cause an unpredictable behavior. To remove these microscopic pinnacles, a conditioning described above, but using a negative voltage instead, is performed. By using the negative voltage, the positive cations are accelerated towards the cathode wires and batter the pinnacles. This type of conditioning has to be performed very carefully since it may also damage the wires. When performing this procedure for the first time, a very high negative voltage of about 2000 V has been applied for two days. After this intensive bombardment of the wires with the argon cations, the burden to the wires was so strong, that one of the wires broke and produced a short circuit inside the chamber.
The voltage at which the current began to increase was around 1500 V. Therefore the voltage was increased gradually up to a value of 2300 V. At a voltage of more than 2400 V, the chamber showed audible sparking when gas discharges occurred between cathode and anode even after long periods of conditioning.

6.3 Converter Pads

As described in Chapter 5, the problem with detecting 511 keV γ-rays with multi wire proportional chambers is the very low cross section for a photoelectric effect or a Compton effect in the low-Z gas atoms. Therefore a converter made of lead combined with copper cathodes vaporized on a thin foil of polyamide have been discussed in Section 5.1 and Section 6.1. Since these cathodes showed an unpredictable behavior, new cathode planes made of circuit boards have been designed. Unfortunately the circuit boards have a thickness of 500 μm so that the electrons from the converter would not pass the cathodes and enter the inner volume of the MWPC.
A new idea to have the electrons emitted directly into the inside of the MWPC was to use the pads themselves as a converter. Therefore the pads cannot be vaporized any more, as a thickness of the determined 70 μm cannot be vaporized without complications.
To solve this problem, it has been tried to galvanize the lead onto the pattern plated copper plates. Unfortunately the copper did not afford hold to the lead. The fringy layer of lead peeled off much too easily; therefore it was not possible to simonize the surface to ensure a solid layer with a thickness of 70 μm. Furthermore the electroplating with lead has to be performed with hydrofluoric acid [Jel97] which is a very dangerous chemical to deal with. For these reasons the decision has been made not to electroplate the converter pads in the Institut fr Kernphysik, but to assign the commercial company OTR-GmbH to produce several prototypes made of lead to test the converter pads with a working MWPC.
Since the electroplated lead did not adhere properly to the copper cathode strips, a second cathode construction has been ordered from OTR-GmbH Rathenow. To convert the incident γ-rays into electrons, a high atomic mass number Z is unalterable. Since gold ($Z = 79$) has a similar atomic mass number as lead ($Z = 82$), it seems to be suitable to use gold instead of lead. Although the costs of supplies are much higher for gold than for lead, gold provides several advantages, as there are:

- Electroplating with gold is much easier than the galvanization with lead and is performed much more often. For this reason there are much more commercial companies offering this procedure.

- The density of gold is 19.3 $\frac{\mathrm{g}}{\mathrm{cm}^3}$, while the density of lead is 11.3 $\frac{\mathrm{g}}{\mathrm{cm}^3}$ [Lid06]. Therefore a converter made of gold can be much thinner than the thickness of a converter pad made of lead. The estimation that has been used to calculate the

lead thickness in Section 5.1, gives a value of 35 μm for the optimal thickness of a converter made of gold. However, the exact optimal layer thickness should also be determined experimentally.

- Compared to lead, gold is a very precious metal. The standard reduction potential is 1.498 V. The one of lead is -0.1263 V [Lid06]. Therefore the gold-plated pads do not form an oxide film at their surface as distinctive as the lead pads do. An oxide film could change the converters properties in an unpredictable way. Especially since the surface of the cathode pads has to be very homogeneous, an oxide film could bias the induced signals in a negative way.

With these new types of cathode strips, new tests can be performed to evaluate this way of photon conversion.

6.3.1 Lead Pads

The cathode that was electro-plated by OTR-GmbH Rathenow had a very crumbly surface. The coarse layer provided an electric connection between the 10 single pads and had to be polished and carved to get a more homogeneous surface and to isolate the single pads from each other. During the carving some sharp edges have been formed which have been polished but could not be removed entirely. These complications suggest that the signals from these pads could be unpredictable due to the inhomogeneous surface.

6.3.2 Gold Pads

The first cathode plane that was gilded by OTR-GmbH Rathenow has been handled very grubbily. The gold layer showed a very bright color, due to an impurity of palladium that deposited during the electroplating process. The copper did afford no hold to the gold and the circuit board deformed due to inner tension that presumably occurred when the circuit board was inserted into a heated electroplating solution. A second pad plane has been ordered, but has not yet been finished by OTR-GmbH.

6.4 Readout of the Chamber Signals

To readout the chamber signals automatically, the SIS 3320 VME 200 MHz Sampling ADC is used. The signals are amplified by a PNG CATSA charge-sensitive preamplifier. The ADC samples the output signals constantly and writes the sample values into the intern memory. For every channel a trigger can be programmed. When the signal exceeds the threshold value, the ADC keeps on sampling the signals for 3000 samples and then moves on to the next sample page for every channel. After every event, the related memory page is read out by the software and the data is written into a file. By this procedure, the data can be analyzed off-line to reconstruct the events.

With this method a data record has been taken by detecting incident cosmic radiation. Due to the uniform character of this radiation, all detector pads ought to detect a similar number of particles that pass through the filling gas. The histograms that show the number of detected particles for every single pad of the two pad planes are shown in Figure 6.5 and Figure 6.6. The blue boxes represent the statistical errors of $\frac{1}{\sqrt{N}}$ of the counted events. It can be seen that the single pads did not detect the same number of incident particles. Since the electronics that are used to amplify the detector signal and the sampling ADCs are the same, the problem seems to originate in the multiwire proportional chamber itself.

Since the spacing between the wires and the cathode pads has a wide influence on the signals that are read out [Wes07], this malfunction may be caused by the asymmetric application of Teflon strips that were used to seal the wire chamber. If two of the strips would overlap, the frames may fit asymmetric and the distance between wires and pads would not be constant for the whole pad plane. Therefore the chamber has been opened and reassembled again. This time the Teflon strips were applied without an overlap of two strips. After the new conditioning procedure, the measurement of the cosmic signals was repeated. The results that show a more satisfying signal distribution can be seen in Figure 6.7 and Figure 6.8.

The result of this measurement is the validation that the signals obtained from an MWPC highly depend on the distance between the wires and the cathode pads. As a consequence, the assembling has to be more precise for future wire chambers. Especially the Teflon strips have to be applied very accurate to avoid an overlap of two strips.

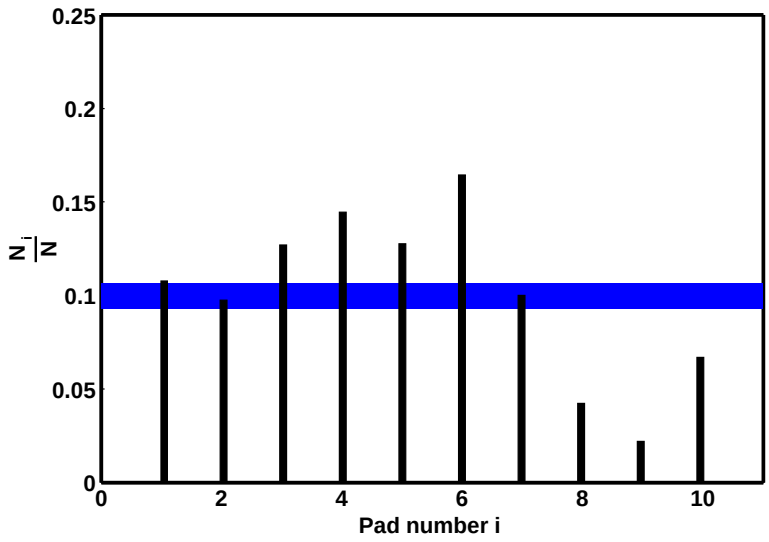

Figure 6.5: Histogram of the particles detected on the x-coordinate cathode plane.

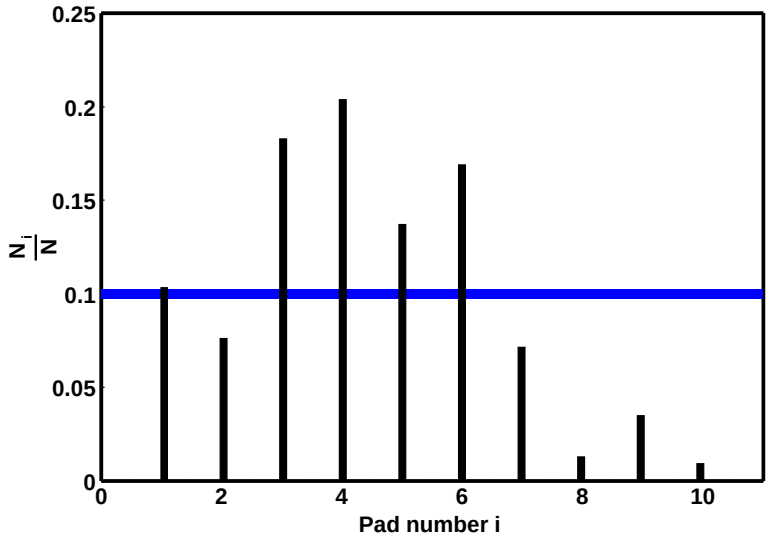

Figure 6.6: Histogram of the particles detected on the y-coordinate cathode plane.

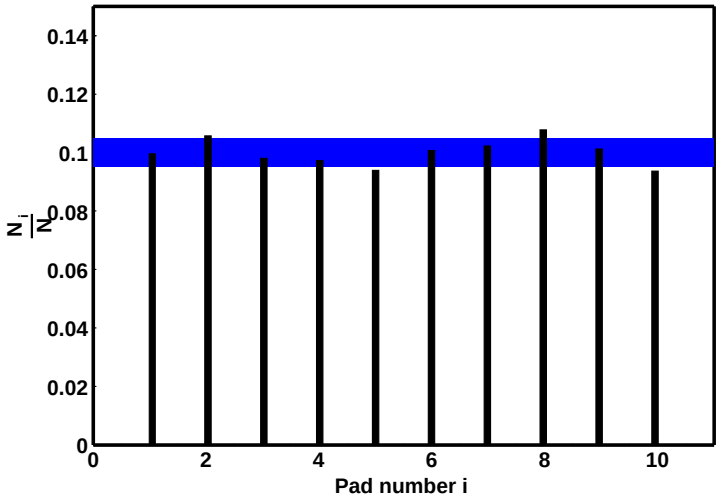

Figure 6.7: Histogram of the particles detected on the x-coordinate cathode plane. During the reassembling of the chamber, the Teflon strips did not overlap.

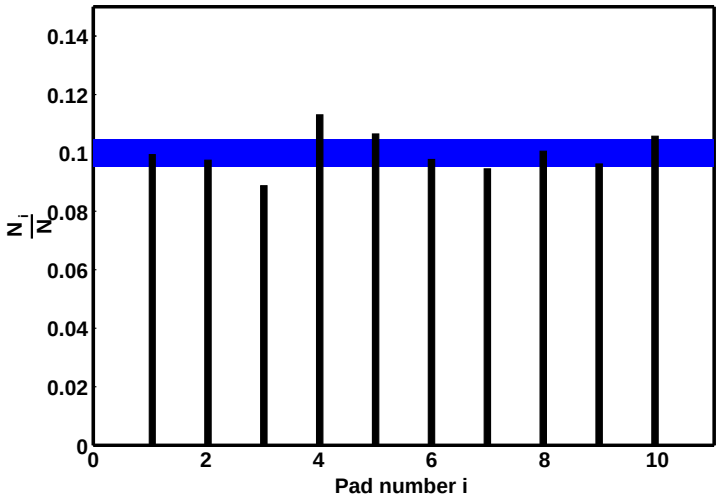

Figure 6.8: Histogram of the particles detected on the y-coordinate cathode plane. During the reassembling of the chamber, the Teflon strips did not overlap.

7. Evaluation of the Detector Performance

7.1 Calculation of the Achievable Sensitivity

As described in Section 4.1, the two main performance parameters of a small animal PET are the sensitivity and the volumetric spatial resolution. To evaluate the performance parameters of the constructed detector, these two parameters are to be calculated. For the calculation of the scanner sensitivity, two parameters are necessary: The probability for the two photons to enter the detector and the probability for the detector to detect the incident photons. The probability for the photons to be converted into an electron has been calculated in Section 5.1. As multiwire proportional chambers have an efficiency of nearly 1 for electrons, the detection efficiency of one MWPC can be assumed to be equal to the conversion probability. Unfortunately, the maximum efficiency of $y_e(d_{\text{opt}}) = 0.0038$ is still insufficient for the use in a small animal PET. To increase the count rate, several multiwire proportional chambers can be stacked in the same direction to detect more of the incident photons. For a stack of 50 chambers, the efficiency is calculated to be [Rey06]:

$$y_{e,50}(d) = y_e \cdot \exp^{-\frac{49 \cdot d_{\text{opt}}}{\lambda}} \tag{7.1}$$

With the optimal converter thickness of $d_{\text{opt}} = 70\ \mu\text{m}$, the maximum efficiency for 50 stacked MWPCs would be $y_{e,50}(d_{\text{opt}}) = 0.13$. Since the technology of PET is based on the detection of two photons, the detection efficiency for one annihilation event is:

$$y_c = (y_{e,50})^2 \tag{7.2}$$

And therefore the detection efficiency is $y_c(d_{\text{opt}}) = 0.018$, using the optimal converter thickness of $d_{\text{opt}} = 70\ \mu\text{m}$. The related plot can be seen in Figure 7.1.
To calculate the sensitivity, the probability for the annihilation photons to propagate through the detector has to be determined. For the estimation of this so-called geometric acceptance, the following assumptions are made:

- 50 MWPCs of growing area are stacked to achieve a better efficiency.
- The scanner consists of four stacks, one at each side of the field of view.
- The stacks fit closely together. No "dead area" occurs between the stacks.
- The inner MWPCs have an area of 16 cm × 16 cm.
- The detection area of the inner MWPCs is 10 cm × 10 cm.

Assuming a decay vertex in the center of the field of view, the solid angle that is covered with an active detection area can be calculated by integrating over the polar and azimuthal angles. The angles of $2 \cdot 0.18\pi$ are the angles, under which the detection area of the MWPCs is *seen* from the center of the detector.

$$\Omega_{\text{det}} = 4 \cdot \int_{\text{asin}\left(5(89-(8\tan\varphi)^2)^{-1}\right)}^{\text{asin}\left(5\left(89+(8\tan\varphi)^2\right)^{-1}\right)} \sin\vartheta \mathrm{d}\vartheta \int_{(1/2-0{,}18)\pi}^{(1/2+0{,}18)\pi} \mathrm{d}\varphi = 4.26 \tag{7.3}$$

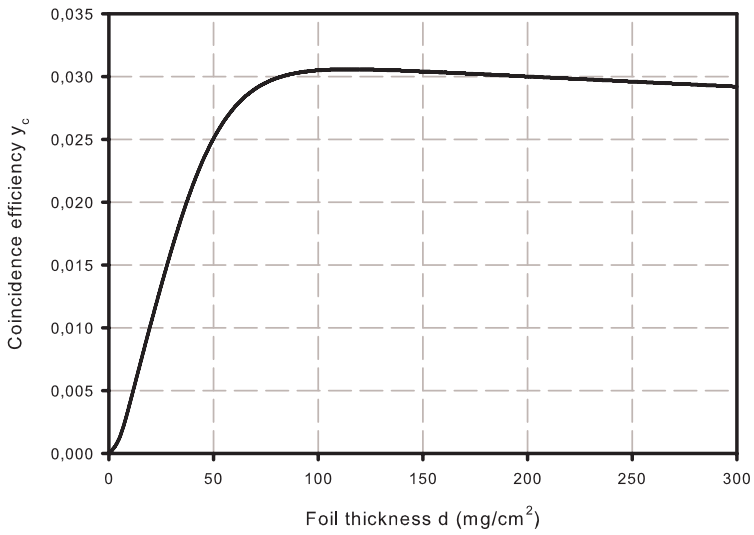

Figure 7.1: Probability to detect the two γ-particles from one annihilation event for $2 \cdot 50$ stacked MWPCs in dependence on the converter thickness.

With an overall solid angle of 4π, the fraction of the solid angle which is covered by detectors is:

$$\mathrm{D} = \frac{4.26}{4\pi} = 0.34 \tag{7.4}$$

The sensitivity is calculated as a product of the geometric acceptance and the detector efficiency:

$$S = D \cdot y_c(d_{\mathrm{opt}}) = 0.34 \cdot 0.018 = 0.006 \stackrel{\wedge}{=} 6\frac{\mathrm{counts}}{\mathrm{s} \cdot \mathrm{kBq}} = 6\frac{\mathrm{cps}}{\mathrm{kBq}} \tag{7.5}$$

Thus, the sensitivity that could be reached with the present architecture would be 0.6%. The consequences of this value for small animal PET scanners will be discussed in Section 7.3.

7.2 Calculation of the Achievable Spatial Resolution

The spatial resolution that can be achieved with a converting multiwire proportional chamber is mainly limited by one factor. The direction of the electrons that are liberated inside the converter material is not always perpendicular to the converter foil, but follows an angular distribution. This angular distribution may cause the electrons to travel in an oblique direction before they are detected. This movement could create inaccuracies in the correct detection of the interaction point. The problem, caused by the angular distribution of the liberated electrons, is illustrated in Figure 7.2.
From this follows, that the calculation of the spatial resolution requires the exact knowledge of the angular distribution of the electrons. With the experimental setup that has been used for the determination of the optimal converter thickness (Figure A.1, Appendix A), this angular distribution can be measured. To achieve a satisfying spatial resolution, the architecture of the multiwire proportional chamber may require modifications to prevent the electron from propagating parallel to the pad plane, by reducing the pitch between wires and converter layers.

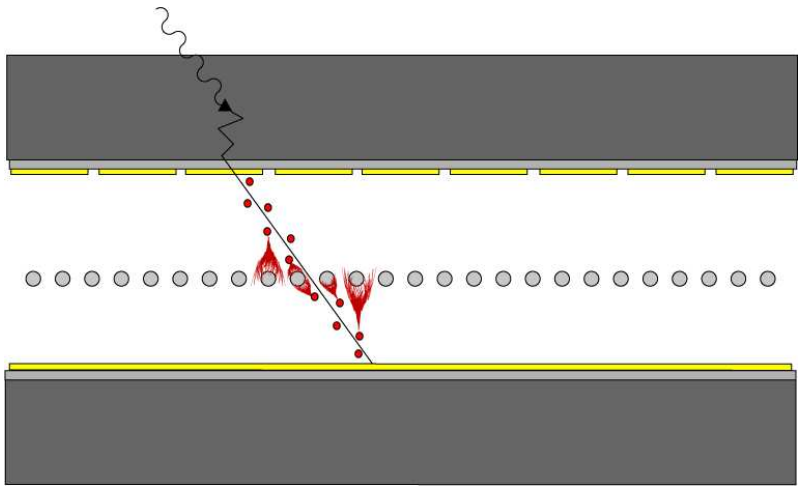

Figure 7.2: The angular distribution of the liberated electrons effects the spatial resolution of an MWPC.

7.2.1 Angular Distribution of the Liberated Electrons

The electrons that are liberated by the photoelectric effect or the Compton effect, vary with an angular distribution (see: Equation 2.21 and Equation 2.33) and in addition are scattered when propagating through the foil of lead. Therefore the angle with which the electrons leave the foil may differ from the original trajectory of the incoming photon. The negative effect of this angle on the spatial resolution could be minimized by reducing the gap between the converter and the anode wires on which the electrons are detected. Thereby the electrons are prevented from propagating a long distance before being detected by the wires.

To measure the angular distribution, an 80 μm thick foil is irradiated by a ^{137}Cs-probe that emits γ-rays of 662 keV and β^--particles of 1176 keV [Nuc00]. To avoid a bias of the measured spectra, the β^--particles are absorbed by 6 mm of perspex. A special clamp has been designed in the mechanical workshop of the Institut fr Kernphysik, on which the surface barrier detector can be mounted and rotated around a thin foil of lead to detect the escaping electrons. The angle between the beam axis and the surface barrier detector can be obtained from a scale that is engraved in the clamp. A sketch of the experimental setup is shown in Figure 7.3.

For angles between -70 and 70 degrees an energy spectrum is recorded for every 10 degrees. The obtained spectra can be seen in Figure 7.4 and Figure 7.5. To provide enough recorded events for an adequate statistical uncertainty, the minimum measuring time was defined to be 20.000 seconds. After the measurement a count rate is calculated for each channel of the histogram with the energy histogram and the measuring time.

To identify liberated electrons from the γ-ray-background of the ^{137}Cs-probe, the first data that is taken is a target-out-measurement, where only the spectrum of the ^{137}Cs-probe is taken without a foil of lead in the course of the beam. Since the ^{137}Cs-probe is positioned approximately in the center of the circular rail on which the detector is moved around the piece of lead and the γ-emission of the probe is isotropic, the target-out measurement does not have to be performed for all angles. This target out spectrum is subtracted from all following spectra to obtain only the events caused by the photo and Compton electrons.

As it has been done to calculate the most efficient converter thickness, the count rate growth when inserting the converter foil is defined by adding the values for energies from 420 keV up to 662 keV.

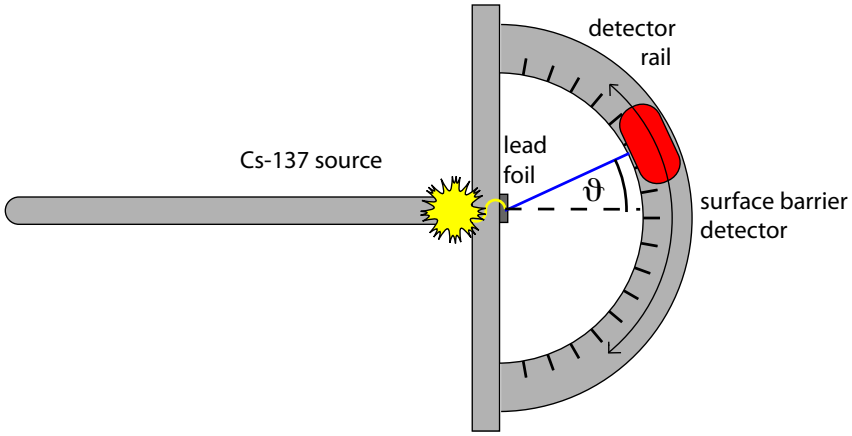

Figure 7.3: A sketch of the experimental setup to measure the angular distribution of the photo and Compton electrons. The converter foil is irradiated by the ^{137}Cs source, the liberated electrons are detected in the surface barrier detector.

This count rate growth describes the changes in the count rate functions that occur when the converter foil is inserted into the beam line. When it is normalized to the solid angle Ω one gets a Gaussian shaped function $\frac{\mathrm{d}^2N}{\mathrm{d}\Omega\cdot\mathrm{d}t}$ for the electron count rate in dependence on the solid angle Ω. This data is shown in Table 7.1 and plotted in Figure 7.6. The Gaussian seen in Figure 7.6 has been fitted to the data by the fitting algorithms of ROOT. The calculated parameters are:

Constant:	(1.0 ± 0.1)
Mean:	(3.4 ± 0.7)°
Sigma:	(34.0 ± 0.6)°

To calculate a mean exit angle (the actuarial expectation), the electron count rate in dependence on the scattering angle $\frac{\mathrm{d}^2N}{\mathrm{d}\vartheta\cdot\mathrm{d}t}$ has to be calculated from the measured electron count rate $\frac{\mathrm{d}N}{\mathrm{d}t}$.

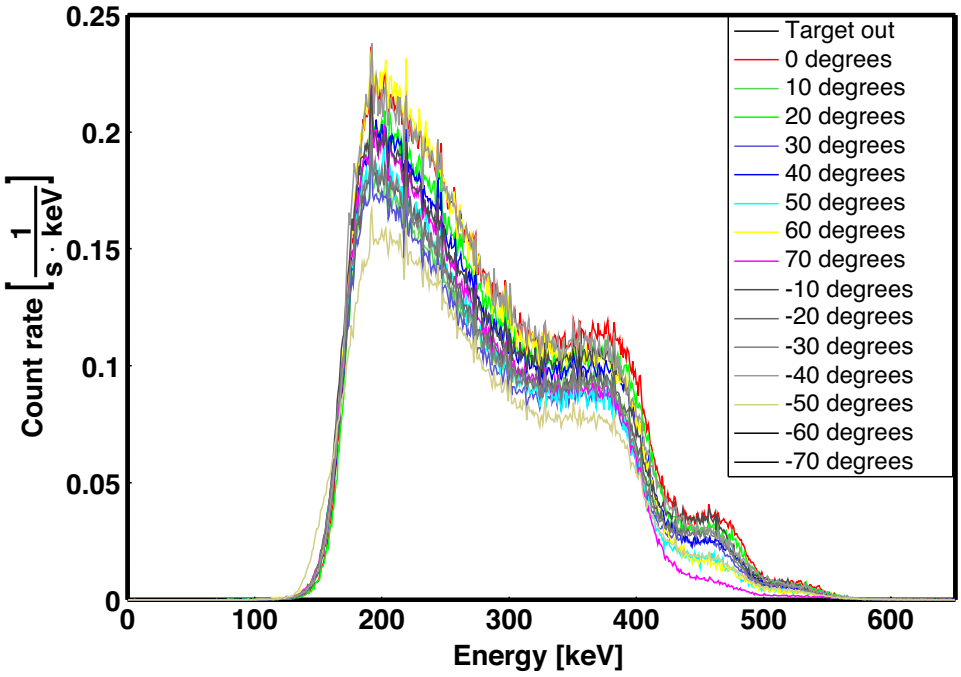

Figure 7.4: ^{137}Cs-spectra with 80 μm lead foil for different angles.

Since the circular surface barrier detector has a radius of 5 mm and an area of $D = \frac{\pi}{4}$ cm^2, one can calculate the fraction of the detector area and the area of a ring shaped fragment of the spherical shell around the interaction vertex with all points with a certain scattering angle on it. The area of this ring shaped fraction is:

$$A = r^2 \int_0^{2\pi} \int_{\vartheta_0 - 0.124}^{\vartheta_0 + 0.124} \sin\vartheta d\vartheta d\varphi \tag{7.6}$$

$$A = 2\pi r^2 \int_{\vartheta_0 - 0.124}^{\vartheta_0 + 0.124} \sin\vartheta d\vartheta \tag{7.7}$$

$$A = -2\pi r^2 \cos\vartheta|_{\vartheta_0 - 0.124}^{\vartheta_0 + 0.124} \tag{7.8}$$

Where $r = 4$ cm is the distance of the surface barrier detector to the interaction vertex, ϑ_0 is the angular position of the detector and $2 \cdot 0.124$ is the angle of the

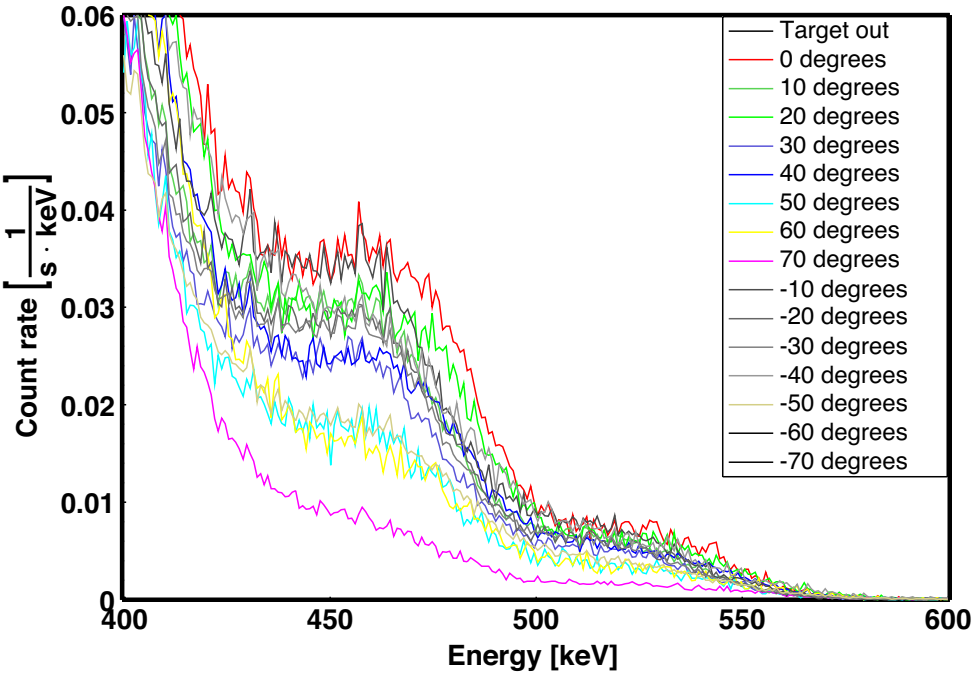

Figure 7.5: Closeup view of the interesting energy band of the ^{137}Cs-spectra.

cone that is spanned between the lead foil and the detector area. From this follows that the fraction of the detector area and the area of the ring fragment is:

$$\frac{A}{D} = -8r^2 \cos\vartheta|_{\vartheta_0-0.124}^{\vartheta_0+0.124} \tag{7.9}$$

This so-called acceptance correction factor represents the fraction of photons emitted within an angle of $\vartheta_0 \pm 7.125°$. The measured $\frac{\mathrm{d}N}{\mathrm{dt}}$ data can be weighted with this fraction and the angular width of the detector $\Delta\vartheta$ to obtain the $\frac{\mathrm{d}^2N}{\mathrm{d}\vartheta\cdot\mathrm{dt}}$ distribution. Table 7.2 shows the fraction $\frac{A}{D}$, the calculated $\frac{\mathrm{d}^2N}{\mathrm{d}\vartheta\cdot\mathrm{dt}}$ data and the uncertainties for $\frac{\mathrm{d}^2N}{\mathrm{d}\vartheta\cdot\mathrm{dt}}$. The calculated values are illustrated in Figure 7.7.
Since this data follows a Gaussian, two Gaussians have been fitted to these data points by the built-in fit algorithms of ROOT. The parameters for the two Gaussians are:

Measuring angle [°]	**Measuring time** [s]	**Count rate Sum(420-662 keV)** $[\mathbf{s^{-1} \cdot sr^{-1}}]$	**Count rate Sum(420-662 keV)-Sum$_0$(420-662 keV)** $[\mathbf{s^{-1} \cdot sr^{-1}}]$
-70	51669	9.34983	0.50925
-60	36546	21.04221	12.20163
-50	60864	25.64583	16.80525
-40	20852	31.12536	22.28478
-30	72246	39.19188	30.3513
-20	40023	43.61217	34.77159
-10	33656	52.04535	43.20477
0	29603	59.09337	50.25279
10	48015	53.28792	44.44734
20	20442	50.96574	42.12516
30	45870	41.26962	32.42904
40	63238	39.25299	30.41241
50	20737	28.47726	19.63668
60	21740	23.93475	15.09417
70	60589	14.259	5.39805

Table 7.1: Measuring time, count rate and count rate growth compared to the target out measurement for measuring angles from $-70°$ to $70°$.

Constant:	(30.4 ± 1.3)	Constant:	(25.0 ± 1.2)
Mean:	(36.7 ± 1.2)°	Mean:	(-35.3 ± 1.6)°
Sigma:	(17.3 ± 0.8)°	Sigma:	(17.2 ± 0.9)°

To calculate the mean exit angle, the arithmetic mean is determined and the uncertainties are summed:

$$\bar{\alpha}_{\text{mean}} = 36.0° \pm 2.8° \tag{7.10}$$

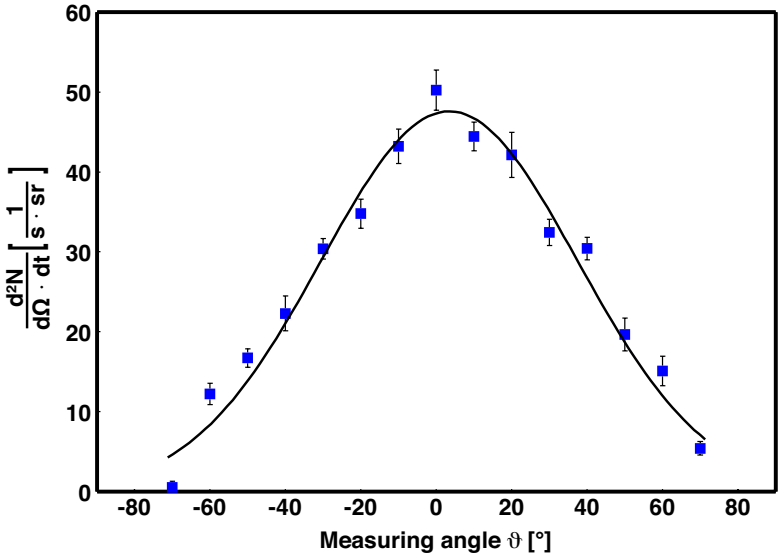

Figure 7.6: Electron count rate $\frac{\mathrm{d}^2N}{\mathrm{d}\Omega \cdot \mathrm{d}t}$ in dependence on the solid angle Ω.

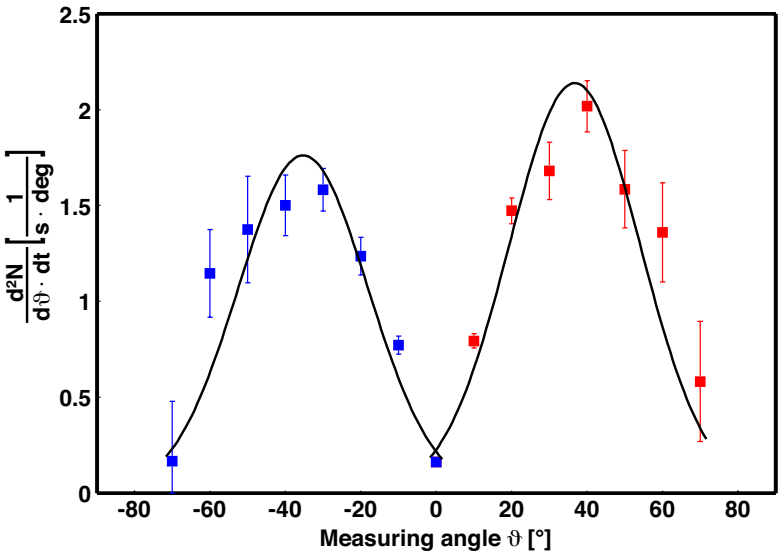

Figure 7.7: Electron count rate $\frac{\mathrm{d}^2N}{\mathrm{d}\vartheta \cdot \mathrm{d}t}$ in dependence on the measuring angle ϑ.

Measurement angle [°]	$\frac{\mathbf{A}}{\mathbf{D}}$	$\frac{\mathbf{dN}}{\mathbf{dt}} \cdot \frac{\mathbf{A}}{\mathbf{D}} \cdot \frac{\mathbf{1}}{\mathbf{\Delta\vartheta}} = \frac{\mathbf{d^2N}}{\mathbf{d\vartheta \cdot dt}}$ $[\frac{\mathbf{1}}{\mathbf{s \cdot deg}}]$	$\mathbf{d}\left(\frac{\mathbf{d^2N}}{\mathbf{d\vartheta \cdot dt}}\right)$ $[\frac{\mathbf{1}}{\mathbf{s \cdot deg}}]$
-70	29.8280	0.166	0.313
-60	27.4998	1.146	0.228
-50	24.2242	1.380	0.279
-40	20.4104	1.502	0.158
-30	15.8764	1.583	0.111
-20	10.8602	1.236	0.098
-10	5.5138	0.772	0.046
0	1	0.161	0.005
10	5.5138	0.793	0.037
20	10.8601	1.473	0.067
30	15.8764	1.682	0.150
40	20.4104	2.019	0.134
50	24.3242	1.586	0.202
60	27.5988	1.355	0.257
70	29.8380	0.582	0.313

Table 7.2: Acceptance correction factor $\frac{\mathrm{A}}{\mathrm{D}}$, $\frac{\mathrm{d}N}{\mathrm{dt}} \cdot \frac{A}{D} \cdot \frac{1}{\Delta\vartheta} = \frac{\mathrm{d}^2N}{\mathrm{d}\vartheta \cdot \mathrm{dt}}$ $[\frac{\mathbf{1}}{\mathbf{s \cdot deg}}]$ and the absolute uncertainty $\mathrm{d}\left(\frac{\mathrm{d}^2\mathrm{N}}{\mathrm{d}\vartheta \cdot \mathrm{dt}}\right)$ $[\frac{\mathbf{1}}{\mathbf{s \cdot deg}}]$ for the measurement angles of -70 ° to 70 °.

To calculate the mean distance, which the electrons travel before they can be detected at the wires, the mean tangent of the emission angle has to be derived. Figure 7.8 illustrates the electron count rate $\frac{\mathrm{d}^2N}{\mathrm{dtan}(\vartheta) \cdot \mathrm{dt}} = \frac{\mathrm{d}N}{\mathrm{dt}} \cdot \frac{\mathrm{A}}{\mathrm{D}} \cdot \frac{1}{\Delta\tan(\vartheta)}$ in dependence on $\tan(\vartheta)$. With the derived parameters of the Gaussian fits, the mean tangent of the exit angle can be calculated:

$$\overline{\tan(\vartheta)} = 0.65 \pm 0.05 \tag{7.11}$$

With the mean tangent the spatial resolution can be determined:

$$\frac{\Delta l}{l} = g \cdot \overline{\tan(\vartheta)} = 1.95 \text{ mm} \pm 0.15 \text{ mm} \tag{7.12}$$

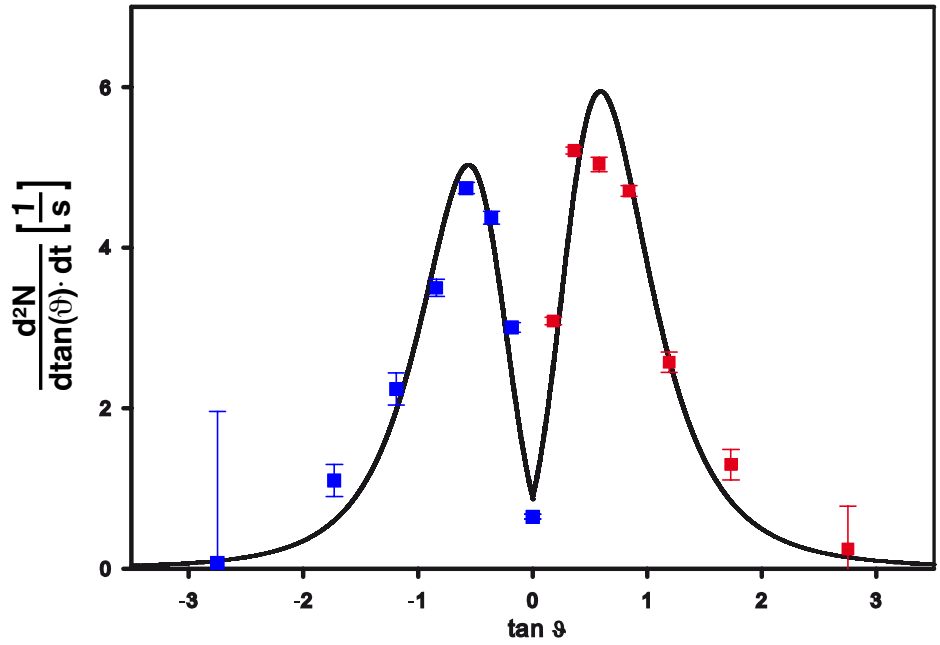

Figure 7.8: Electron count rate $\frac{\mathrm{d}^2N}{\mathrm{d}\vartheta \cdot \mathrm{dt}}$ in dependence on the measuring angle ϑ.

A PET scanner with a spatial resolution of 1.95 mm $\pm$ 0.15 mm is not competitive with other commercial devices. To keep up with these products, the resolution of the multiwire proportional chambers has to be improved by a factor of 2 - 3. Section 7.3 will discuss possibilities to enhance the performance of the detector.

7.3 Evaluation of the Performance Parameters

7.3.1 Evaluation of the Sensitivity

The sensitivity that has been calculated in Section 7.1 has a value of $S = 0.6\% \triangleq 11 \frac{\text{cps}}{\text{kBq}}$. This sensitivity would not be sufficient for a PET scanner and is not competitive with other products. Therefore, it would be desirable to improve the sensitivity even further. Since the sensitivity depends on the two factors geometric acceptance and detector acceptance, measures to enhance the sensitivity would have to improve either the one or the other factor. With the discussed method to convert the incident γ-particles into electrons, the only way to improve the detector acceptance would be the use of more than 50 stacked MWPCs. One idea to improve the geometric acceptance would be to revise the chamber architecture to reduce the dead areas, where the incident radiation is not detected.
The improvement of the sensitivity would be one of the primary aims of the further research on this project.

7.3.2 Evaluation of the Spatial Resolution

Small animal PET cameras nowadays are used to analyze the behavior of modern tracer molecules in the bodies of mice. Since neurology and cardiology are two of the three main fields of application of positron emission tomography, both the brain and the heart are of great interest for modern research.
Since the heart of a mouse has a length of 6-8 mm, while its width is about 3-5 mm and the brain has a length of approximately 7 mm, (refer: Section 4.1), the spatial resolution of 1.95 mm that has been calculated in Equation 7.12 is not a satisfactory result for a small animal PET camera. To visualize the adsorption processes of up-to-date tracer molecules it is indispensable to achieve better spatial resolutions.
Since the spatial resolution diminishes with reduced pad-wire distance, the so-called gap, one possibility to reduce the spatial resolution would be to construct a multiwire proportional chamber with a gap of only 1 mm. With this gap, the achievable spatial resolution would be:

$$\frac{\Delta l}{l} = g \cdot \tan \bar{\alpha}_{\text{mean}} = 0.65 \text{ mm} \pm 0.05 \text{ mm} \tag{7.13}$$

Since the mean free path in human tissue of ^{18}F positrons is on the order of 1 mm (Section 2.3.1), a resolution of $\frac{\Delta l}{l} = 0.65$ mm would be a sufficient result

that would be of great interest for medical scientists. With these two parameters of performance, the usability of the MWPC PET compared to other commercial products could be made clear by plotting the scatter plot illustrated in Figure 4.1 again, supplemented with the calculated performance data. The plot shows that the predicted spatial resolution would be highly competitive with other products, but the sensitivity would have to be improved to keep up with other products. The improvement of these parameters could be future tasks to be performed for the second generation of PET scanners.

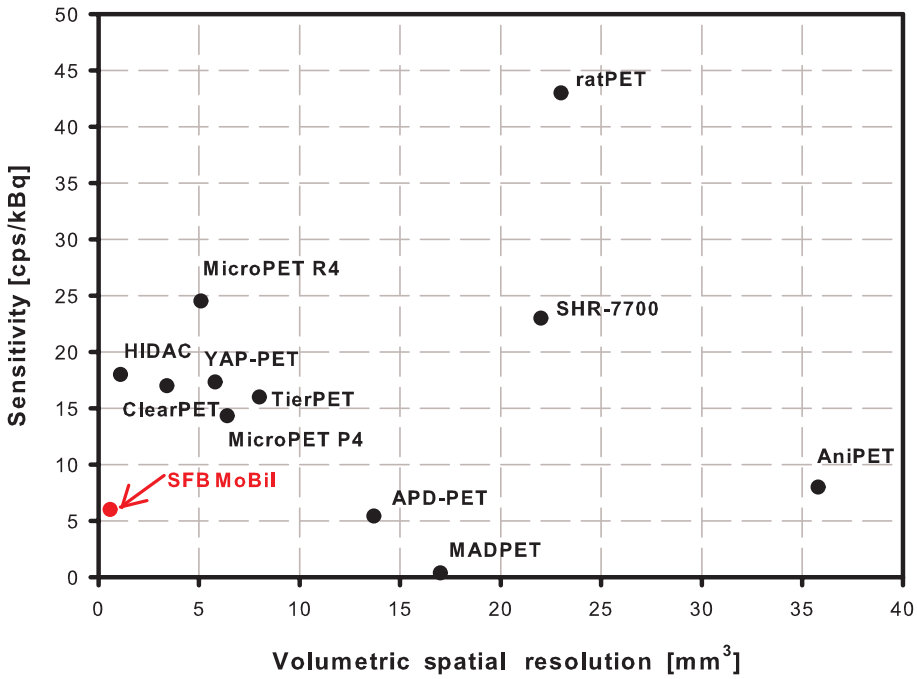

Figure 7.9: Comparison of the predicted performance parameters with the parameters of existing small animal PET devices.

If it would be possible to improve the sensitivity and to reach the predicted spatial resolution with a working PET scanner prototype, this device could match other commercial products and would be a great success for the Collaborative Research Center SFB 656 MoBil at the University of Mnster.

8. Future Prospects

8.1 1 mm-Prototype

To produce a second MWPC prototype that provides a spatial resolution that would be necessary to match existing small animal PET cameras, a new mechanical drawing was made. Figure 8.1 shows a rendered image of the mechanical drawing. Since several individual production steps (e.g. the frame has to be cut, the pad planes have to be etched on the surface of the circuit boards, the screw wholes have to be drilled very precisely) have to be performed to produce the new prototype, it is still in its construction process. To be independent of the ALICE TRD wire winding machine in Frankfurt, a winding machine had to be designed and constructed, too. Especially when a large number of proportional chambers have to be produced to achieve a sufficient efficiency, the efforts for this procedure have to be reduced to assure an efficient and economic production of MWPCs.

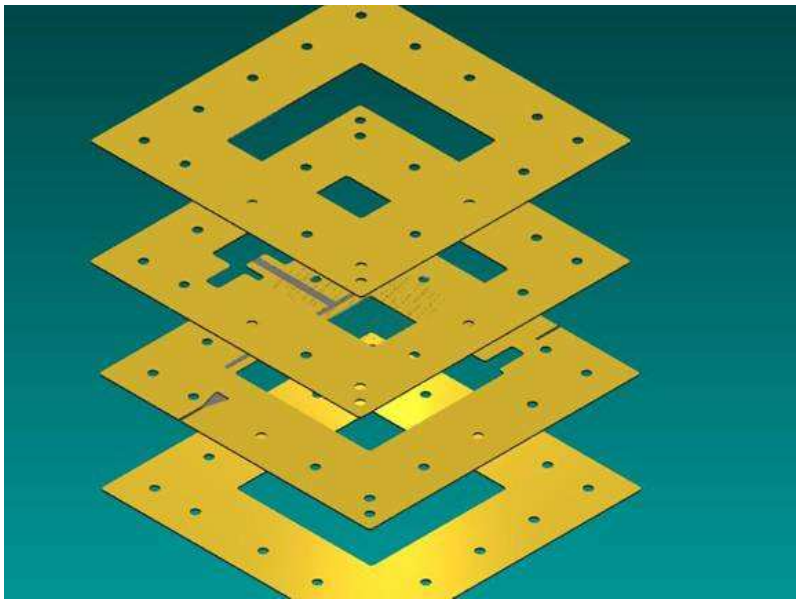

Figure 8.1: Engineering drawing of the new multiwire proportional chamber with a gap of 1 mm.

8.2 Readout ASICs

When reading out several multiwire proportional chambers, with at least 20 channels each, a huge amount of data accumulates that have to be analyzed. To not save gigabytes of digital data into a huge data storage system, at least a first trigger process has to be performed on-the-fly before the data is written to a hard disk. Therefore very fast and reliable electronics are necessary. On the one hand one would want the electronics to save all the relevant data, but on the other hand the data that is not relevant for the image reconstruction has to be deleted or not to be saved at all.
For purposes like that, so-called application specific integrated circuits are designed. The advantage of these ASICs is the inflexible but efficient analysis of known signals especially for one application.
For the DETNI[1] project, an ASIC has been developed especially for the neutron detectors that are produced. The N-XYTER ASIC that is being developed at the ASIC laboratory in Heidelberg, seems to have all the characteristics the readout electronics for the small animal PET project needs to have. Referring to [Sch06], the main specifications are:

Channels	128
Polarity	+/-
Data rate	32 MHz
Peaking time	18.5 ns / 139 ns
Timing resolution	1 ns
Trigger	Internal PDH Trigger
Power consumption	12.8 mW/channel

[1]DETNI: Detectors for Neutron Instrumentation. The DETNI project is a European collaboration that researches on the development of new types of neutron detectors. Since increasing neutron intensities are expected in future experiments, new detectors with high resolutions and efficiencies are needed. Another goal of DETNI is the development of a frontend ASIC for the new detectors.

Such an ASIC seems to be optimal for the purpose of the small animal PET, since a fast and effective readout electronic system that reduces the data output to the relevant data and provides every value with a precise timestamp could simplify the image reconstruction and allow an off line data processing with high accuracy. Therefore one of the next steps would be to collaborate with the developers of the N-XYTER, or a similar ASIC, to develop a fast and precise readout system.

9. Summary

Due to the low cross section for a photoelectric effect or a Compton effect with an electron from the counting gas and the low density of the gas, the detection of 511 keV γ-particles in an MWPC is rather difficult. The incident photons have to be converted into electrons to increase the detection probability. One way of conversion is the use of lead foils to liberate photoelectrons and Compton electrons into the inner volume of the MWPC. Since the electrons that are liberated inside the converter are decelerated and stopped inside the lead foil if the foil is too thick, there is an optimal thickness which provides the maximal electron yield. This thickness was determined theoretically and experimentally to be 70 μm.

To test and to evaluate the principle of positron emission tomography using MWPCs, a working MWPC prototype has been constructed. It has been learned that the distance between the cathode pads and the anode wires is critical for a uniform detector performance.

To evaluate the achievable performance parameter, the angular distribution of the electrons that leave the converter and enter the MWPC has been determined experimentally. With an average angle of $36.0° \pm 2.8°$ and an anode-cathode gap 1 mm of, a volumetric spatial resolution of less than 0.65 mm $\pm$ 0.05 mm could be achieved. This result would be of great interest for medical research, since common PET scanners have a spatial resolution of 1 mm or lower.

The achievable sensitivity that has been determined mathematically is 6 $\frac{\text{counts}}{\text{s}\cdot\text{kBq}}$. This result would not be competitive with modern PET scanners. In order to compete with other products, the sensitivity has to be improved by the factor of two or three. The improvement of the sensitivity would be one of the primary aims in further research.

The main future task is the construction of a prototype with a gap of 1 mm to justify the achievable spatial resolution experimentally and the deployment of an automatic readout ASIC to analyze the data during the acquisition and determine the events that are relevant for image reconstruction.

A. Experimental Setups

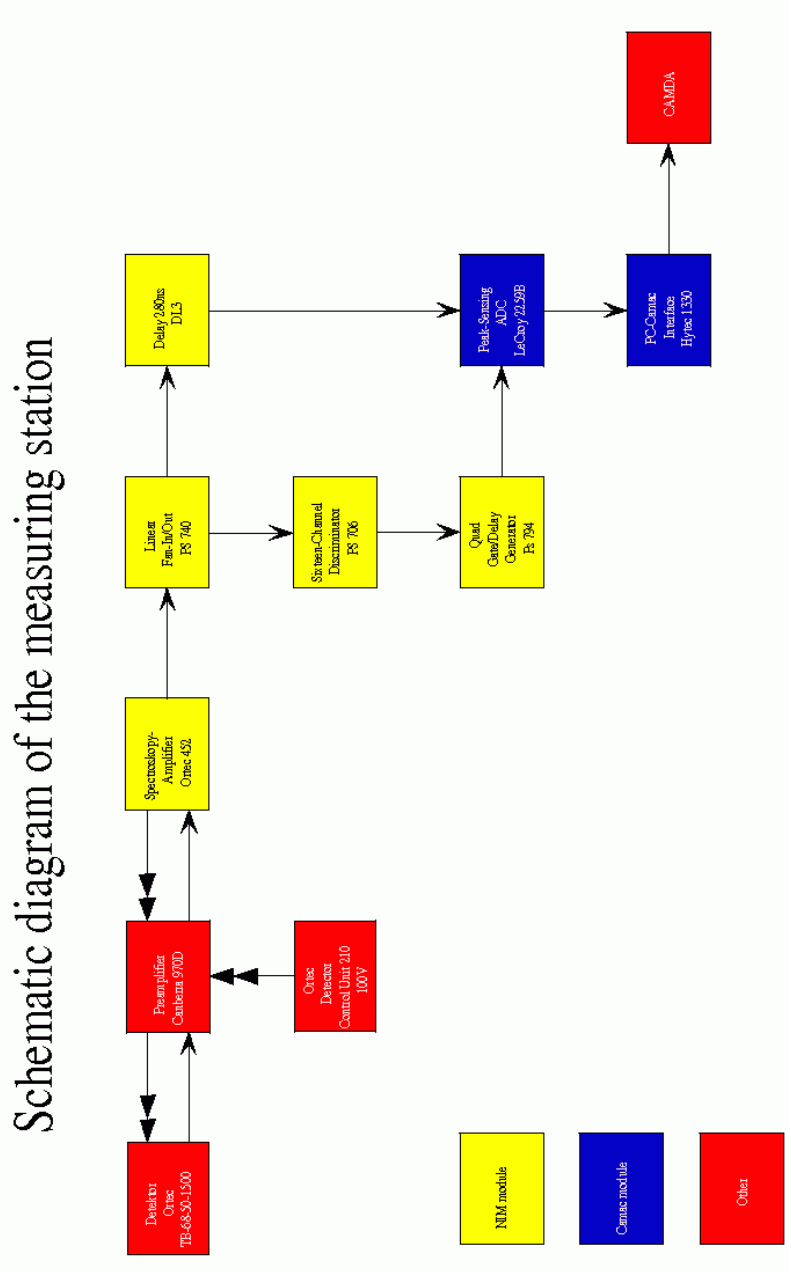

Figure A.1: Experimental setup for the determination of the optimal lead foil thickness.

Bibliography

[Ali06] CERN, 2006. URL `http://aliceinfo.cern.ch/`.

[Bai03] Bailey, D., Karp, J., and Surti, S. *Physics and Instrumentation in PET*. Springer-Verlag London, 2003.

[Ber79] Berko, S., Canter, K., and Mills, A. *Progress in Atomic Spectroscopy*, chapter 32. Plenum Press New York and London, 1979.

[Ber05a] Berger, M. J., et al. National Institute of Standards and Technology, Physics Laboratory, Ionizing Radiation Division. Stopping-Power and Range Tables for Electrons, Protons, and Helium Ions. http://physics.nist.gov/PhysRefData/Star/Text/contents.html, 2005.

[Ber05b] Berger, M. J., et al. National Institute of Standards and Technology, Physics Laboratory. XCOM: Photon Cross Sections Database. http://physics.nist.gov/PhysRefData/Xcom/Text/XCOM.html, 2005.

[Bet01] Bethge, K., Walter, G., and Wiedemann, B. *Kernphysik*. Springer-Verlag, 2001. ISBN 3–540–41444–4.

[Blu94] Blum, W. and Rolandi, L. *Particle Detection with Drift Chambers*. Springer-Verlag, 1994. ISBN 3–540–58322–X.

[Bre76] Breskin, A. et al. High-accuracy, bidimensional read-out of proportional chambers with short resolution times. *Nucl. Instr. and Meth.*, 143, pages 29–39, 1976.

[Bus02] Busch, O. *Position resolution with prototypes of ALICE Transition Radiation Detectors*. Master's thesis, Gesellschaft fuer Schwerionenforschung Darmstadt, 2002.

[Car06] Carron, N. J. *An Introduction to the Passage of Energetic Particles through Matter*. Taylor and Francis Group, 2006. ISBN 0–7503–0935–0.

[Cha68] Charpak, G. et al. The use of multiwire proportional counters to select and localize charged particles. *Nucl. Instr. and Meth.*, 62, pages 262–268, 1968.

[Cha70a] Charpak, G. Evolution of the automatic spark chambers. *Ann. Rev. Nucl. Sci.*, 20, pages 195–255, 1970.

[Cha70b] Charpak, G. et al. Some developments in the operation of multiwire proportional chambers. *Nucl. Instr. and Meth.*, 80, pages 13–34, 1970.

[Cha79a] Charpak, G. and Sauli, F. Multiwire proportional chambers and drift chambers. *Nucl. Instr. and Meth.*, 162, pages 405–428, 1979.

[Cha79b] Charpak, G. et al. High-accuracy localization of minimum ionizing particles using the cathode-induced charge centre-of-gravity read-out. *Nucl. Instr. and Meth.*, 167, pages 455–464, 1979.

[Cha84] Charpak, G. and Sauli, F. High-Resolution Electronic Particle Detectors. *Ann. Rev. Nucl. Sci.*, 34, pages 385–350, 1984.

[Chi55] Childers, H. M. and Graves, J. D. Bipartition Angles for Compton Scattering by Free Electrons. *The Physical Review*, 99(2), pages 343–345, 1955.

[Cho75] Cho, Z. H. et al. Positron ranges obtained from biomedically important positron emitting radionucleides. *J. Nucl. Med.*, 16, pages 1174–1176, 1975.

[Col65] Colombino, P., Fiscella, B., and Trossi, L. Study of positronium in water and ice from 22°C to −144°C by annihilation quantum measurement. *Nuovo Cimento*, 38, pages 707–723, 1965.

[Dav52] Davisson, C. and Evans, R. Gamma-Ray Absorption Coefficients. *Revs. Modern Phys.*, 24, pages 79–107, 1952.

[Deu92] Deusch, F. *Aufbau und Erprobung einer Vieldrahtproportionalkammer*. Examensarbeit, Westfaelische Wilhelms-Universitaet Muenster, 1992.

[Eng06] Engelen, M., Universitaesklinikum Muenster, Medizinische Klinik und Poliklinik C, Kardiologie und Angiologie. E-Mail, 2006.

[Fis77] Fischer, B. A digital processor for position sensitive detectors. *Nucl. Instr. and Meth.*, 141, pages 173–181, 1977.

[GEA07] CERN, 2007. URL `http://geant4.web.cern.ch/`.

[Got06] Gottschlag, H., WWU Muenster, Institut fuer Kernphysik. personal communication, 2006.

[Got07] Gottschlag, H., WWU Muenster, Institut fuer Kernphysik. personal communication, 2007.

[Gro70] Grove, R. et al. Electromagnetic delay line readout for proportional wire chambers. *Nucl. Instr. and Meth.*, 89, pages 257–262, 1970.

[Gru00] Grupen, C. *Astroteilchenphysik.* Friedr. Vieweg und Sohn Verlagsgesellschaft mbH, 2000. ISBN 3–528–03158–1.

[Hei53] Heitler, W. *The Quantum Theory of Radiation.* B.G. Teubner, 1953. ISBN 0–486–64558–4.

[Hei06] Heine, N., WWU Muenster, Institut fuer Kernphysik. personal communication, 2006.

[Hum03] Humm, J., Rosenfeld, A., and Del Guerra, A. From PET detectors to PET scanners. *Eur J Nucl Med Mol Imaging*, 30, pages 1574–1597, 2003.

[Jel97] Jelinek and other. *Praktische Galvanotechnik.* Eugen G. Leuze Verlag, 1997. ISBN 3–87480–108–x.

[KB06] Klein-Boesing, M., WWU Muenster, Institut fuer Kernphysik. personal communication, 2006.

[Kle92] Kleinknecht, K. *Detektoren fuer Teilchenstrahlung.* B.G. Teubner, 1992. ISBN 3–835–10058–0.

[Kno79] Knoll, G. *Radiation detection and measurement.* John Wiley & Sons, Inc., 1979. ISBN 0–471–49545–X.

[Kri04] Krieger, H. *Grundlagen der Strahlungsphysik und des Strahlungsschutzes*. B.G. Teubner, 2004. ISBN 3–519–00487–9.

[Kri06] Krieger, H., Klinikum Ingolstadt. E-Mail, 2006.

[Laz00] Lazurik, V. and Tabata, T. Radiation Dynamic Group, Kharkov National University and Institute for Data Evaluation and Analysis. EMID: Electron-Material Interaction Database. http://www3.ocn.ne.jp/˜ttabata, 2000.

[Leo87] Leo, W. *Techniques for nuclear and particle physics experiemtns*. Springer-Verlag, 1987. ISBN 0–387–17386–2.

[Lev99] Levin, C. and Hoffman, E. Calculation of positron range and its effect on the fundamental limit of positron emission tomography system spatial resolution. *Phys. Med. Biol.*, 44, pages 781–799, 1999.

[LHC06] CERN, 2006. URL `http://lhc.web.cern.ch/`.

[Lid06] Lide, D. R. et al. *CRC Handbook of Chemistry and Physics*. CRC Press, Taylor & Francis Group, 2006. ISBN 0–8493–0487–3.

[Lod05] Lodge, M. A. et al. Developments in Nuclear Cardiology: Transition from Single Photon Emission Computed Tomography to Positron Emission Tomography/Computed Tomography. *J. Invasiv. Cardiol*, 17, pages 491–496, 2005.

[Lut31] Lutze, E. Ueber die Richtungsverteilung der Photoelektronen kurzwelliger Roentgenstrahlen. *Ann. Physik*, 401, pages 853–864, 1931.

[Mob07] Collaborative Research Center - SFB 656 MoBil, 2007. URL `http://www.sfbmobil.de/`.

[Mos06] Moses, W. and Ullisch, M. Factors influencing timing resolution in a commercial LSO PET camerat. *Nuclear Science, IEEE Transactions on*, 53, pages 78–85, 2006.

[Mye02] Myers, R. and Hume, S. Small Animal PET. *European Neuropsychopharmacology*, 12, pages 545–555, 2002.

[Net91] Nettebrock, P. Konstruktion und Test einer Vieldrahtproportionalkammer, 1991.

[Nis29] Nishina, Y. and Klein, O. Ueber die Streuung von Strahlung durch freie Elektronen nach der neuen relativistischen quantumelektrodynamik von Dirac. *Zeit. Phys.*, 52, pages 853–868, 1929.

[Nob07] The Nobel Foundation. http://nobelprize.org/, 2007.

[Nuc00] Korea Atomic Energy Research Institute. Table of nucleides. http://atom.kaeri.re.kr/, 2000.

[Rao66] Rao, B. A Simple Formula for the Transmission and Absorption of Monoenergetic Electrons. *Nucl. Instr. Meth.*, 44, pages 155–156, 1966.

[Rey95] Reygers, K. *Aufbau eines Streamer-Tube Detektors mit Pad-Auslese durch einen integrierten Schaltkreis.* Master's thesis, Westfaelische Wilhelms-Universitaet Muenster, 1995.

[Rey06] Reygers, K., WWU Muenster, Institut fuer Kernphysik. personal communication, 2006.

[Sau31] Sauter, F. Ueber den atomaren Photoeffekt in der K-Schale nach der relativistischen Wellenmechanik Diracs. *Ann. Physik*, 403, pages 454–488, 1931.

[Sau77] Sauli, F. Principles of operation of multiwire proportional and drift chambers, Lectures given in the Academic Training Programme of CERN, 1975 – 1976. 1977.

[Sch92] Schatz, G. and Weidinger, A. *Nukleare Festkrperphysik.* Teubner Verlag, 1992. ISBN 3–51923–079–8.

[Sch03a] Schaefers, K. Imaging small animals with positron emission tomography. *Nuklearmedizin*, 42, pages 86–89, 2003.

[Sch03b] Schober, O. and Schicha, H. *Nuklearmedizin - Basiswissen und klinische Anwendung.* Schattauer, Stuttgart, 2003. ISBN 3–7945–2237–0.

[Sch06] Schmidt, C. J. Silicon Strip Readout for CBM employing N-XYTER, The First Dedicated Neutron Detector Readout ASIC. 2006, 8th CBM Collaboration Meeting, Strasbourg, Sept. 20. - 22. 2006.

[Sem72] Semat, H. and Albright, J. *Introduction to Atomic and Nuclear Physics*. Chapman and Hall, 1972. ISBN 0–412–11940–4.

[Smi] Smith, L. *An investigation into limits of resolution in Positron Emission Tomography resulting from non-collinear positron annihilation*. Master's thesis, University of Melburne. URL `www.ph.unimelb.edu.au/photo/people/leighton/thefinalcheck.pdf`.

[Sty06] Stypmann, J. and Engelen, M. Age and gender related reference values for transthoracic Doppler-echocardiography in the anesthetized CD1 mouse. *The International Journal of Cardiovascular Imaging*, 2006.

[Web96] Weber, S. Doktorarbeit, Westfaelische Wilhelms-Universitaet Muenster, 1996.

[Wes07] Wessels, J. P., WWU Muenster, Institut fuer Kernphysik. personal communication, 2007.

[Wie98] Wienhard, K., Wagner, R., and Heiss, W.-D. *PET, Grundlagen und Anwendungen der Positronen-Emissions-Tomographie*. Springer-Verlag, 1998. ISBN 3–540–19451–7.

[Wol74] Wolff, R. Measurement of the gas constants for various proportional-counter gas mixtures. *Nucl. Instr. and Meth.*, 115, pages 461–463, 1974.

[Zec06] Zecotek Medical Systems, 2006. URL `http://www.zecotekmed.com`.

Danksagung

Ich möchte mich bei allen bedanken, die auf ihre Weise zum Gelingen dieser Diplomarbeit beigetragen haben und ohne deren Unterstützung diese Arbeit nicht möglich gewesen wäre.

An erster Stelle sind das meine Eltern, vor allem meine Mutter Ilsebill Hünteler, die mich während meines gesamten Studiums uneingeschränkt unterstützt haben.

Dr. Klaus Schäfers danke ich für die Idee und Prof. Dr. Johannes Wessels für die Möglichkeit, meine Diplomarbeit im Projekt Small Animal PET zu absolvieren. Des Weiteren gilt Prof. Dr. Johannes Wessels mein Dank für die hervorragenden Arbeitsbedingungen am Institut für Kernphysik, sowie die Möglichkeit der Teilnahme an den DPG-Frühjahrstagungen in München und Regensburg, sowie der Tagung Imaging 2006 in Stockholm. Für das Zweitgutachten dieser Arbeit danke ich Prof. Dr. Christian Weinheimer.
Ein besonderer Dank gilt Holger Gottschlag, Klaus Reygers und Jan Pietschmann für die gute Zusammenarbeit im Projekt Small Animal PET. Für die zahlreichen Hilfestellungen und anregenden Diskussion möchte ich mich bei Bastian Bathen, Christoph Baumann, Dr. Tom Dietel, Holger Gottschlag, Melanie Klein-Bösing, Prof. Dr. Johannes Wessels, Alexander Wilk und insbesondere PD Dr. Klaus Reygers bedanken.

Für die stetige Hilfestellung bei chemischen, elektronischen, mechanischen oder physikalischen Problemen bedanke ich mich bei Helmut Baumeister, PD Dr. Alfons Khoukaz, Wolfgang Verhoeven sowie der elektronischen Werkstatt unter Leitung von Roland Berendes und der mechanischen Werkstatt und der Leitung von Georg Bourichter.

Für die Korrektur dieser Arbeit danke ich Christoph Baumann, Dr. Tom Dietel, Holger Gottschlag, Prof. Konrad Hünteler, Melanie Klein-Bösing, PD Dr. Klaus Reygers, Klaus Schürmann, Alexander Wilk und Oliver Zaudtke.

Bastian, Christoph, Holger und Jan danke ich für das Arbeitsklima im Kompetenzcenter. Auch wenn wir uns immer wieder gegenseitig abgelenkt haben, hat mir die Arbeit mit euch Spaß gemacht (Tooor!). Außerdem natürlich Alex, Ansgar, Baldo, Christian, Helge, Jan, Katharina, Klaus, Markus, Mela, Oliver, Richard, Robert, Tom und Uwe für die angenehme Zeit in der AG Wessels und die Unterstützung während der vergangenen 16 Monate.

Außerdem gilt mein Dank allen Freunden und Bekannten die mich - in welcher Form auch immer - während dieser Zeit unterstüzt, ertragen oder auch einfach mal von der Physik abgelenkt haben.

Katharina für das fünfblättrige Kleeblatt.

DANKE!

Eigenständigkeitserklärung

Ich versichere, diese Arbeit selbständig verfasst und keine anderen als die angegebenen Hilfsmittel und Quellen benutzt zu haben.
Münster, 20. 02 2007

Henning Hünteler